Honours Thesis - Dissertation - PHYS 4678 A01

CRN: 51222
Duration: Jan 18, 2017 - Apr 21, 2017
Credits: 3

Instructor for the course:

Dr. Can-Ming Hu
Professor
Department of Physics and Astronomy
University of Manitoba,
Winnipeg, Manitoba,
Canada R3T 2N2

Telefon: (001) 204 - 474 6189
Email: hu@physics.umanitoba.ca
Website: http://www.physics.umanitoba.ca/~hu
Office: Allen 332, availability for consultation anytime when I am in the office

Project supervisors for the course:

Dr. M. Gericke, Dr. Johan van Lierop, Dr. Juliette Mammei, Dr. Russell Mammei, Dr. Andreas Shalchi.

Course and project materials:

Each student should discuss with their project supervisor about the materials.

Evaluation procedure and a tentative schedule of the exam:

Each student should prepare **an oral presentation** and **a written thesis** for their Honours Thesis research. The final course grade will be determined from the student's performance in both, with an **equal weight**.

The oral presentation will be given in a block seminar on **Tuesday, April 18** (room: 326 Allen) that is open to the public. All students of this course are expected to participate in the block seminar. In case the project supervisor can not attend the block seminar, the student should make appointment individually with the project supervisor, presenting their slides, and get their slides and preparation evaluated by their project supervisor (**40%**). At the block seminar, each presentation consists of 20 min presentation plus 10 min Q/A, which will be evaluated by the course instructor (**40%**) and all other students (**20%**, averaged by all of them). The evaluation sheet is attached. After the block seminar, the students may revise their slides based on the discussions. The revised slides in PDF format must be submitted to the course instructor by the end of **Tuesday, April 18**. Late submission will receive 10% penalty of the mark.

The written thesis will be evaluated by the course instructor (**50%**) and the project supervisor (**50%**). The written thesis in PDF format must be submitted to both the course instructor and the

project supervisor by the end of **Tuesday, April 18**. Submission of a printed copy in addition to the PDF file is welcome. An example with the appropriate formatting and referencing style is attached. The thesis must be solely written by the student. Late submission will receive 10% penalty.

Bonus for publishing your result: with the goal of establishing a high-quality Honours Thesis research program in the department, students of this course are encouraged to publish the results of their Honours Thesis (with the help of their project supervisor). A 10% bonus of the total mark will be added to the students who are able to submit their written thesis together with a LaTeXed preprint of manuscript (with the student as the leading author) by the end of **Tuesday, April 18**. An example of the published high-quality Honours Thesis is attached. The manuscript may be jointly written by the student, the project supervisor, and other collaborators.

Academic Integrity

Students are expected to conduct themselves in accordance with the highest ethical standards and evince academic integrity in all their pursuits and activities at the university. As such in accordance with the General Academic Regulations and Requirements of the University of Manitoba, Section 7.1, students are reminded that "plagiarism or any other form of cheating in examinations or term tests (e.g. crib notes) is subject to serious academic penalty (e.g. suspension or expulsion from the faculty or university). A student found guilty of contributing to cheating in examinations or term assignments is also subject to serious penalty."

PHYS4678 Oral Presentation Evaluation Sheet (Tuesday, April 18, 2017) Name: _____

Speaker	1:30-2:00 Shepit, Michael M.	2:00-2:30 Lasuik, Jordan R.	2:30-3:00 Break	3:00-3:30 Klassen, Wolfgang J.	3:30-4:00 Hucko, Timothy
Project Supervisor	Dr. Johan van Lierop,	Dr. Andreas Shalchi		Drs. Gericke & R. Mammei	Dr. Juliette Mammei
Thesis Introduction Max: 20					
Objective and Method Max: 20					
Data analysis & conclusion Max 20					
Presentation Qualities Max 20					
Answer to questions Max 20					
Total (Max: 100)					
Course Instructor (40%)					
Project Supervisor (40%)					
Avg of all others (20%)					
Total Mark					

On The Line Shape of Electrically Detected Ferromagnetic Resonance

Michael Harder

April 17, 2011

A thesis submitted to the Department of Physics & Astronomy in partial fulfillment of the requirements for the honours physics thesis

Abstract

In this work we investigate the microwave induced ferromagnetic resonance (FMR) measured through electrical detection and show that the line shape depends strongly on the relative phase shift between electric and magnetic fields. Electrical detection of FMR is based on the anisotropic magnetoresistance (AMR) of a ferromagnetic strip which results in a time varying resistance dependent on the angle between the strip magnetization and current. Through the AMR effect the magnetization precession rectifies the microwave voltage, producing a non-zero time averaged dc voltage which is measured through lock-in amplification. This photovoltage has a Lorentz type line shape characteristic of resonance phenomena. However the line shape can range from purely symmetric to purely dispersive depending on the microwave frequency and sample structure, which is not accounted for in the conventional line shape description. By introducing a phase shift between the rf electric field, which drives a current in the strip, and the rf magnetic field which drives the magnetization precession, the line shape is shown to change dependent on the direction of the driving magnetic field, and the magnitude of the phase shift. This model is used to fit experimental data driven by various magnetic field components and enables a separation of their relative magnitudes and phases. In this way the line shape dependence on frequency and sample structure is accounted for due to a change in the relative phase induced by changing boundary conditions.

Contents

1 Introduction

1.1 Ferromagnetic Resonance

Ferromagnetic resonance was first discovered in the mid 20^{th} century when ferromagnetic materials were found to strongly absorb microwave frequency electromagnetic radiation [1]. These resonances in the Larmor frequency, which is the frequency of magnetic moment precession in a magnetic field, had been predicted by Landau and Lifshitz and were observed later by Griffiths as the shifted resonance peaks in the electron paramagnetic resonance (EPR) of electroplated ferromagnetic films [2]. As explained by Kittel these "anomalous" peaks, which lay outside of the normal resonance fields were due to the demagnetization fields which effectively reduced the magnetic field for a given Larmor frequency [3, 4].

As an experimental technique, FMR measurements began as macroscopic probes to study large ferromagnetic samples with measurements performed, for example, using microwave resonance cavities [1]. These techniques quickly developed into local ferromagnetic probes using local excitation and/or local detection and a variety of FMR techniques have since been used. By allowing researchers to probe the magnetization precession that gives rise to FMR, this spectroscopic technique enables the study of a materials underlying spin properties and as a result has become a standard tool in the research of spin dynamics making it invaluable to the field of spintronics. Recently the electrical detection of FMR has gained popularity amongst the spintronics community proving to be a powerful and precise experimental tool [5].

The electrical FMR detection is based on the anisotropic magnetoresistance which induces a time varying resistance due to the magnetization motion which becomes resonant for certain external fields. This method enables the study of microstructured ferromagnetic samples, further increasing its value in spintronics measurements. However electrical detection techniques require both amplitude and phase information to properly characterize the line shape which carries important physical information about the voltage production. The recent development of powerful phase resolved techniques has further enabled phase measurements of the rectified voltage which has opened the door to new studies of the FMR line shape [6]. Such research has applications to a broad range of condensed matter research, including the spin Hall effect.

1.2 Spin Hall Effect

The spin Hall effect has its origins in the spin flux generated by the current flow in a conductor as was theoretically described in 1971 by D'yakonov and Perel [7, 8]. This spin flux produces a spin accumulation which is limited by the spin relaxation time. The transverse voltage generated by such an effect was described by Hirsch in 1999 [9] and was first experimentally observed in semiconductors in 2004 [10, 11]. The experimental generation of a spin Hall voltage has resulted in a flurry of activity

in the condensed matter community and many groups are now studying the spin Hall effect in both semiconductors and ferromagnets. The reason for this interest is the ability to convert charge currents into spin currents and vice versa which has great potential in the field of spin driven electronics, or spintronics, since less energy would be required to drive spin currents than charge currents, and spin transport could be enabled without ferromagnets.

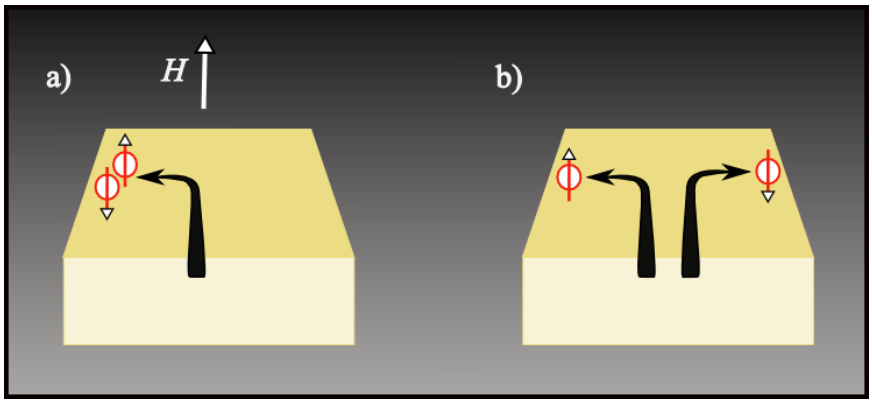

Figure 1: (a) Normal Hall effect where a magnetic field deflects moving electrons via the Lorentz force. Both spin up and spin down electrons are deflected the same way. (b) Spin Hall effect where spin dependent scattering occurs due to the spin-orbit interaction.

The spin Hall effect in a conductor is due to the spin dependent scattering of charge carriers originating from the spin-orbit interaction, which causes spin-up and spin-down electrons to flow in opposite directions resulting in a net spin accumulation [12]. It is analogous to the Hall effect in that the scattering of charge carriers results in the generation of a transverse voltage. However in the Hall effect an external magnetic field is required which is unnecessary for the spin Hall effect. Also the Hall effect will scatter both spin up and spin down carriers in the same direction whereas the spin Hall effect will cause spin dependent scattering. If the conductor has equal up and down spin densities, the equal and opposite Hall charge currents will cancel, leaving only a pure spin current [13].

Alternative methods for driving pure spin currents have also been proposed, such as spin pumping. As described by Tserkovnyak *et. al.* [14, 15] magnetization precession at a ferromagnetic-normal metal (F|N) interface can act as a spin pump which transfers a spin current from the ferromagnet into the normal metal due to the spin accumulation at the F|N interface. Such a spin current can be converted back into a charge current through the inverse spin Hall effect via the spin-orbit interaction which would again generate a spin Hall voltage. The effectiveness of either of these spin-charge conversion can be characterized by the spin Hall angle γ_{SH}, which is the ratio of spin Hall and charge conductivities.

An accurate determination of γ_{SH} has broad applications to spintronics, since the conversion between spin and charge currents determined by γ_{SH} is one key to developing spintronic devices. For instance by converting the spin pumping current into a charge current through the spin Hall effect, a spin battery could be enabled which could be used to power electronic devices [16, 17, 18]. Such spin powered devices are characterized by their low power consumption and small size and as such could be the future of electronics. A popular technique used to determine γ_{SH} is through the electrical detection of FMR. However experimentally determining γ_{SH} has proven controversial. For example, work by Seki *et. al.* found a large spin Hall angle in Au of $\gamma_{SH} = 0.113$ suggesting the giant spin Hall effect [19], however Mihajlovic *et. al.* found an upper limit for γ_{SH} in Au under similar conditions to be 0.023 [20]. Similarly in Pt the spin Hall angle was found to be 0.08 and 0.0037 by Ando *et. al.* [21] and Kimura *et. al.* [22] respectively. More recently Mosendz *et. al.* reported values of γ_{SH}=0.0067 in Pt and γ_{SH}=0.0016 in Au using spin pumping and the inverse spin Hall effect [12] while Liu *et. al.* reported $\gamma_{SH} = 0.056$ for bulk platinum [23]. In the later experiment a current in the Pt layer of a Py/Pt bilayer creates a spin current through the spin Hall effect which drives FMR in the adjacent Py layer; a reverse process to that used by Mosendz. A possible explanation given by Liu for the variation from the Mosendz result is that the spin diffusion length used by Mosendz was under estimated [23]. However, in such spin pumping experiments in addition to the spin Hall voltage there may be other voltages such as a voltage produced by the anisotropic magnetoresistance, and the proposed measurement schemes must account for this [9, 24]. Typically both effects are considered and are distinguished based on the symmetry or antisymmetry of the FMR lineshape [12]. However this symmetry analysis requires knowledge of the line shape phase; an additional problem which has not been properly addressed in the analysis of the FMR line shape.

1.3 The Relative Phase and Electrical Detection

The phase contribution to the electrically detected line shape has a component due to the well known spin resonance phase Θ which describes the phase lag between the response and the driving force. However there is also a phase contribution due to the relative electromagnetic phase Φ between the electric and magnetic fields. When an electromagnetic wave propagates through free space the electric and magnetic fields are in phase and orthogonal to each other. However when an electromagnetic wave travels though a dispersive medium where the wave vector and hence the index of refraction is complex, the imaginary contribution can create a phase shift between electric and magnetic fields. The most well known example is that of a plane electromagnetic wave moving in a conductor where Faraday's law gives a simple relation between electric and magnetic fields, $\omega\mu\mathbf{H} = \mathbf{k} \times \mathbf{E}$. Therefore the complex part of the wave vector $\mathbf{k}$ will induce a phase shift bewteen electric and magnetic fields. Although the field will exponentially decay inside a conductor, it will still penetrate

a distance on the order of the skin depth, and in a perfect conductor for frequencies below $\sim 10^{17}$ Hz the conductivity ($\sigma \sim 10^7$) which produces an imaginary dielectric constant will result in a phase shift of $\pi/4$ between the electric and magnetic fields [25, 26].

In a complex system, such as the series of waveguides, coaxial cables, bonding wires and sample holder required for electrical FMR detection, the relative phase cannot be calculated and even to create a simulation would be a highly nontrivial problem. Nevertheless the relative phase problem is fundamental to the study of the electrically detected FMR line shape and thanks to new phase resolved techniques, such as spintronic Michelson interferometry [6], an experimental probe now exists to examine such questions, which will be the focus of this work.

This work is organized as follows: In section 2 the theory of ferromagnetic resonance and the dynamic susceptibility, which is used to determine the electrically detected FMR line shape are described. In section 3 the experimental setup is discussed and in section 4 the experimental results and determination of the relative phase for different samples are presented. In section 5 the results and key findings are summarized in the conclusion. Finally in the appendix a possible calculation of the relative phase in a simple system is outlined, with possible concerns and questions raised and the final calculation left as an open question.

2 Theory

2.1 Ferromagnetic Resonance

The source of ferromagnetism is the spontaneous magnetic moment possessed by certain materials below the Curie temperature, T_C. This spin polarization arises from the exchange interaction which makes it energetically favorable for the spins of neighboring atoms to align [27, 28] resulting in a locally non-zero magnetization. To excite FMR the magnetization is aligned with an externally applied dc magnetic field, and an rf field is used to drive magnetization precession. While there are different forms of damping which are introduced based on phenomenological grounds, a description generally begins with the damping free Landau-Lifshitz equation

$$\frac{d\mathbf{M}}{dt} = -\gamma(\mathbf{M} \times \mathbf{H}_i). \tag{1}$$

Here γ is the electron gyromagnetic ratio and $\mathbf{H}_i$ includes all the magnetic fields seen by the electron such as fields from the exchange interaction, dipole-dipole interaction, anisotropy interaction and the externally applied field, which itself will contain a dc and rf term [29]. Eq. 1 describes motion without damping and consequently represents precession without a spin torque. Based on phenomelogical grounds damping was added in order to produce a torque which would force the magnetization inward and reduce the cone angle of the precession. With damping the Landau-Lifshitz equation becomes

$$\frac{d\mathbf{M}}{dt} = -\gamma(\mathbf{M} \times \mathbf{H}_i) - \lambda\left(\frac{(\mathbf{H}_i \cdot \mathbf{M})\mathbf{M}}{M^2} - \mathbf{H}_i\right), \tag{2}$$

where λ is the Landau-Lifshitz damping parameter with dimensions of frequency. Using the so called BAC CAB rule we have

$$\mathbf{M} \times (\mathbf{M} \times \mathbf{H}_i) = \mathbf{M}(\mathbf{M} \cdot \mathbf{H}_i) - \mathbf{H}_i(\mathbf{M} \cdot \mathbf{M}) = \mathbf{M}(\mathbf{M} \cdot \mathbf{H}_i) - \mathbf{H}_i M^2, \tag{3}$$

so that

$$\frac{(\mathbf{H}_i \cdot \mathbf{M})\mathbf{M}}{M^2} - \mathbf{H}_i = \frac{\mathbf{M} \times (\mathbf{M} \times \mathbf{H}_i)}{M^2}. \tag{4}$$

Thus we can rewrite the Landau-Lifshitz equation with damping as

$$\frac{d\mathbf{M}}{dt} = -\gamma(\mathbf{M} \times \mathbf{H}_i) - \lambda\left(\frac{\mathbf{M} \times (\mathbf{M} \times \mathbf{H}_i)}{M^2}\right). \tag{5}$$

Let α be the Gilbert damping parameter defined as

$$\alpha = \frac{\lambda}{\gamma M}, \tag{6}$$

then we have

$$\frac{d\mathbf{M}}{dt} = -\gamma(\mathbf{M} \times \mathbf{H}_i) - \frac{\alpha\gamma}{M}\left(\mathbf{M} \times (\mathbf{M} \times \mathbf{H}_i)\right). \tag{7}$$

If we then cross each side of Eq. 7 with $\mathbf{M}$ and use Eq. 3 with $\mathbf{M} \times \mathbf{M} = 0$ we have

$$\gamma\mathbf{M} \times (\mathbf{M} \times \mathbf{H}_i) = -\mathbf{M} \times \frac{d\mathbf{M}}{dt} + \alpha\gamma M(\mathbf{M} \times \mathbf{H}_i). \tag{8}$$

Using the above result in Eq. 7 we find the form of the Landau-Lifshitz-Gilbert equation commonly used

$$\frac{d\mathbf{M}}{dt} = -\gamma(\mathbf{M} \times \mathbf{H}_i)(1 + \alpha^2) + \frac{\alpha}{M}\left(\mathbf{M} \times \frac{d\mathbf{M}}{dt}\right). \tag{9}$$

The α^2 term is small and is typically neglected at this point. For now we follow through keeping this term to determine the dynamic susceptibility and will only set $\alpha^2 = 0$ when determining the line shape of the susceptibility elements. From Eq. 9 we can develop a picture of how the magnetic field acts on the magnetization. The first term describes a torque applied to the magnetization by the magnetic field, similar in form to the torque exerted by gravity on a precessing top [29, 30] as shown in Fig. 2.

The second term in the Landau-Lifshitz-Gilbert equation is perpendicular to

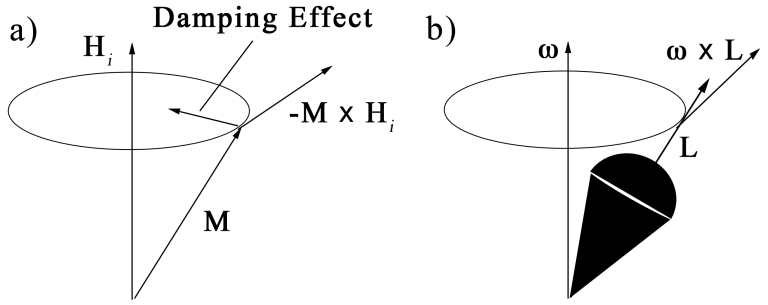

Figure 2: (a) Precession of the magnetization $\mathbf{M}$ due to the magnetic field $\mathbf{H}_i$. (b) Precession of a spinning top due to the torque from gravity.

both the magnetization and the torque and results in an inward force with tends to reduce the angle at which the magnetization is precessing which is also illustrated in Fig. 2. If we regroup Eq. 9 as

$$\frac{d\mathbf{M}}{dt} = -\gamma(\mathbf{M} \times \left(\mathbf{H}_i(1 + \alpha^2) - \frac{\alpha}{\gamma M}\frac{d\mathbf{M}}{dt}\right), \tag{10}$$

we see that the damping can be introduced into our original Landau-Lifshitz equation by the addition of a field which reduces the non damped field.

2.2 Dynamic Susceptibility

Solving the Landau-Lifshitz-Gilbert equation gives rise to the susceptibility tensor which relates the rf field to the rf magnetization. To solve the LLG equation we split both the magnetic field and the magnetization into dc and rf components. We will take the dc field, and hence the dc magnetization, to be along the $\widehat{z}$ direction. The rf response of the magnetization will to first order be perpendicular to $\widehat{z}$ so that the magnitude of $\mathbf{M}$ will be constant. This fact was actually already used in the definition of the Gilbert damping parameter in Eq. 6. Explicitly then to solve the LLG equation we take $\mathbf{H}_i = \mathbf{H}_{0i} + \mathbf{h}_i \mathrm{e}^{-i\omega t} = (0,\ 0,\ \mathrm{H}_{0i}) + (\mathrm{h}_{ix},\ \mathrm{h}_{iy},\ \mathrm{h}_{iz})\mathrm{e}^{-i\omega t}$ and $\mathbf{M} = \mathbf{M}_0 + \mathbf{m}\mathrm{e}^{-i\omega t} = (0,\ 0,\ \mathrm{M}_0) + (\mathrm{m}_x,\ \mathrm{m}_y,\ 0)\mathrm{e}^{-i\omega t}$ where $\mathbf{H}_{0i}$ is the internal dc magnetic field, $\mathbf{h}_i \mathrm{e}^{-i\omega t}$ is the internal rf field, $\mathbf{M}_0$ is the dc magnetization, and $\mathbf{m}\mathrm{e}^{-i\omega t}$ is the rf magnetization. Using these forms of the field and magnetization in the LLG equation yields

$$\begin{aligned}\frac{d\mathbf{M}_0}{dt} - i\omega \mathbf{m} e^{-i\omega t} = -\gamma \left[(\mathbf{M}_0 + \mathbf{m}e^{-i\omega t}) \times (\mathbf{H}_{0i} + \mathbf{h}_i e^{-i\omega t})\right](1+\alpha^2) \\ + \frac{\alpha}{M}\left[(\mathbf{M}_0 + \mathbf{m}e^{-i\omega t}) \times \left(\frac{\mathbf{M}_0}{dt} - i\omega \mathbf{m} e^{-i\omega t}\right)\right]. \qquad (11)\end{aligned}$$

Now if we use the linear approximation so that terms higher than the first power in $\mathbf{h}_i$ and $\mathbf{m}$ are ignored and since $\frac{d\mathbf{M}_0}{dt} = 0$ and $\mathbf{M}_0 \times \mathbf{H}_{0i} = 0$ ($\mathbf{M}_0$ is parallel to $\mathbf{H}_{0i}$) this result simplifes to

$$\mathbf{m} = \frac{\gamma}{i\omega}(1+\alpha^2)\left[\mathbf{M}_0 \times \mathbf{h}_i + \mathbf{m} \times \mathbf{H}_{0i}\right] + \frac{\alpha}{M}\mathbf{M}_0 \times \mathbf{m}. \qquad (12)$$

When the ferromagnetic strip is placed inside the externally applied magnetic field the strip will become polarized, and the magnetic dipoles at the surface will create an additional internal magnetic field that opposes the applied field. Thus the internal fields will not be the same as the externally applied fields but can be related to the external field through the demagnetization factors N_k, which depend on the sample geometry and are taken to be uniform in a given direction. For the k^{th} component the fields are then given by

$$\begin{aligned} h_{ik} &= h_K - N_k m_k, \\ H_{0ik} &= H_k - N_k M_k. \end{aligned} \qquad (13)$$

Here H_k and h_K are the externally applied dc and rf fields respectively where $h_K = h_k e^{i\Phi_k}$ could in general have a phase shift with respect to the rf current which will be described later. For the dc field only the z component is non-zero, so we only need to consider the case when $k = z$ and we can drop the subscript on the external field to give

$$H_i = H - N_z M_0. \qquad (14)$$

The cross products in the LLG equation then become

$$\begin{aligned}\mathbf{M}_0 \times \mathbf{h}_i &= -h_{iy}M_0\widehat{x} + h_{ix}M_0\widehat{y} = -(h_Y - N_yM_y)M_0\widehat{x} + (h_X - N_xM_x)\widehat{y},\\ \mathbf{m} \times \mathbf{H}_{0i} &= m_yH_{0i}\widehat{x} - m_xH_{0i}\widehat{y} = m_y(H - N_zM_0)\widehat{x} - m_x(H - N_zM_0)\widehat{y},\\ \mathbf{M}_0 \times \mathbf{m}_i &= -m_yM_0\widehat{x} + m_xM_0\widehat{y},\end{aligned}$$

and the LLG equation is

$$\begin{aligned}i\omega \begin{pmatrix} m_x \\ m_y \\ 0 \end{pmatrix} &= \gamma(1+\alpha^2)\left(M_0 \begin{pmatrix} -(h_Y - N_ym_y) \\ h_X - N_xm_x \\ 0 \end{pmatrix} + (H - N_zM_0)\begin{pmatrix} m_y \\ -m_x \\ 0 \end{pmatrix}\right) + i\omega\alpha\frac{M_0}{M}\begin{pmatrix} -m_y \\ m_x \\ 0 \end{pmatrix}\\ &= \gamma(1+\alpha^2)M_0\begin{pmatrix} -h_Y + N_ym_y \\ h_X - N_xm_x \\ 0 \end{pmatrix} + \left[\gamma(1+\alpha^2)(H - N_zM_0) - i\omega\alpha\right]\begin{pmatrix} m_y \\ -m_x \\ 0 \end{pmatrix}.\end{aligned}$$

In the last step we used $\frac{M_0}{M} \approx 1$ which is consistent with taking M to be constant and ignoring higher order terms in $\mathbf{m}$. Now we define

$$\begin{aligned}\omega_m &= \gamma(1+\alpha^2)M_0,\\ \omega_0 &= \gamma(1+\alpha^2)(H - N_zM_0),\end{aligned} \tag{15}$$

so that the LLG solution becomes

$$i\omega \begin{pmatrix} m_x \\ m_y \\ 0 \end{pmatrix} = \omega_m \begin{pmatrix} -h_Y + N_ym_y \\ h_X - N_xm_x \\ 0 \end{pmatrix} + \omega_0 - i\omega\alpha \begin{pmatrix} m_y \\ -m_x \\ 0 \end{pmatrix}. \tag{16}$$

This gives two equations

$$\begin{aligned}i\omega m_x &= -\omega_m h_Y + (\omega_m N_y + \omega_0 - i\alpha\omega)m_y,\\ i\omega m_y &= \omega_m h_X - (\omega_m N_x + \omega_0 - i\alpha\omega)m_x.\end{aligned} \tag{17}$$

Combining these two

$$\begin{aligned}(i\omega)^2 m_x &= -i\omega\omega_m h_Y + (\omega_m N_y + \omega_0 - i\alpha\omega)i\omega m_y\\ &= -i\omega\omega_m h_Y + (\omega_m N_y + \omega_0 - i\alpha\omega)(\omega_m h_X - (\omega_m N_x + \omega_0 - i\alpha\omega)m_x)\\ &= -i\omega\omega_m h_Y + \omega_m(\omega_m N_y + \omega_0 - i\alpha\omega)h_X - [(\omega_m N_y + \omega_0)(\omega_m N_x + \omega_0)\\ &\qquad - i\alpha\omega(\omega(N_x + N_y) + 2\omega_0) - \alpha^2\omega^2]m_x.\end{aligned}$$

Letting

$$\begin{aligned}\omega_r^2 &= (\omega_m N_y + \omega_0)(\omega_m N_x + \omega_0)\\ &= \gamma^2(1+\alpha^2)(H + M_0(N_y - N_z))(H + M_0(N_x - N_z)),\end{aligned} \tag{18}$$

we find

$$m_x = \frac{\omega_m(\omega_m N_y + \omega_0 - i\alpha\omega)h_X - i\omega\omega_m h_Y}{\omega_r^2 - (1+\alpha^2)\omega^2 - i\alpha\omega(2\omega_0 + \omega_m(N_x + N_y))}. \tag{19}$$

Proceeding in the same manner of substitution one can easily find m_y to be given by

$$m_y = \frac{i\omega\omega_m h_X + \omega_m(\omega_m N_x + \omega_0 - i\alpha\omega)h_Y}{\omega_r^2 - (1+\alpha^2)\omega^2 - i\alpha\omega(2\omega_0 + \omega_m(N_x + N_y))}. \tag{20}$$

Eqs. 19 and 20 allow us to define the susceptibility tensor which relates the magnetization and magnetic field

$$\mathbf{m} = \widehat{\chi}\mathbf{h} = \begin{pmatrix} \chi_{xx} & i\chi_{xy} & 0 \\ -i\chi_{xy} & \chi_{yy} & 0 \\ 0 & 0 & 0 \end{pmatrix} \mathbf{h}, \tag{21}$$

where

$$\begin{aligned}
\chi_{xx} &= \frac{\omega_m(\omega_m N_y + \omega_0 - i\alpha\omega)}{\omega_r^2 - (1+\alpha^2)\omega^2 - i\alpha\omega(2\omega_0 + \omega_m(N_x + N_y))}, \\
\chi_{xy} &= \frac{-\omega\omega_m}{\omega_r^2 - (1+\alpha^2)\omega^2 - i\alpha\omega(2\omega_0 + \omega_m(N_x + N_y))}, \\
\chi_{yx} = -\chi_{xy} &= \frac{\omega\omega_m}{\omega_r^2 - (1+\alpha^2)\omega^2 - i\alpha\omega(2\omega_0 + \omega_m(N_x + N_y))}, \\
\chi_{yy} &= \frac{\omega_m(\omega_m N_x + \omega_0 - i\alpha\omega)}{\omega_r^2 - (1+\alpha^2)\omega^2 - i\alpha\omega(2\omega_0 + \omega_m(N_x + N_y))}.
\end{aligned} \tag{22}$$

To proceed further and split the solutions into their symmetric and antisymmetric Lorentz contributions we will first ignore terms of order α^2. ω_m, ω_0 and ω_r then become

$$\begin{aligned}
\omega_m &= \gamma M_0, \\
\omega_0 &= \gamma(H - N_z M_0), \\
\omega_r^2 &= \gamma^2(H + M_0(N_y - N_z))(H + M_0(N_x - N_z)),
\end{aligned} \tag{23}$$

and $\widehat{\chi}$ simplifies slightly

$$\begin{aligned}
\chi_{xx} &= \frac{\omega_m(\omega_m N_y + \omega_0 - i\alpha\omega)}{\omega_r^2 - \omega^2 - i\alpha\omega(2\omega_0 + \omega_m(N_x + N_y))} = \omega_m(\omega_m N_y + \omega_0 - i\alpha\omega)F, \\
\chi_{xy} &= \frac{-\omega\omega_m}{\omega_r^2 - \omega^2 - i\alpha\omega(2\omega_0 + \omega_m(N_x + N_y))} = -\omega\omega_m F, \\
\chi_{yx} = -\chi_{xy} &= \frac{\omega\omega_m}{\omega_r^2 - \omega^2 - i\alpha\omega(2\omega_0 + \omega_m(N_x + N_y))} = \omega\omega_m F, \\
\chi_{yy} &= \frac{\omega_m(\omega_m N_x + \omega_0 - i\alpha\omega)}{\omega_r^2 - \omega^2 - i\alpha\omega(2\omega_0 + \omega_m(N_x + N_y))} = \omega_m(\omega_m N_x + \omega_0 - i\alpha\omega)F,
\end{aligned} \tag{24}$$

where

$$F = \frac{1}{\omega_r^2 - \omega^2 - i\alpha\omega(2\omega_0 + \omega_m(N_x + N_y))}. \tag{25}$$

With the expressions in Eq. 24 we can see that the resonance condition is $\omega = \omega_r$. Since the resonance frequency depends on the demagnetization factors, ω_r will change depending on the static field configuration. This resonance condition allows us to express a fixed frequency ω in terms of the resonance field H_r which will vary depending on the value of ω,

$$\omega^2 = \gamma^2(H_r + M_0(N_y - N_z))(H_r + M_0(N_x - N_z)). \tag{26}$$

Using Eqs. 23 and 26 the components of $\widehat{\chi}$ can be written in terms of their symmetric and antisymmetric Lorentz line shapes by expressing F in terms of the applied field H and the resonant field H_r. This is also the desired form of $\widehat{\chi}$ since in the experiments performed ω will be fixed while the field will be varied.

$$\begin{aligned}
F &= \frac{1}{\omega_r^2 - \omega^2 - i\alpha\omega(2\omega_0 + \omega_m(N_x + N_y))} \\
&= \frac{\omega_r^2 - \omega^2 + i\alpha\omega(2\omega_0 + \omega_m(N_x + N_y))}{(\omega_r^2 - \omega^2)^2 + \alpha^2\omega^2(2\omega_0 + \omega_m(N_x + N_y))^2} \\
&= \frac{1}{\gamma^2} \frac{\begin{array}{r}(H + M_0(N_y - N_z))(H + M_0(N_x - N_z)) - (H_r + M_0(N_y - N_z))(H_r + M_0(N_x - N_z)) \\ + i\dfrac{\alpha\omega}{\gamma}(2(H - N_z M_0) + M_0(N_x + N_y))\end{array}}{\begin{array}{r}((H + M_0(N_y - N_z))(H + M_0(N_x - N_z)) - (H_r + M_0(N_y - N_z))(H_r + M_0(N_x - N_z)))^2 \\ + \dfrac{\alpha^2\omega^2}{\gamma^2}(2(H - N_z M_0) + M_0(N_x + N_y))^2\end{array}}.
\end{aligned}$$

Since

$$\begin{aligned}
&(H + M_0(N_y - N_z))(H + M_0(N_x - N_z)) - (H_r + M_0(N_y - N_z))(H_r + M_0(N_x - N_z)) = \\
&\qquad [H + H_r + M_0(N_x + N_y - 2N_z)][H - H_r],
\end{aligned}$$

this becomes

$$F = \frac{1}{\gamma^2}\frac{[H + H_r + M_0(N_x + N_y - 2N_z)][H - H_r] + i\frac{\alpha\omega}{\gamma}(2(H - N_z M_0) + M_0(N_x + N_y))}{[H + H_r + M_0(N_x + N_y - 2N_z)]^2[H - H_r]^2 + \frac{\alpha^2\omega^2}{\gamma^2}(2(H - N_z M_0) + M_0(N_x + N_y))^2}$$
$$= \frac{1}{\gamma\alpha\omega[2(H - N_z M_0) + M_0(N_x + N_y)]}\left[\frac{\Delta H(H - H_r) + i\Delta H^2}{(H - H_r)^2 + \Delta H^2}\right], \tag{27}$$

where

$$\Delta H = \frac{2(H - N_z M_0) + M_0(N_x + N_y)}{H + H_r + M_0(N_x + N_y - 2N_z)}\frac{\alpha\omega}{\gamma}, \tag{28}$$

is the line width of the resonance. Similar to ω_r, since ΔH depends on the demagnetization factors, the line width will vary for different field configurations.

The expression for F contains an amplitude multiplied by two important line shape contributions, one a symmetric Lorentz contribution and one an antisymmetric dispersive contribution. By defining the Lorentz line shape L and the dispersive line shape D,

$$L = \frac{\Delta H^2}{(H - H_r)^2 + \Delta H^2},$$
$$D = \frac{\Delta H(H - H_r)}{(H - H_r)^2 + \Delta H^2}, \tag{29}$$

F can be written more compactly as

$$F = \frac{D + iL}{\gamma\alpha\omega[2(H - N_z M_0) + M_0(N_x + N_y)]}. \tag{30}$$

Since α is small the $i\alpha\omega$ term in Eq. 24 can be ignored and the susceptibility elements simplify to the final desired form which can be written in terms of L and D,

$$(\chi_{xx}, \chi_{xy}, \chi_{yy}) = (A_{xx}, A_{xy}, A_{yy})(D + iL). \tag{31}$$

Again as shown above $\chi_{xy} = -\chi_{yx}$ and the real amplitudes, A_{xx}, A_{xy} and A_{yy} are given by,

$$A_{xx} = \frac{\gamma M_0(M_0 N_y + (H - N_z M_0))}{\alpha\omega(2(H - N_z M_0) + M_0(N_z + N_y))},$$
$$A_{xy} = -\frac{M_0}{\alpha(2(H - N_z M_0) + M_0(N_z + N_y))},$$
$$A_{yy} = \frac{\gamma M_0(M_0 N_x + (H - N_z M_0))}{\alpha\omega(2(H - N_z M_0) + M_0(N_z + N_y))}. \tag{32}$$

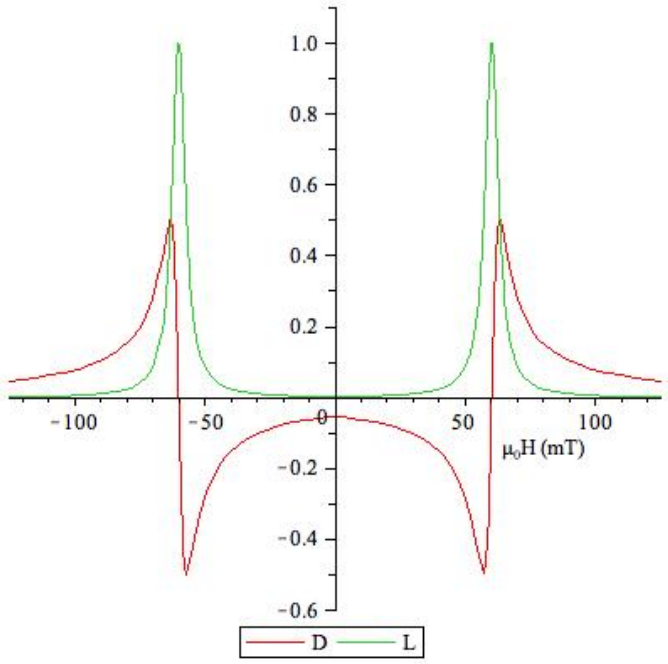

Figure 3: The Lorentz line shape is shown in green (light) and the dispersive line shape in red (dark) using $H_r = 60.1$ mT and $\mu_0 \Delta H = 3.1$ mT.

The susceptibility elements are complex valued functions of H and therefore also have an associated phase known as the spin resonance phase Θ,

$$\begin{aligned} tan(\Theta) &= \frac{Im(\chi_{xx})}{Re(\chi_{xx})} \\ &= \frac{\Delta H}{H - H_r}, \end{aligned}$$

which represents whether the driving force is in or out of phase with the magnetization precession and changes from 180° (driving force out of phase with precession) to 0° (driving force in phase) around resonance, going through 90° at resonance. This represents the universal feature of a resonance; the phase lags behind the driving force.

Since A_{xx}, A_{xy} and A_{yy} are real, the spin resonance phase can also be associated with the Lorentz and dispersive line shapes, $L \propto \sin(\Theta)$, $D \propto \cos(\Theta)$ so that $\tan(\Theta) = L/D$. Therefore the spin resonance phase information is carried by the line shape contributions L and D.

2.2.1 In-Plane and Out-of-Plane Susceptibilities

In the case of a thin film microstructure where the sample thickness is much less than the length and width, effectively resulting in a 2D plane, it is useful to define two field configurations, namely in-plane and out-of-plane, which can be used to experimentally excite FMR.

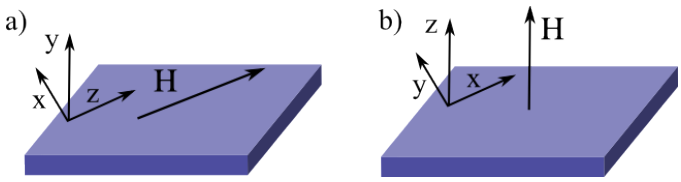

Figure 4: The two field configurations for a thin ferromagnetic film. Here **H** is the externally applied dc magnetic field. (a) In-plane field with coordinate system. (b) Out-of-plane field with coordinates.

In each case the form of the susceptibility can be determined from Eqs. 31 and 32 by using the appropriate demagnetization factors. For a thin film, the demagnetization factor is 1 perpendicular to the film, and 0 within the film. This can be understood by recalling that the demagnetization factors represent the field due to surface dipoles so that the largest effects will be where the sample is thinnest. Thus in the plane the thin film acts as an infinite plane when compared to the perpendicular direction. This means for the in-plane case shown in Fig. 4(a) $\mathrm{N}_x = 0, N_y = 1, N_z = 0$, and for the perpendicularly applied field of Fig. 4(b) $\mathrm{N}_x = 0, N_y = 0, N_z = 1$. The amplitudes A_{xx}, A_{xy}, A_{yy} and ΔH then become,

$$\begin{aligned} A_{xx} &= \frac{\gamma M_0(M_0 + H)}{\alpha\omega(2H + M_0)}, \\ A_{xy} &= -\frac{M_0}{\alpha(2H + M_0)}, \\ A_{yy} &= \frac{\gamma M_0 H}{\alpha\omega(2H + M_0)}, \\ \Delta H &= \left[\frac{2H + M_0}{H + H_r + M_0}\right]\frac{\alpha\omega}{\gamma}, \end{aligned} \tag{33}$$

for the in-plane field and,

$$
\begin{aligned}
A_{xx} &= \frac{\gamma M_0(H - M_0)}{\alpha\omega(2H + M_0)}, \\
A_{xy} &= -\frac{M_0}{\alpha(2H + M_0)}, \\
A_{yy} &= \frac{\gamma M_0(H - M_0)}{\alpha\omega(2H + M_0)}, \\
\Delta H &= \left[\frac{2(H - M_0)}{H + H_r - 2M_0}\right]\frac{\alpha\omega}{\gamma},
\end{aligned} \tag{34}
$$

for the perpendicular field. These same results have also been obtained by solving the Landau-Lifshitz equation without damping (Eq. 1) in a manner similar to the way in which we solved the Landau-Lifshitz-Gilbert equation with damping, and then introducing α by replacing ω_0 with $\omega_0 - i\alpha\omega$ [29] and applying the boundary conditions of Maxwell's equations at the thin film boundaries [31].

The choices made for the demagnetization factors also allow the resonance field to be calculated for the in-plane and out-of-plane configurations. For the in-plane field

$$\omega = \gamma\sqrt{H_r(H_r + M_0)}, \tag{35}$$

and for the out-of-plane field

$$\omega = \gamma(H_r - M_0). \tag{36}$$

2.3 Perpendicular Standing Spin Waves

Aside from ferromagnetic resonance which describes a uniform precession of spins across the ferromagnetic material, there can also be inhomogeneous ferromagnetic excitations with out of phase spin precession, known as spin waves. When such spin waves are spatially confined standing spin waves are produced. In a ferromangetic thin film, where the thickness is on the order of a few hundred nanometers and therefore the wavelength of the spin waves is small, the perpendicular standing spin waves arise due to the exchange interaction. This exchange interaction can be modeled by the addition of an exchange term [32],

$$\frac{2A\gamma}{M_0^2}(\nabla^2\mathbf{M}) \times \mathbf{M}, \tag{37}$$

into the Landau-Lifshitz equation, where A is a material dependent exchange stiffness.

The resulting equation which describes the spin waves is then

$$\frac{d\mathbf{M}}{dt} = -\gamma\mathbf{M} \times \mathbf{H}_i + \frac{2A\gamma}{M_0^2}(\nabla^2\mathbf{M}) \times \mathbf{M}. \tag{38}$$

Here the damping coefficient α has been set to zero since it will not effect the follow results. Damping may easily be included by the procedure described at the end of the previous section.

The dynamic magnetization will now have a spatial dependence and can be written as $\mathbf{m}e^{-i(\omega t+\mathbf{k}\cdot\mathbf{r})}$. Again separating $\mathbf{M}$ and $\mathbf{H}$ into dc and rf components we have $\mathbf{M} = \mathbf{M}_0+\mathbf{m}e^{-i(\omega t+\mathbf{k}\cdot\mathbf{r})}$ and $\mathbf{H}_i = \mathbf{H}_{0i}+\mathbf{h}_i e^{-i(\omega t+\mathbf{k}\cdot\mathbf{r})}$. Using $\frac{d\mathbf{M}}{dt} = -i\omega\mathbf{m}e^{-i(\omega t+\mathbf{k}\cdot\mathbf{r})}$, $\nabla^2\mathbf{M} = k^2\mathbf{m}e^{-i(\omega t+\mathbf{k}\cdot\mathbf{r})}$, $\mathbf{M}_0 \times \mathbf{H}_{0i} = 0$, $\mathbf{m} \times \mathbf{m} = 0$ and $\mathbf{m} \times \mathbf{h} = 0$ (since both $\mathbf{m}$ and $\mathbf{h}$ are small) so that $\mathbf{M} \times \mathbf{H}_i = \mathbf{M}_0 \times \mathbf{h}e^{-i(\omega t+\mathbf{k}\cdot\mathbf{r})} + \mathbf{m}e^{-i(\omega t+\mathbf{k}\cdot\mathbf{r})} \times \mathbf{H}_{0i}$ we have,

$$\mathbf{m} = \frac{\gamma}{i\omega}[\mathbf{m} \times (\mathbf{H}_{0i} + \frac{2Ak^2}{M_0^2}\mathbf{M}_0) + \mathbf{M}_0 \times \mathbf{h}_i]. \tag{39}$$

This has the same form as Eq. 12 with $\alpha = 0$ if we replace $\mathbf{H}$ with $\mathbf{H} + \mathbf{H}_{ex}$ where,

$$\mathbf{H}_{ex} = \frac{2Ak^2}{M_0^2}\mathbf{M}_0. \tag{40}$$

Using this replacement in Eq. 35 and Eq. 36, the standing spin wave resonance frequencies become

$$\omega = \gamma\sqrt{(H + H_{ex})(H + H_{ex} + M_0)}, \tag{41}$$

for the in-plane field and

$$\omega = \gamma(H + H_{ex} - M_0), \tag{42}$$

for the perpendicular field. In both cases the resonance frequency increases, which means that depending on the frequency range looked at, one may observe FMR without observing the perpendicular standing spin wave resonance (SWR).

2.4 Spin Rectification

Originally ferromagnetic resonance experiments were performed on bulk magnetic samples using resonance cavities where a sample would be placed in the cavity and the microwave intensity would be measured as a function of the applied magnetic field [1]. At resonance a strong absorption occurs in the sample causing a sharp decrease in the measured intensity, allowing a determination of the resonance field. This technique works remarkably well for bulk materials, and even for ferromagnetic thin films, but recently the improvement of fabrication techniques has enabled the production of thin film microstructures with dimensions small enough (on the order of 10 - 100 μm) that their effect on the intensity in the comparatively large cavity is negligible, requiring a new method of FMR detection. Fortunately the improvements in thin film fabrication have been complemented by the development of planar waveguide devices which allow precise delivery of the microwave field enabling a solution to the FMR problem by electrical detection. Such an electrical detection technique directly probes the sample

properties by detecting a voltage generated via the spin rectification effect, which produces a dc voltage through the non-linear coupling of rf electric and magnetic fields. It is this so called photovoltage which replaces the intensity measurement and whose line shape is of interest. While the line shape of the spin rectified voltage differs depending on the strength of the applied dc magnetic field, the source of the spin rectification effect is the generation of a dynamic resistance which in this work is a result of the anisotropic magnetoresistance exhibited by ferromagnets.

2.4.1 Anisotropic Magnetoresistance

The anisotropic magnetoresistance effect is found in ferromagnets and results in different resistivities parallel to and perpendicular to the magnetization. Typically the resistivity parallel to the magnetization, ρ, is higher than the perpendicular resistivity, $\rho+\rho_{AMR}$ [28]. These different resistivities cause the resistance to depend on the angle between the current and the magnetization, producing a dynamic resistance according to

$$R(H) = R(0) - \Delta R \sin^2(\theta_M), \tag{43}$$

where θ_M is the angle between the magnetization and current and ΔR is the resistance change due to the AMR effect. The resistance will depend on the static field H since $\theta_M = \theta_M(H)$.

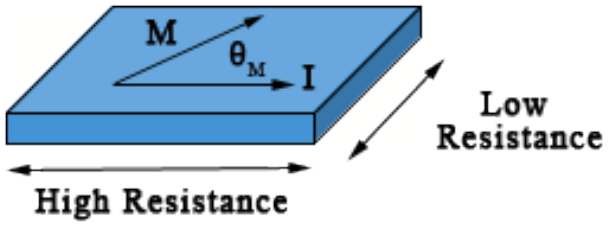

Figure 5: Anisotropic magnetoresistance effect, where the largest resistance is observed when the current and magnetization are parallel, and the smallest resistance occurs when they are perpendicular.

2.4.2 General Spin Rectified Voltage

To see how a voltage can arise due to the AMR effect, consider first the general case of a material under an applied field as described above, $\mathbf{H}_i = \mathbf{H}_{0i} + \mathbf{h}_i e^{-i\omega t}$. The

resistance under this field can be expanded in a Taylor series,

$$R(\mathbf{H}_i = \mathbf{H}_{0i} + \mathbf{h}_i e^{-i\omega t}) \approx R(\mathbf{H}_{0i}) + \mathbf{h}_i e^{-i\omega t} \cdot \nabla R(\mathbf{H}_{0i}), \tag{44}$$

where $\nabla R(\mathbf{H}_{0i})$ is the gradient of $R(\mathbf{H}_i)$ evaluated at $\mathbf{H}_{0i}$. The source of the dynamic resistance is for instance the anisotropic magnetoresistance. For a current $I = I_0 e^{-i\omega t}$ along the measurement direction a photovoltage will be generated

$$\begin{aligned} V &= \langle Re(I) \cdot Re(R(\mathbf{H}_{0i})) \rangle \\ &= \left\langle Re(I_0 e^{-i\omega t}) Re(\mathbf{h}_i e^{-i\omega t} \cdot \nabla R(\mathbf{H}_{0i})) \right\rangle . \end{aligned} \tag{45}$$

We see that whenever the resistance is a function of the applied field, and the field is not an extremum of $R(\mathbf{H}_{0i})$ (that is $\nabla R(\mathbf{H}_{0i}) \neq 0$) a photovoltage will in general be produced. This general spin rectification can be used to explain the photovoltage at low to zero magnetic fields due to magnetization rotation or magnetization switching which has already been shown to have applications to microwave imaging [33, 34].

2.4.3 Spin Rectified Voltage Near Resonance

To examine the exact form of the FMR line shape near resonance we consider the generalized Ohm's law [35] which is followed by the spin rectified voltage production,

$$\mathbf{J} = \sigma \mathbf{E}_0 - \frac{\sigma \Delta\rho}{\mathbf{M}^2}(\mathbf{J} \cdot \mathbf{M})\mathbf{M} + \sigma R_H \mathbf{J} \times \mathbf{M}. \tag{46}$$

The first term describes the normal Ohm's law where the current $\mathbf{J}$ is linearly related to the electric field $\mathbf{E}_0$ through the conductivity σ. The last two terms represent non-linear corrections to Ohm's law, where the second term describes anisotropic magnetoresistance (AMR), and the third describes the anomalous Hall effect. $\Delta\rho$ is the resistivity change corresponding to the AMR effect, and R_H is the anomalous Hall coefficient. Rewriting this equation as the sum of two fields we have

$$\mathbf{J} = \sigma(\mathbf{E}_0 + \mathbf{E}_1),$$

$$\mathbf{E}_1 = -\frac{\Delta\rho}{\mathbf{M}^2}(\mathbf{J} \cdot \mathbf{M})\mathbf{M} + R_H \mathbf{J} \times \mathbf{M}. \tag{47}$$

If $\mathbf{E}_0$ is an rf field it will time average to zero, but the higher order $\mathbf{E}_1$ will in general have a non-zero time average resulting in the so called rectified voltage. The applied field and the magnetization will be the same as in the determination of the dynamic susceptibility where a static magnetic field, $\mathbf{H}$ applied along the $\widehat{\mathbf{z}}$ direction, is used to create a static magnetization, $\mathbf{M}_0$ also in the $\widehat{\mathbf{z}}$ direction and an applied microwave field $h_K e^{-i\omega t} = h_k e^{-i\omega t + i\Phi_k} = h_k^t e^{i\Phi_k}$ will be used to induce oscillations about this equilibrium. Here Φ_k denotes the phase shift between the electric and magnetic fields in the kth direction. The magnetization is $\mathbf{M} = \mathbf{M}_0 + \mathbf{m}e^{-i\omega t}$ and as

we have seen this oscillating magnetization can be related to the applied field through the susceptibility tensor. To determine the photovoltage line shape we will use the notation $\mathbf{m}^t = Re(\mathbf{m}e^{-i\omega t})$.

Using these magnetization and feld expressions in Eq. 47, we find the microwave field as the time average of $\mathbf{E}_1$,

$$\begin{aligned}\mathbf{E}_{MW} = \langle \mathbf{E}_1 \rangle &= \frac{-\Delta\rho}{M^2} \left\langle (\mathbf{J}\cdot\mathbf{M}_0)\,\mathbf{M}_0 + (\mathbf{J}\cdot\mathbf{M}_0)\,\mathbf{m}^t + \left(\mathbf{J}\cdot\mathbf{m}^t\right)\mathbf{M}_0 + \left(\mathbf{J}\cdot\mathbf{m}^t\right)\mathbf{m}^t \right\rangle \\ &\quad + R_H \left\langle \mathbf{J}\times\mathbf{M}_0 + \mathbf{J}\times\mathbf{m}^t \right\rangle \\ &= \frac{-\Delta\rho}{M^2} \left\langle \left(\mathbf{J}\cdot\mathbf{m}^t\right)\mathbf{M}_0 + (\mathbf{J}\cdot\mathbf{M}_0)\,\mathbf{m}^t \right\rangle + R_H \left\langle \mathbf{J}\times\mathbf{m}^t \right\rangle . \end{aligned} \tag{48}$$

Eq. 48 gives the general microwave field expression from which the photovoltage and its line shape can be determined.

2.4.4 In-Plane H Field

As discussed previously there are two field configurations, namely in-plane and out-of-plane, which can be used to excite FMR. The line shape for each of these

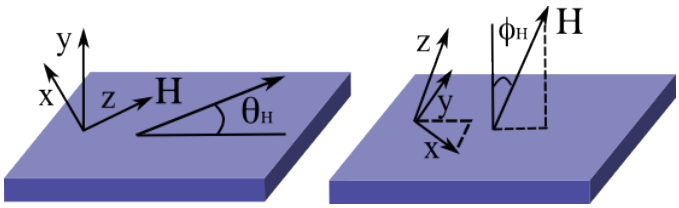

Figure 6: The two field configurations for a thin ferromagnetic film. Here **H** is the externally applied dc magnetic field, θ_H is the in-plane field angle and ϕ_H is the perpendicular field angle.

configurations can be determined from Eq. 48. In the case of an in-plane field we consider the two coordinate systems in Fig. 7. Here the dc field and resulting static magnetization are denoted by **H** and $\mathbf{M}_0$ respectively. The z axis is along the field direction while the z' axis is along the current direction. The two coordinate systems are related through the transformation,

$$\begin{pmatrix} \widehat{\mathbf{x}} \\ \widehat{\mathbf{y}} \\ \widehat{\mathbf{z}} \end{pmatrix} = \begin{pmatrix} \cos(\theta_H) & 0 & -\sin(\theta_H) \\ 0 & 1 & 0 \\ \sin(\theta_H) & 0 & \cos(\theta_H) \end{pmatrix} \begin{pmatrix} \widehat{\mathbf{x}'} \\ \widehat{\mathbf{y}} \\ \widehat{\mathbf{z}'} \end{pmatrix} . \tag{49}$$

Since rotation matrices are unitary we know that the matrix taking $(\widehat{\mathbf{x}}, \widehat{\mathbf{y}}, \widehat{\mathbf{z}})$ into $(\widehat{\mathbf{x}'}, \widehat{\mathbf{y}'}, \widehat{\mathbf{z}'})$ will simply be the transpose of the rotation matrix given in Eq. 49.

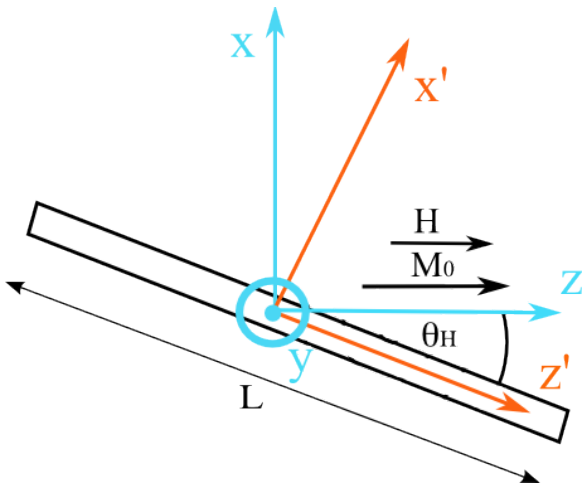

Figure 7: Coordinate systems for in-plane magnetic field.

Using this field configuration we have $\mathbf{m}^t = (\mathrm{m}_x^t,\ \mathrm{m}_y^t,\ 0)$ and due to the strip geometry the current flows along the z' direction and is given by $\mathbf{J} = \mathrm{j}_{z'}\cos(\omega t)\widehat{\mathbf{z}'}$. Using these expressions in Eq. 48, and transforming $\mathbf{m}^t$ to the primed coordinate system the time averaged microwave electric field is given by

$$\begin{aligned}\mathbf{E}_{MW} = &-\frac{\Delta\rho}{M^2}\left\langle -M_0 j_{z'}\cos(\omega t)m_x^t\sin(\theta_H)\left[\sin(\theta_H)\widehat{\mathbf{x}'}+\cos(\theta_H)\widehat{\mathbf{z}'}\right]\right\rangle \\ &-\frac{\Delta\rho}{M^2}\left\langle M_0 j_{z'}\cos(\omega t)\cos(\theta_H)\left[m_x^t\cos(\theta_H)\widehat{\mathbf{x}'}+m_y^t\widehat{\mathbf{y}}-m_x^t\sin(\theta_H)\widehat{\mathbf{z}'}\right]\right\rangle \\ &+R_H\left\langle -j_{z'}\cos(\omega t)m_y^t\widehat{\mathbf{x}'}+j_{z'}\cos(\omega t)m_x^t\cos(\theta_H)\widehat{\mathbf{y}}\right\rangle. \end{aligned} \tag{50}$$

To find the voltage in the ferromagnetic strip we then simply integrate the field along the length of the strip.

$$\begin{aligned}V &= \int_0^L \mathbf{E}_{MW}\cdot d\mathbf{z}' \approx L\mathbf{E}_{MW}\cdot\widehat{\mathbf{z}'} \\ &= \frac{\Delta R}{M}\left\langle I_{z'}\cos(\omega t)m_x^t\right\rangle\sin(2\theta_H).\end{aligned} \tag{51}$$

Here we have used $I_{z'} = Aj_{z'}$ and $\Delta R = \Delta\rho\frac{L}{A}$ where A is the cross sectional area.

We see that along the strip the voltage generated is due to the AMR effect and there is no voltage due to the Hall effect. However in the transverse direction there is a voltage generated by both the AMR and Hall effect, which can be determined by integrating Eq. 50 along the x' direction.

We know that m_x^t is related to the applied microwave field through the susceptibility tensor (Eq. 21). If we write the tensor elements in terms of the spin resonance

phase Θ we have $m_x^t = Re(|\chi_{xx}|e^{i\Theta}h_x + i|\chi_{xy}|e^{i\Theta}h_y^t)$. Using the coordinate rotation once again yields

$$\begin{pmatrix} h_x^t \\ h_y^t \\ h_z^t \end{pmatrix} = \begin{pmatrix} h_{x'}^t \cos(\theta_H) - h_{z'}^t \sin(\theta_H) \\ h_y^t \\ h_{x'}^t \sin(\theta_H) + h_{z'}^t \cos(\theta_H) \end{pmatrix}, \tag{52}$$

which gives

$$\begin{aligned} m_x^t &= Re\left[|\chi_{xx}|h_x e^{-i(\omega t - \Phi_x - \Theta)} + |\chi_{xy}|h_y e^{-i(\omega t - \Phi_y - \Theta - \frac{\pi}{2})}\right] \\ &= Re\left[|\chi_{xx}|h_{x'} e^{-i(\omega t - \Phi_{x'} - \Theta)}\cos(\theta_H) - |\chi_{xx}|h_{z'} e^{-i(\omega t - \Phi_{z'} - \Theta)}\sin(\theta_H) + |\chi_{xy}|h_y e^{-i(\omega t - \Phi_y - \Theta - \frac{\pi}{2})}\right] \\ &= |\chi_{xx}|h_{x'}\cos(\theta_H)[\cos(\omega t)\cos(\Phi_{x'} + \Theta) + \sin(\omega t)\sin(\Phi_{x'} + \Theta)] \\ &\quad - |\chi_{xx}|h_{z'}\sin(\theta_H)[\cos(\omega t)\cos(\Phi_{z'} + \Theta) + \sin(\omega t)\sin(\Phi_{z'} + \Theta)] \\ &\quad + |\chi_{xy}|h_y\left[\cos(\omega t)\cos(\Phi_y + \Theta + \frac{\pi}{2}) + \sin(\omega t)\sin\left(\Phi_y + \Theta + \frac{\pi}{2}\right)\right]. \end{aligned} \tag{53}$$

Combining Eq. 53 with the voltage expression in Eq. 51 and taking the time average gives the photo voltage expression for an in-plane applied magnetic field,

$$\begin{aligned} V = \frac{\Delta R}{2M_0} I_{z'} \sin(2\theta_H) \left[|\chi_{xx}|h_{x'}\cos(\theta_H)\cos(\Phi_{x'} + \Theta) - |\chi_{xx}|h_{z'}\cos(\Phi_{z'} + \Theta)\sin(\theta_H)\right. \\ \left. + |\chi_{xy}|h_y\cos\left(\Phi_y + \Theta + \frac{\pi}{2}\right)\right]. \end{aligned} \tag{54}$$

We can then write

$$\begin{aligned} &|\chi_{xx}|\cos(\Phi_{x'} + \Theta) = |\chi_{xx}|(\cos\Phi_{x'}\cos\Theta - \sin\Phi_{x'}\sin\Theta) = Re(\chi_{xx})\cos\Phi_{x'} - Im(\chi_{xx})\sin\Phi_{x'}, \\ &|\chi_{xx}|\cos(\Phi_{z'} + \Theta) = Re(\chi_{xx})\cos\Phi_{z'} - Im(\chi_{xx})\sin\Phi_{z'}, \\ &|\chi_{xy}|\cos(\Phi_y + \Theta + \frac{\pi}{2}) = -\sin(\Phi_y + \Theta) = -Re(\chi_{xy})\sin\Phi_y - Im(\chi_{xy})\cos\Phi_y. \end{aligned} \tag{55}$$

The real and imaginary parts of the susceptibility tensor elements can be determined from Eq. 31 so that we obtain the voltage in terms of symmetric and antisymmetric Lorentz contributions.

$$\begin{aligned} V = \frac{\Delta R}{2M_0} I_{z'} \sin(2\theta_H) \left[A_{xx}h_{x'}\cos\theta_H\left(\frac{\Delta H(H - H_r)}{(H - H_r)^2 + \Delta H^2}\cos\Phi_{x'} - \frac{\Delta H^2}{(H - H_r)^2 + \Delta H^2}\sin\Phi_{x'}\right)\right. \\ - A_{xx}h_{z'}\sin\theta_H\left(\frac{\Delta H(H - H_r)}{(H - H_r)^2 + \Delta H^2}\cos\Phi_{z'} - \frac{\Delta H^2}{(H - H_r)^2 + \Delta H^2}\sin\Phi_{z'}\right) \\ \left. - A_{xy}h_y\left(\frac{\Delta H(H - H_r)}{(H - H_r)^2 + \Delta H^2} sin\Phi_y + \frac{\Delta H^2}{(H - H_r)^2 + \Delta H^2}\cos\Phi_y\right)\right]. \end{aligned} \tag{56}$$

This voltage may be written as

$$V = \frac{\Delta R}{2M_0} I_{z'} \left[A_L L + A_D D\right], \tag{57}$$

where,

$$A_L = -A_{xx}h_{x'}\cos(\theta_H)\sin(2\theta_H)\sin(\Phi_{x'}) - A_{xy}h_y\sin(2\theta_H)\cos(\Phi_y) + A_{xx}h_{z'}\sin(\theta_H)\sin(2\theta_H)\sin(\Phi_{z'}),$$
$$A_D = A_{xx}h_{x'}\cos(\theta_H)\sin(2\theta_H)\cos(\Phi_{x'}) - A_{xy}h_y\sin(2\theta_H)\sin(\Phi_y) - A_{xx}h_{z'}\sin(\theta_H)\sin(2\theta_H)\cos(\Phi_{z'}), \tag{58}$$

and L and D are the Lorentz and dispersive line shapes respectively. This voltage expression shows that at certain field angles, $\theta_H = n\pi/2,\ n = 0, 1, 2, \ldots$, the voltage will be 0.

Eqs. 57 and 58 suggest a way to separate the relative phase in the x', y and z' directions. One can fit the FMR using Eq. 57 to determine A_L and A_D. θ_H can then be varied and A_L and A_D can be fit using Eq. 58. This allows a determination of $\Phi_{x'}, \Phi_y$ and $\Phi_{z'}$ based on the θ_H dependence of A_L and A_D.

In the appropriate experimental conditions, the dominant contribution to the driving microwave field will either be the $h_{x'}$ field or the h_y field and we may take $h_y \rightarrow 0$ and $h_{z'} \rightarrow 0$ or $h_{x'} \rightarrow 0$ and $h_{z'} \rightarrow 0$ respectively. This will simplify the A_L and A_D expressions. In the case that $h_{x'}$ dominates we have,

$$V_{x'} = -\frac{\Delta R}{2M_0} I_{z'} h_{x'} \sin(2\theta_H)\cos(\theta_H) A_{xx} \left[L\sin(\Phi_{x'}) - D\cos(\Phi_{x'})\right]. \tag{59}$$

From this expression we can see that the line shape changes from purely symmetric when $\Phi_{x'} = \frac{2n+1}{2}\pi \quad n = 0, 1, 2, \ldots$ to purely antisymmetric when $\Phi_{x'} = n\pi \quad n = 0, 1, 2, \ldots$

In the case when the h_y field dominates the voltage expression becomes,

$$V_y = -\frac{\Delta R}{2M_0} I_{z'} h_y \sin(2\theta_H) A_{xy} \left[L\cos(\Phi_y) + D\sin(\Phi_y)\right]. \tag{60}$$

In this case we see that the line shape changes from purely symmetric when $\Phi_y = n\pi \quad n = 0, 1, 2, \ldots$ to purely antisymmetric when $\Phi_{x'} = \frac{2n+1}{2}\pi \quad n = 0, 1, 2, \ldots$.

It is worth noting the features of Eq. 59 and Eq. 60 when $\Phi_k = 0$. When the precession is driven by the $h_{x'}$ field, the photovoltage line shape is completely antisymmetric when $\Phi_{x'}$ is 0, whereas when the precession is driven by the h_y field the line shape is completely symmetric when $\Phi_y = 0$. Aside from the symmetry properties under changes in Φ_k, the two voltage expressions in Eq. 59 and Eq. 60 also show interesting symmetries in the field angle θ_H. Since a change in sign of the static field, $\mathbf{H} \rightarrow$ -$\mathbf{H}$ corresponds to $\theta_H \rightarrow \theta_H + 180°$, we see that $V_{x'}(H) = -V_{x'}(-H)$, so that $V_{x'}$ is odd with respect to $\mathbf{H}$. On the other hand $V_y(H) = V_y(-H)$ so that V_y is even with respect to $\mathbf{H}$. This symmetry can be used as an indication that FMR is being driven by multiple $\mathbf{H}$ field components as the H and $-H$ FMR peaks may have different amplitudes and line shapes as a result of the different symmetries of $V_{x'}$ and V_y.

2.4.5 Out-of-Plane H Field

For an out-of-plane field we use the two coordinate systems shown in Fig. 8 where the two coordinate systems are related by,

$$\begin{pmatrix} \widehat{\mathbf{x}} \\ \widehat{\mathbf{y}} \\ \widehat{\mathbf{z}} \end{pmatrix} = \begin{pmatrix} \cos(\phi_H) & 0 & \sin(\phi_H) \\ 0 & 1 & 0 \\ -\sin(\phi_H) & 0 & \cos(\phi_H) \end{pmatrix} \begin{pmatrix} \widehat{\mathbf{x}'} \\ \widehat{\mathbf{y}} \\ \widehat{\mathbf{z}'} \end{pmatrix}, \tag{61}$$

which is simply the transpose of the in-plane rotation matrix.

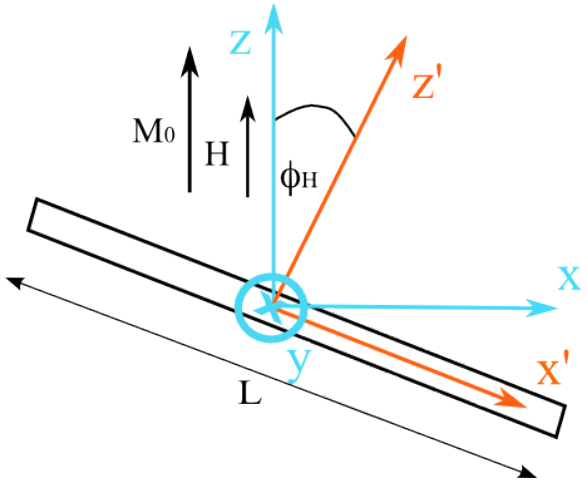

Figure 8: Coordinate systems for out-of-plane magnetic field.

In this case $\mathbf{M}_0 = (0,\, 0,\, \mathrm{M}_0)$, $\mathbf{m}^t = (\mathrm{m}_x^t,\, \mathrm{m}_y^t,\, 0)$ and $\mathbf{J} = \mathrm{j}_{x'} \cos(\omega t)\widehat{\mathbf{x}'}$. Using the coordinate rotation

$$\begin{aligned} \mathbf{M}_0 &= -M_0 \sin(\phi_H)\mathbf{x}' + M_0 \cos(\phi_H)\mathbf{z}', \\ \mathbf{m}^t &= m_x^t \cos(\phi_H)\mathbf{x}' + m_y^t \mathbf{y}' + m_x^t \sin(\phi_H)\mathbf{z}', \\ \mathbf{J} \times \mathbf{m}^t &= -j_{x'} \cos(\omega t) m_x^t \sin(\phi_H)\mathbf{y}' + j_{x'} \cos(\omega t)\mathbf{z}', \end{aligned}$$

so that

$$\begin{aligned} \mathbf{J} \cdot \mathbf{M}_0 &= -M_0 j_{x'} \sin(\phi_H) \cos(\omega t), \\ \mathbf{J} \cdot \mathbf{m}^t &= m_x^t j_{x'} \cos(\omega t) \cos(\phi_H), \end{aligned}$$

the microwave field is given by Eq. 48,

$$\begin{aligned} \mathbf{E}_{MW} = &\frac{\Delta\rho}{M^2} \left\langle (m_x^t j_{x'} \cos(\phi_H) \cos(\omega t) \left[-M_0 \sin(\phi_H)\mathbf{x}' + M_0 \cos(\phi_H)\mathbf{z}'\right] \right\rangle \\ &- \frac{\Delta\rho}{M^2} \left\langle M_0 j_{x'} \sin(\phi_H) \cos(\omega t) \left[m_x^t \cos(\phi_H)\mathbf{x}' + m_y^t)\mathbf{y}' + m_x^t \sin(\phi_H)\mathbf{z}'\right] \right\rangle \\ &+ R_H \left\langle -j_{x'} m_x^t \sin(\phi_H) \cos(\omega t)\mathbf{y}' + m_y^t j_{x'} \cos(\omega t)\mathbf{z}' \right\rangle, \end{aligned} \tag{62}$$

so that the photovoltage becomes,

$$V' = \int_0^L \mathbf{E}_{MW} \cdot d\mathbf{x}' \approx L\mathbf{E}_{MW} \cdot \mathbf{x}' \tag{63}$$

$$= \frac{\Delta R}{M} I_{x'} 2\sin(\phi_H)\cos(\phi_H)\left\langle m_x^t \cos(\omega t)\right\rangle. \tag{64}$$

In analogy with Eq. 53 we have,

$$\begin{aligned} m_x^t &= Re\left[|\chi_{xx}|h_{x'}e^{-i(\omega t-\Phi_{x'}-\Theta)}\cos(\phi_H) + |\chi_{xx}|h_{z'}e^{-i(\omega t-\Phi_{z'}-\Theta)}\sin(\phi_H) - |\chi_{xy}|h_y e^{-i(\omega t-\Phi_y-\Theta-\frac{\pi}{2})}\right] \\ &= |\chi_{xx}|h_{x'}\cos(\phi_H)[\cos(\omega t)\cos(\Phi_{x'}+\Theta)+\sin(\omega t)\sin(\Phi_{x'}+\Theta)] \\ &\quad + |\chi_{xx}|h_{z'}\sin(\phi_H)[\cos(\omega t)\cos(\Phi_{z'}+\Theta)+\sin(\omega t)\sin(\Phi_{z'}+\Theta)] \\ &\quad - |\chi_{xy}|h_y[\cos(\omega t)\cos(\Phi_y+\Theta+\frac{\pi}{2})+\sin(\omega t)\sin\left(\Phi_y+\Theta+\frac{\pi}{2}\right)]. \end{aligned} \tag{65}$$

so that the photovoltage is

$$\begin{aligned} V' = \frac{\Delta R}{2M_0} I_{z'}\sin(2\phi_H)[&|\chi_{xx}|h_{x'}\cos(\phi_H)\cos(\Phi_{x'}+\Theta) + |\chi_{xx}|h_{z'}\cos(\Phi_{z'}+\Theta)\sin(\phi_H) \\ &-|\chi_{xy}|h_y\cos\left(\Phi_y+\Theta+\frac{\pi}{2}\right)]. \end{aligned} \tag{66}$$

Again we can write,

$$\begin{aligned} &|\chi_{xx}|\cos(\Phi_{x'}+\Theta) = |\chi_{xx}|(\cos\Phi_{x'}\cos\Theta - \sin\Phi_{x'}\sin\Theta) = Re(\chi_{xx})\cos\Phi_{x'} - Im(\chi_{xx})\sin\Phi_{x'}, \\ &|\chi_{xx}|\cos(\Phi_{z'}+\Theta) = Re(\chi_{xx})\cos\Phi_{z'} - Im(\chi_{xx})\sin\Phi_{z'}, \\ &|\chi_{xy}|\cos(\Phi_y+\Theta+\frac{\pi}{2}) = -\sin(\Phi_y+\Theta) = -Re(\chi_{xy})\sin\Phi_y - Im(\chi_{xy})\cos\Phi_y. \end{aligned} \tag{67}$$

Then proceeding as before we find

$$V' = \frac{\Delta R}{2M_0} I_{z'}\left[A'_L L + A'_D D\right], \tag{68}$$

where

$$\begin{aligned} A'_L &= -A_{xx}h_{x'}\cos(\phi_H)\sin(2\phi_H)\sin(\Phi_{x'}) + A_{xy}h_y\sin(2\phi_H)\cos(\Phi_y) - A_{xx}h_{z'}\sin(\phi_H)\sin(2\phi_H)\sin(\Phi_{z'}), \\ A'_D &= A_{xx}h_{x'}\cos(\phi_H)\sin(2\phi_H)\cos(\Phi_{x'}) + A_{xy}h_y\sin(2\phi_H)\sin(\Phi_y) + A_{xx}h_{z'}\sin(\phi_H)\sin(2\phi_H)\cos(\Phi_{z'}). \end{aligned} \tag{69}$$

For precession driven by $h_{x'}$ the photovoltage becomes,

$$V'_{x'} = -\frac{\Delta R}{2M_0} I_{z'} A_{xx} h_{x'}\cos(\phi_H)\sin(2\phi_H)\left[\sin(\Phi_{x'})L - \cos(\Phi_{x'})D\right], \tag{70}$$

and for precession driven by h_y,

$$V_y' = \frac{\Delta R}{2M_0} I_{z'} A_{xy} h_y \sin(2\phi_H) \left[\cos(\Phi_y) L + \sin(\Phi_y) D\right]. \tag{71}$$

These expressions are very similar to the in-plane field expressions and have the same symmetry properties.

In this derivation we have used the dynamic susceptibility for the out-of-plane configuration which requires $N_x = N_y = 0$ and $N_z = 1$. This of course is only true if $\phi_H = 0$ in which case the voltage is actually 0. This means that while the expression in Eq. 66 is exact the expression in terms of L and D given in Eq. 68 is only true for small ϕ_H where $N_x \approx N_y \approx 0$ and $N_z \approx 1$. If we want this equation to be true in general we would need to determine the demagnetization factors as a function of ϕ_H.

Eq. 57 and Eq. 68 are the key results and give the desired expressions which describe the in-plane and out-of-plane FMR line shapes respectively. In both cases we see that the symmetry of the line shape depends on the value of the relative phase Φ_k. A feature common to both expressions is that at certain points of high symmetry there will be no voltage production. For both the in-plane and perpendicular configurations this occurs at $\theta_H,\ \phi_H = n\frac{\pi}{2},\ n = 0, 1, 2, \ldots$.

3 Experimental Techniques

3.1 Primary Experimental Setup

The main components of the measurement setup are an Agilent E8257D microwave generator which provides an rf field from 0.2 - 20 GHz, a Lakeshore EM 1375 electromagnet which produces the static magnetic field, and a Stanford Research SR830 DSP lock-in amplifier used to measure the dc voltage. The general set up is shown in Fig. 9 and is used for the $h_{x'}$, h_y and "well controlled" sample experiments described in the results section. The set up for both spintronic Michelson interferometry and the single permalloy ($Ni_{80}Fe_{20}$, Py) strip differ slightly and will be described in the next sections.

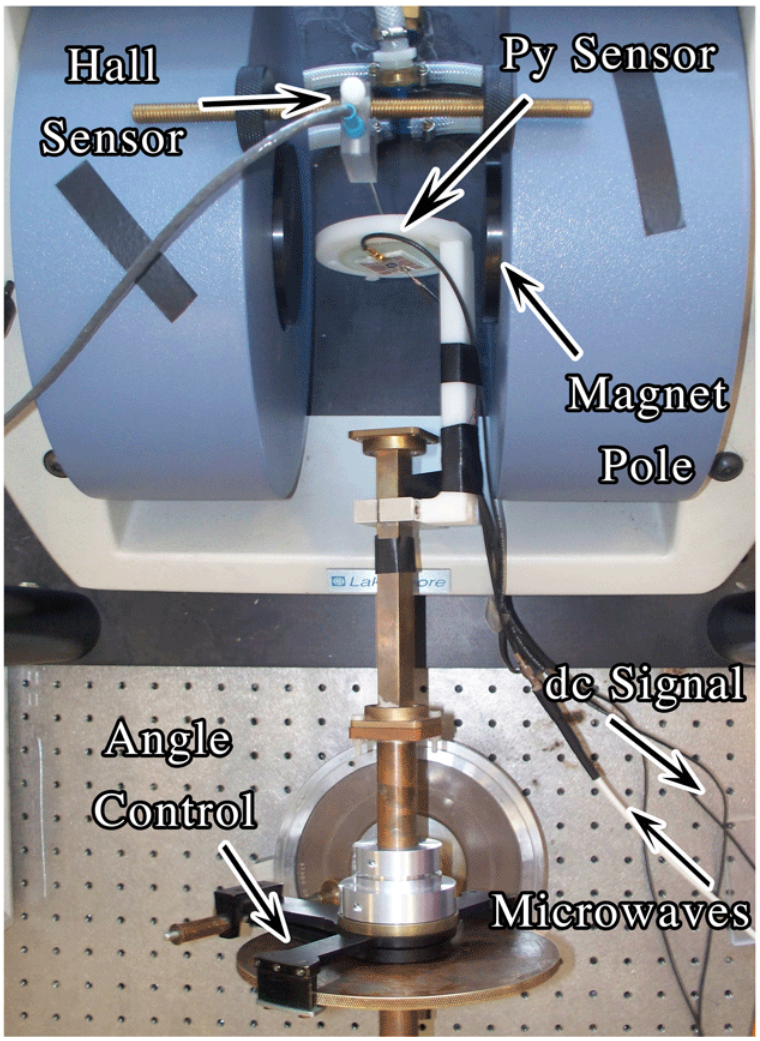

Figure 9: Experimental measurement set up.

As shown in Fig. 9, the static field is measured by a Hall probe and digital Gauss meter placed next to the sample in between the poles of the electromagnet. The electromagnet used to align the static magnetization is water cooled and can produce fields as high as 2 T depending on the air gap between the poles. However in this work the fields were in general less than 0.2 T. The sample holder allows effective rotations of the magnetic field angle θ_H, by more than 360° by rotating the waveguide and sample about the horizontal axis. The sample can also be rotated by 90° to allow both in-plane and perpendicular static fields, although we only consider the in-plane case here.

3.2 Spintronic Michelson Interferometry

The difficulties associated with a direct measurement of the relative electromagnetic phase have long prohibited experimentally probing Φ. However the novel technique of spintronic Michelson interferometry allows such a measurement by transforming the well known Michelson interferometry technique into a powerful phase resolved spintronic probe [6]. This technique has the ability to coherently measure both the electro and magneto dynamic processes at the same time, in the same ferromagnetic sample, and it is this capability which can be used to probe Φ.

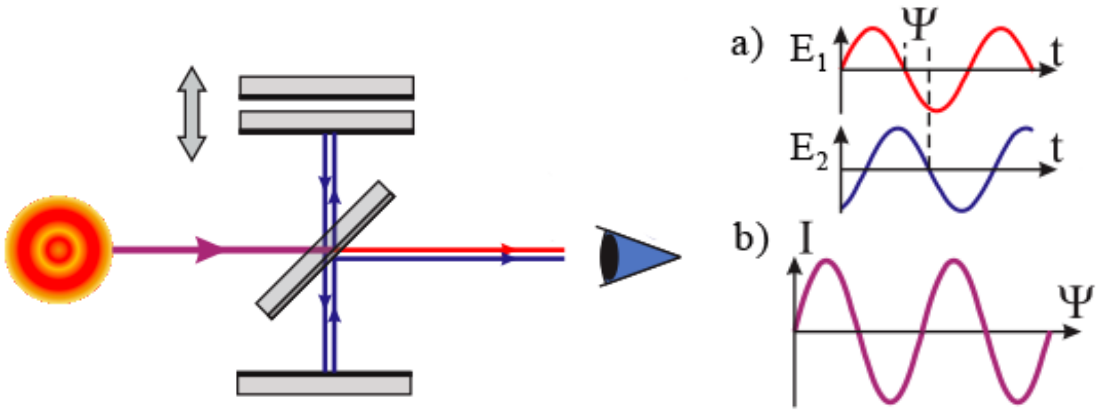

Figure 10: Classical Michelson Interferometer. (a) The two electric fields and their phase shift Ψ which results in the interference pattern in (b).

As shown in Fig. 10, classical Michelson interfometry, which was developed from the Michelson-Morley experiment [36] uses a path length difference between waves to generate an interference pattern which can be used to determine the phase shift Ψ between two electric fields. In contrast spintronic Michelson interferometry as shown in Fig. 11 controls the relative electromagnetic phase between the electric and magnetic fields in order to probe the material induced phase shift Φ between electric and magnetic fields at the permalloy sensor. The microwave signal is separated into

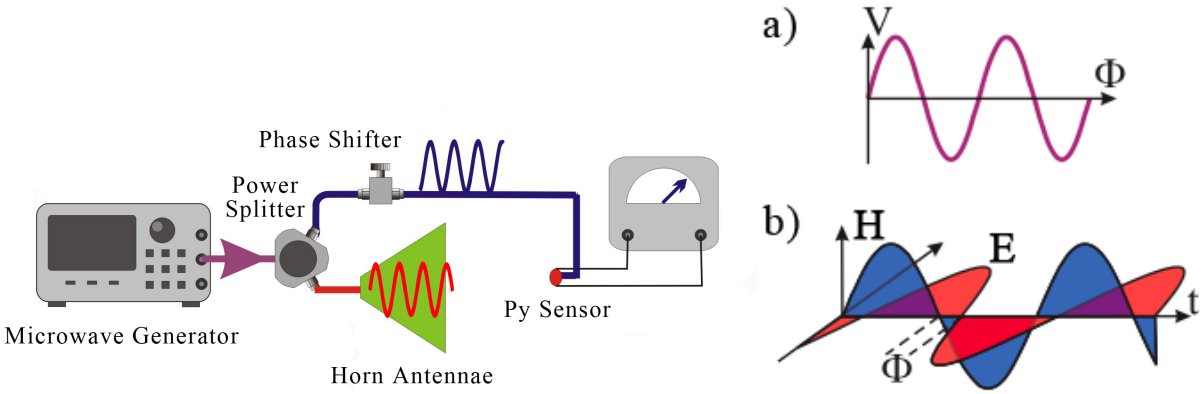

Figure 11: Spintronic Michelson Interferometer. (a) The photovoltage signal measured as a function of Φ which is produced by the coupling of the fields shown in (b).

two paths by an rf power splitter. One path travels through a phase shifter and is directly injected into the sensor, while the other path can either be injected into a CPW or shone on the sensor from a horn antennae (in Fig. 11 the horn antennae setup is shown). The magnetic field drives magnetization precession in the strip while the directly injected electric field produces a current. These two fields couple to produce a non-zero dc voltage via the spin rectification effect which can be detected by the lock-in amplifier. By controlling the phase through the phase shifter inserted in one path, Φ can effectively be controlled and a signal analogous to the one shown in Fig. 11(a) can be measured. This allows the determination of Φ for the system. By sweeping the externally applied magnetic field an FMR spectra can also be obtained in the same system.

3.3 Lock-in Amplification

Since the voltages produced through the spin rectification effect based on anisotropic magnetoresistance are quite small ($\sim$ 100 nV - a few μV depending on field strength and microwave power) due to the small resistance change ΔR, (<1%) the small dc signal will be obscured by background noise and a special technique is needed to extract the signal from the background. The technique commonly used is lock-in amplification which can result in excellent sensitivity; $\sim$ 5 nV noise. By modulating the input signal with a low frequency square wave set at some reference frequency, the dc output from the Py strip will also be modulated at the same frequency. However the noise will be unaffected. The lock-in amplifier then multiplies this signal by a sine wave of frequency equal to the reference frequency and averages over the signal using a low pass filter. Since sine waves of different frequencies are orthogonal, the noise will average to zero and only the signal at the reference frequency

will remain. Thus the small dc signal can be measured with minimal background noise. This process is schematically shown in Fig. 12 which shows the ideal case of a pure dc signal out which could then be measured directly. However the actual signal also includes noise of various frequencies and cannot be measured directly, so the lock-in must be used to help remove the noise before it can measure the dc signal.

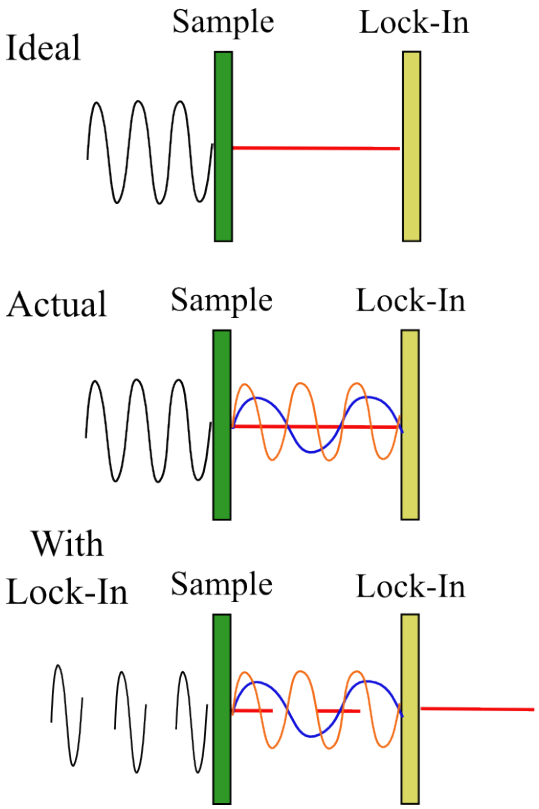

Figure 12: Schematic illustration showing the purpose of the lock-in amplifier. The output dc signal also contains noise components at different frequencies which must be filtered.

4 Experimental Results

In this section we present experimental results from six different samples which are used to demonstrate the combined effect that the field component used to drive FMR and the relative phase have on the FMR line shape. We also show how to determine the relative phase and separate the contributions from the different **h** field components driving FMR. First we present data using spintronic Michelson interferometry to show the effect of controlling the relative phase and how the line shape changes with changing phase. We then show samples where $h_y, h_{x'}$ and an arbitrary **h** field drive FMR and finally look at the FMR in two Py strips in a first generation spin dynamo to show that even in well controlled samples, the relative phase needs to be calibrated.

4.1 In-Plane Spintronic Michelson Interferometry

To illustrate the effect that a changing phase has on the FMR line shape, we first show results from experiments recently featured in two papers highlighting the spintronic Michelson interferometry technique [33, 34].

The experimental setup for the first experiment is shown in Fig. 13(a) where the signal from a broadband microwave generator is split into two paths by a microwave power splitter. Path A contains a WR90 waveguide and a horn antennae which shines on the sensor; a first generation spin dynamo consisting of two Py strips between the G and S strips of a G-S-G coplanar waveguide (CPW). Path B is directly connected to one port of the G-S-G CPW through an ATM P1607 phase shifter. The effect of the interference of path A and B can be seen in Fig. 13(c) at $\mu_0 H = 60$ mT and $\theta_H = 45°$.

The key point we wish to highlight is illustrated in Fig. 14. Here the FMR line shape is observed for different $\Phi_{x'}$ at $\omega/2\pi = 8$ GHz and $\theta_H = 45°$. Since the dominant driving field is the $h_{x'}$ field the results are fit to Eq. 59 using $\mu_0 H_r = 69.2$ mT and $\mu_0 \Delta H = 2.3$ mT, which allows a determination of $\Phi_{x'}$. As Fig. 14 shows, the line shape changes from almost purely symmetric at $\Phi_{x'} = 90.0°$ to almost purely dispersive at $\Phi_{x'} = -5.2°$ and back to almost purely symmetric at $\Phi_{x'} = -86.4°$. This agrees with the symmetry properties expected for FMR driven by an $h_{x'}$ field according to Eq. 59. The phase increment of 13.6° corresponds to half a turn on the ATM P1607 phase shifter.

A similar experiment has also been performed without a horn waveguide using a second generation spin dynamo, where both signals are connected directly to the sensor as shown in Fig. 15. The second generation spin dynamo consists of a Cu/Cr CPW on top of a $300 \times 7 \times 0.1$ μm Py microstrip with a 200 nm SiO_2 layer between the CPW and Py for insulation. Again the driving field is the $h_{x'}$ field produced from the CPW and the line shape shows the corresponding nearly dispersive line shape at $\Phi_{x'} \sim 0°$ and nearly Lorentz line shape at $\Phi_{x'} \sim 90°$ as shown in Fig. 16, where

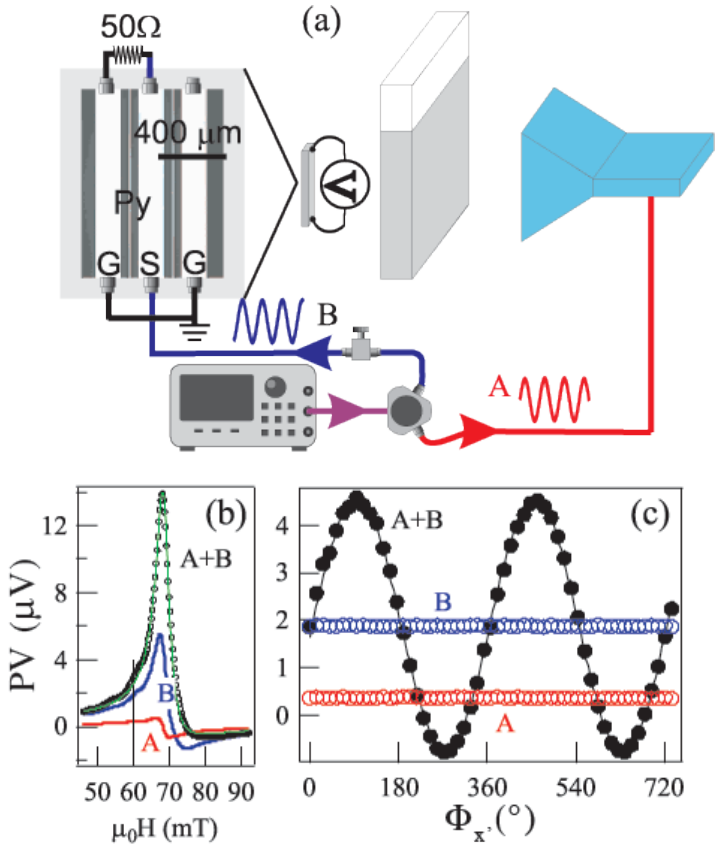

Figure 13: (a) Measurement set up to perform spintronic Michelson interferometry using horn antennae field. (b) FMR photovoltage line shape at $\omega/2\pi = 8$ GHz when paths A and B are connected separately and together. Signal from A + B is much larger due to the coupling between the rf magnetization driven by the magnetic field from A and the rf current driven by the electric field from B. From this line shape one finds $\mu_0 H_r = 68.7$ mT and $\mu_0 \Delta H = 2.3$ mT. (c) Photovoltage signal showing a sinusoidal oscillation with $\Phi_{x'}$ only appears when both paths are on.

the data at $\omega/2\pi = 4.8$ GHz and $\theta_H = 75°$ was fit to Eq. 59 using $\mu_0 H_r = 30.8$ mT and $\mu_0 \Delta H = 3.1$ mT. The steps in $\Phi_{x'}$ are larger than the experiment using the horn antennae since the change in frequency results in a half turn of the phase shifter corresponding to a larger change in $\Phi_{x'}$.

Both of these cases demonstrate that by controlling the relative phase the line shape of the FMR will change as described by Eq. 57. Now we turn to our systematic study of the **h** field component and Φ_k contributions to the FMR line shape.

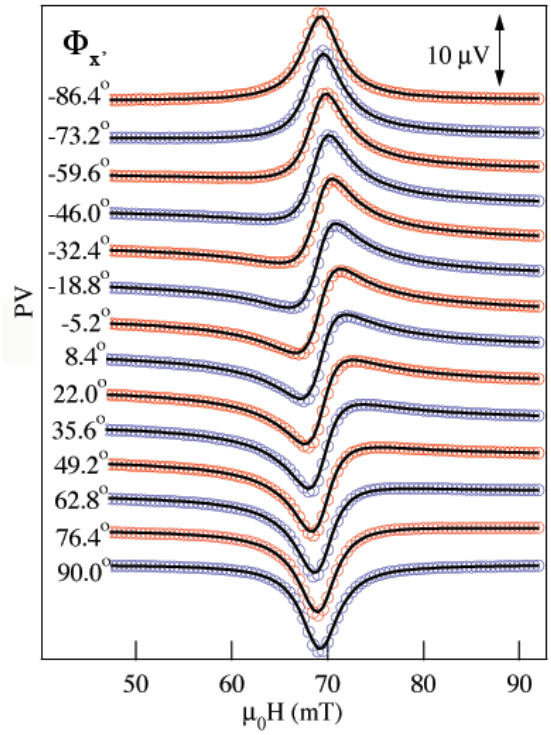

Figure 14: (a) Phase resolved FMR spectra. Circles are experimental data and solid lines are fits according to Eq. 59 using $\mu_0 H_r = 69.2$ mT and $\mu_0 \Delta H = 2.3$ mT. A striking change in line shape is observed when $\Phi_{x'}$ is changed.

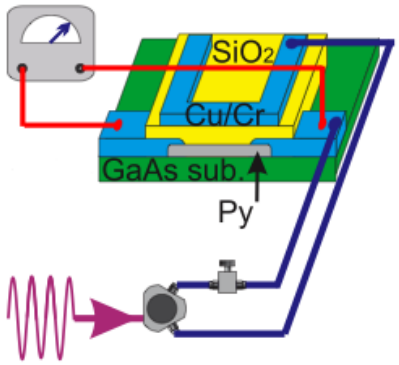

Figure 15: Second generation spin dynamo in spintronic Michelson interferometer. The microwave signal is coherently split into two paths which go to the CPW and Py strip. Again the relative phase is controlled by inserting a phase shifter into one path.

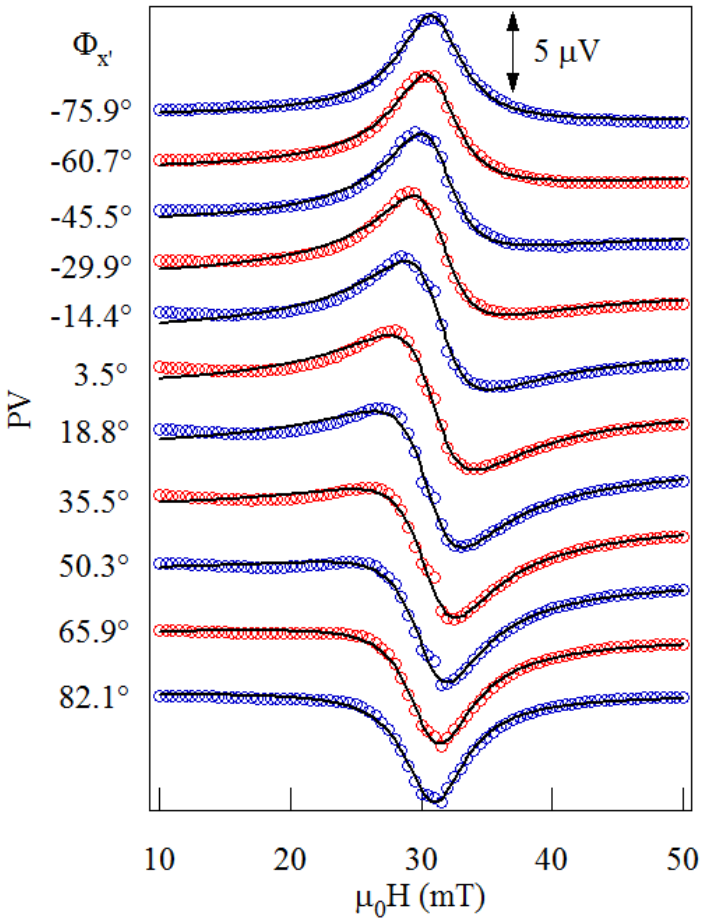

Figure 16: Phase resolved FMR spectra. Circles are experimental data and solid lines are fits according to Eq. 59 using $\mu_0 H_r = 30.8$ mT and $\mu_0 \Delta H = 3.1$ mT.

4.2 FMR Driven by h_y Field

In order to use the h_y field to drive FMR a first generation sample was used where a Cu/Cr coplanar waveguide (CPW) was fabricated beside a Py microstrip with dimension 300 μm $\times$ 20 μm $\times$ 50 nm on a semi-insulating SiO_2/Si substrate as shown schematically in Fig. 17(a). A microwave current is directly injected into the CPW and flows in the z' direction inducing a current in the Py strip also along the z' axis. In this geometry the dominant rf magnetic field in the Py will be the Oersted field in the $-y$ direction produced according to Ampère's Law. This field will induce FMR precession with the same amplitude regardless of the static **H** orientation, that is, since we are driving precession with the h_y field, the voltage V_y will be symmetric with respect to the static field **H** as described previously.

In this sample the AMR effect produces a resistance change of $\sim$ 0.4 % and depends on the orientation of the magnetization according to Eq. 43. When **H** is

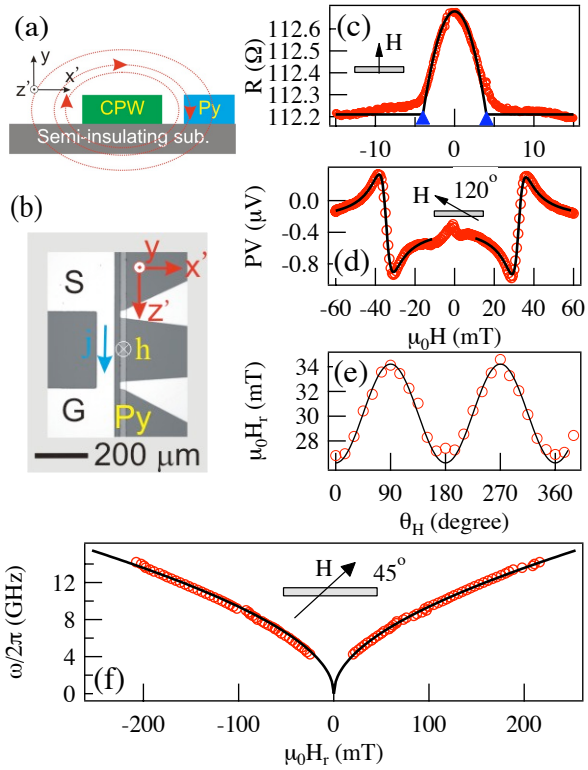

Figure 17: (a) Schematic diagram of the first generation Py/CPW sample where the Py strip is located beside the CPW. The dominate magnetic field in the Py is the Oersted field in the $-y$ direction due to the current in the CPW. (b) Micrograph of the Py/CPW device. (c) Magnetoresistance at $\theta_H = 90°$. Resistance change due to AMR is seen to be $\sim 0.4\%$. Arrows denote the anisotropic field, $H_A = 4.0$ mT. Open circles are experimental data and solid curve is the fitting result using $R(0) = 112.66\ \Omega, \Delta R = 0.47\ \Omega, H_A = 4.0$ mT. (d) Electrically detected FMR at $\theta_H = 120°$ and $\omega/2\pi = 5$ GHz showing an almost purely dispersive line shape ($\Phi_y \sim 90°$). Fit is according to Eq. (60) with $\mu_0 \Delta H = 3.6$ mT, $\mu_0 H_r = 32.2$ mT. (e) Oscillating H_r dependence on the static field direction θ_H with amplitude $2H_A$. (f) Dependence of FMR frequency on the resonant field H_r at $\theta_H = 45°$. Open circles are experimental data and the solid line is the fit according to $\omega = \gamma\sqrt{|H_r|(|H_r| + M_0)}$.

applied along the x' axis, the in-plane hard axis, the magnetization $\mathbf{M}$ tends to align toward the static field $\mathbf{H}$ and the angle θ_M is related to H and H_A by $\sin(\theta_M) = H/H_A$ for $H < H_A$. This means that for $H < H_A$, Eq. 43 becomes $R(H) = R(0) - \Delta R(H^2/H_A^2)$ as shown in Fig. 17(c) where the symbols are data and the solid curve is a fit using $R(0) = 112.66\ \Omega$, $\Delta R = 0.47\ \Omega$ and $H_A = 4.0$ mT. $H_A = N_{x'} M_0$ is the in-plane shape anisotropy field with $N_{x'} = 0.004$.

Fig. 17(d) shows that the line shape at $\theta_H = 120°$ is almost purely dispersive,

indicating that $\Phi_y \sim 90°$ according to Eq. (60). The θ_H dependence of H_r is shown in Fig. 17(e) and can be well fit by the function

$$\omega = \gamma\sqrt{(|H_r| + H_A\cos(2\theta_H))[|H_r| + M_0 - H_A(1+\sin^2(\theta_H)]}$$

by taking the shape anisotropy field H_A along the x' axis into account. As expected the amplitude of these oscillations is $H_A = 4.0$ mT. The frequency dependence of H_r is shown in Fig. 17(f) and is fit using $\omega = \gamma\sqrt{|H_r|(|H_r| + M_0)}$ (Eq. 35) with $\gamma/2\pi = 29.0$ μ_0GHz/T and $\mu_0 M$=1.0 T.

By systematically measuring the line shape as a function of the microwave frequency, we observe the interesting results of Fig. 18. The FMR line shape is observed to change from almost purely dispersive at $\omega/2\pi = 5$ GHz to almost purely symmetric at $\omega/2\pi = 5.56$ GHz. As discussed before, the line shape may be effected by the **h** orientation *i.e.* the different **h** vector components will effect the line shape differently, and if changing the **h** orientation changes the dominant driving field, the line shape may change. To rule out the possibility that the changes in the line shape in Fig. 18 were due to the **h** field orientation an experiment was performed to measure the line shape at several θ_H for each ω. The results are shown on the right hand side of Fig. 18 which shows the sinusoidal curves for the Lorentz, A_L, and dispersive A_D, amplitudes (dashed/blue and solid/red curves respectively) as a function of the static field angle θ_H. At $\omega/2\pi = 5$ GHz the amplitude of A_D is approximately one order of magnitude larger than A_L, while at $\omega/2\pi = 5.56$ GHz A_D is nearly 2 orders of magnitude less than A_L, as shown in Fig. 19(a). As expected the Lorentz and dispersive amplitudes are found to follow a $\sin(2\theta_H)$ dependence on the field angle in agreement with Eq. (60) indicating that the magnetization precession is indeed dominantly driven by the h_y field. Therefore the only factor causing the change in A_L/A_D is the relative phase of the electric and magnetic fields. The reversal of line shape symmetry observed by changing the frequency shows that in a microwave frequency range as narrow as 0.6 GHz, the relative phase Φ_y can change by 90° indicating a strong dependence of the relative phase on the frequency for this sample.

This large change of Φ_y may be surprising but can be explained by the large microwave wavelength compared to the sample size. Microwaves at ~ 5 GHz have wavelengths on the order of a few centimeters which is much larger than the sub-millimeter sample dimensions. Consequently the microwave propagation depends strongly on the boundary conditions of Maxwell's equations which physically include the bonding wire, chip carrier, as well as the sample holder and even the magnet. For this reason the magnetic field is not necessarily in phase with the electric field as most people believe and depending on the unique wave distribution in the Py sample, the relative phase Φ_y can take on any value. This is similar to the microwave propagation in a waveguide where the field distribution *i.e.* the waveguide modes, are known to depend strongly on boundary conditions and frequency.

We emphasize here that although such a wave propagation problem has many variables making it too complex to simulate, one can expect that Φ_y should be smoothly

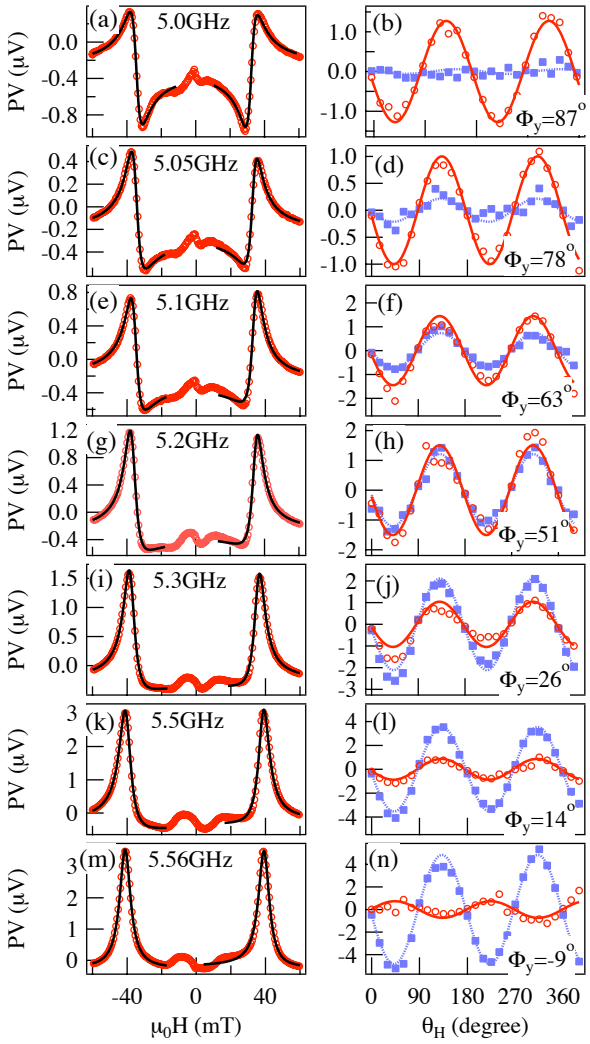

Figure 18: Data shown for a first generation sample. FMR spectra for several frequencies from 5.0 to 5.56 GHz with corresponding Lorentz and dispersive amplitudes as a function of θ_H. Circles and squares indicate the Lorentz and dispersive amplitudes of Eq. (60) respectively and show a $\sin(2\theta_H)$ dependence as expected. Solid and dashed curves are $\sin(2\theta_H)$ functions.

changing with microwave frequency. This effect is demonstrated in Fig. 19, where the line shape changes from pure dispersive at 5 GHz to pure Lorentz at 5.6 GHz with a step size of 0.01 GHz. Interestingly, even in such a small frequency range Φ_y is not monotonously varying with microwave frequency, therefore for a certain frequency the phase has to be determined by such a θ_H dependent measurement.

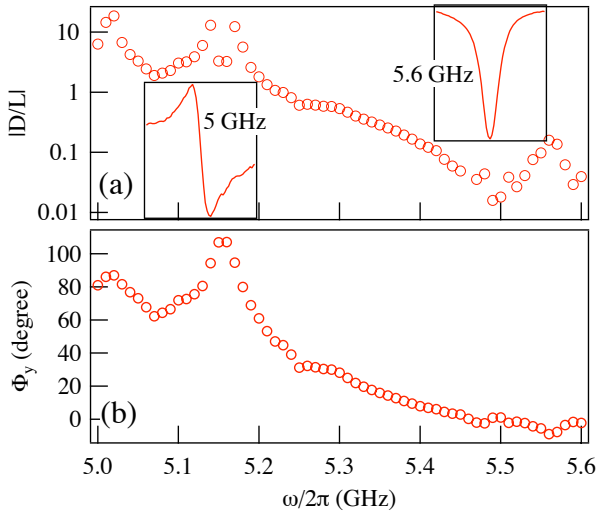

Figure 19: (a) The A_D/A_L ratio as a function of $\omega/2\pi$ showing the line shape change from dispersive at 5 GHz (left inset) to Lorentz at 5.6 GHz (right inset) with a step size of 0.01 GHz. (b) Φ_y dependence on $\omega/2\pi$ over same frequency interval showing the same dependence as A_D/A_L.

4.3 FMR Driven by $h_{x'}$ Field

In order to drive the FMR using the rf field in the x' direction, $h_{x'}$, a second generation sample was fabricated with the Py strip underneath the CPW as shown in Fig. 20(a). In this case the 300 μm $\times$ 70 μm $\times$ 100 nm Py strip is underneath the Cu/Cr coplanar waveguide which is fabricated on a SiO_2/Si substrate. Again a microwave current is directly injected into the CPW and induces a current in the z' direction in the Py strip. The dominant rf field in the Py is still the Oersted field, but due to the new geometry it is in the x' direction. Due to the smaller width and larger thickness, the demagnetization factor, $N_{x'} = 0.008$ is twice that in the first generation sample. This corresponds to $H_A = 8.0$ mT as indicated by the broader AMR curve in Fig. 20(c). This value is further confirmed by the amplitude of the H_r vs θ_H plot shown in Fig. 20(e).

Fig. 20(f) shows the frequency dependence of H_r for FMR (circles/red) and for the first perpendicular standing spin wave resonance (triangles/blue). The frequency dependence of H_r follows Eq. 41 with $\gamma/2\pi = 29.0$ μ_0GHz/T, $\mu_0 H_{ex} = 30$ mT and $\mu_0 M_0 = 1.0$ T. Since $k^2 \propto 1/d^2$, where d is the sample thickness, the exchange field, $H_{ex} \propto 1/d^2$ in accordance with Eq. 40. Therefore H_{ex} is much larger in the first generation sample compared to the second generation sample due to the difference in thickness. This can explain why such a standing SWR does not appear in Fig. 17(f), since a higher ω would be needed.

The frequency dependence of the line shape has also been observed for the second generation sample and is shown for a single frequency $\omega = 8$ GHz, in Fig. 21(b).

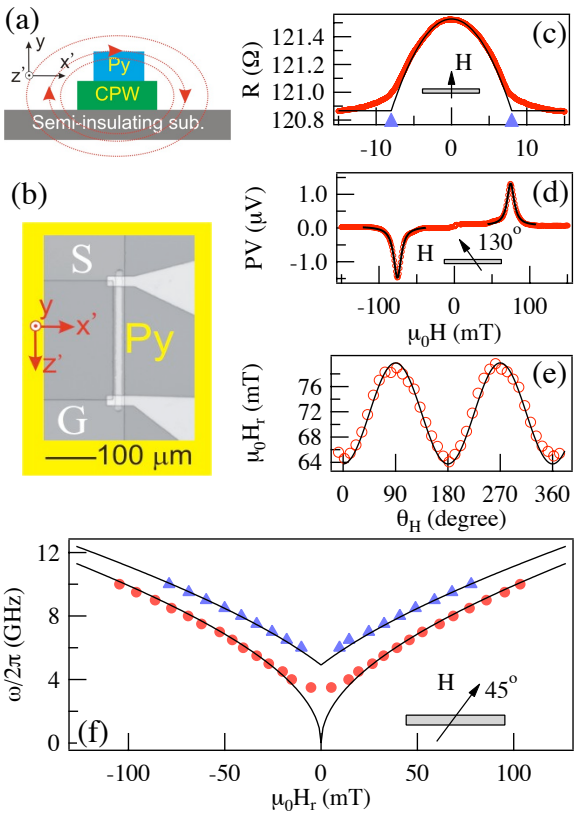

Figure 20: (a) Schematic diagram of the second generation Py/CPW sample where the Py strip is located underneath the CPW. In this case the dominate magnetic field in the Py is the Oersted field in the x' direction due to the field in the CPW. (b) Micrograph of the Py/CPW device. (c) Magnetoresistance at $\theta_H = 90°$. AMR is seen to be $\sim 0.5\%$. Arrows denote the anisotropic field, $H_A = 8.0$ mT. Open circles are experimental data and solid curve is the fitting result using $R(0) = 121.53\ \Omega$ and $\Delta R = 0.66\ \Omega$. (d) Electrically detected FMR at $\theta_H = 130°$ and $\omega/2\pi = 8$ GHz showing a symmetric Lorentz line shape. Fit is according to Eq. (60) with $\Delta H = 6.0$ mT , $H_r = 76.5$ mT and $\Phi_{x'} = 90°$. (e) Oscillating H_r dependence on the static field direction θ_H with amplitude $2H_A$. (f) Dependence of FMR frequency on the resonant field H_r at $\theta_H = 45°$. Open circles show the FMR frequency dependence while the open triangles are the standing SWR frequency dependence. The solid line is a fit to $\omega = \gamma\sqrt{|H_r|(|H_r| + M_0)}$.

The FMR has been observed to have any line shape between a symmetric Lorentz line shape and an antisymmetric dispersive line shape, similar to the first generation sample. While the relative phase shift and hence the line shape is expected to be frequency dependent, the line shape is not expected to depend on the static field direction θ_H when the FMR is driven by a single **h** component. This is confirmed in

Fig. 21(a) which shows the line shape using a second generation sample for several values of θ_H in 10° increments. The data can be fit well using Eq. (59) with a constant $\Phi_{x'} = 78°$ for all θ_H. This is evidence that the FMR is driven by a single **h** component, in this case the $h_{x'}$ field, and that $\Phi_{x'}$ does not depend on θ_H.

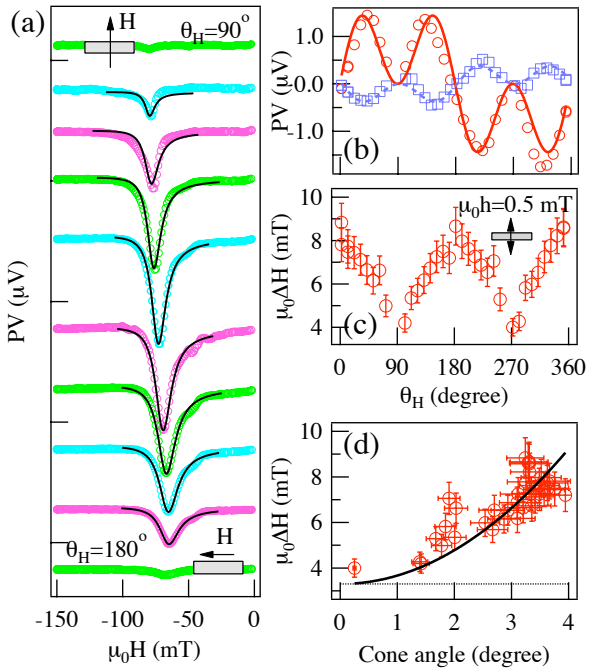

Figure 21: Data shown for a second generation sample. (a) FMR line shape at fixed frequency, $\omega/2\pi = 8$ GHz for several θ_H from 90° to 180° in steps of 10°. Open circles are experimental data and solid lines are fits using Eq. (59) with $\Phi_{x'} = 78°$ fixed. (b) A_D and A_L shown in squares and circles respectively as a function of θ_H. Fitting curves are $\sin(2\theta_H)\cos(\theta_H)$ functions. (c) ΔH for several values of θ_H showing an oscillation with θ_H. (d) Non-linear dependence of line width ΔH on the cone angle. Dashed line is the expected linear Gilbert damping whereas the data follows the quadratic dependence shown by the solid line.

In Fig. 21(b) the θ_H dependence of A_L and A_D (solid/circles and dashed/squares respectively) is shown. The circles and squares are experimental data while the solid and dashed lines are fitting results using a $\sin(2\theta_H)\cos(\theta_H)$ function according to Eq. (59), showing that the **h** field contributions can be separated based on a θ_H measurement and providing further evidence that the $h_{x'}$ field is responsible for driving the FMR in this sample. On the other hand one cannot use such a simple θ_H measurement to distinguish the spin rectification effect and the spin-pumping effect in an $h_{x'}$ dominant configuration since they both follow the same θ_H dependence [12].

There is a discrepancy between the solid curves and the experimental data from 45° - 135° where the experimental data is greater than the fitting curve and from 0° -

45° and 145° - 180° where the curve is greater than the experimental data. This effect can be explained by the non-linear damping, which has a quadratic dependence on the precession cone angle, $\theta \sim h_{x'}\cos(\theta_H)/\Delta H$. The fact that ΔH shows a dependence on θ_H can actually be seen in Fig. 21(a) where there seems to be an increase in ΔH with increasing θ_H, which is confirmed by the fitting. Indeed ΔH shows a strong dependence on θ_H which is illustrated in Fig. 21(c), and is enhanced by more than 100% from 4.0 mT at about 90° to 9.0 mT at about 180°. At $\theta_H = 0°$, $\theta \sim h_{x'}/\Delta H$ and the cone angle is its largest. As θ_H increases from 0° and moves toward 90°, θ decreases to 0° indicating a linear Gilbert damping. From Fig. 21(c) the cone angle can be calculated as a function of ΔH which is plotted in Fig. 21(d). Here the dashed line is a linear plot which would be expected in the linear damping regime. However the line width follows a quadratic dependence on the cone angle as shown with the solid line, indicating non-linear damping characterized by an increase of ΔH corresponding to an increase in the cone angle. Therefore for large cone angles it is necessary to consider non-linear damping effects. This has implications to the determination of the spin Hall angle, γ_{SH}. In a recent work of Mosendz [12] it was found that θ was as high as 15° while ΔH was found to be constant while varying θ_H. This may indicate an error in their analysis and since γ_{SH} depends on θ an inaccurate estimation of the cone angle could result in an incorrect γ_{SH}.

4.4 Arbitrary h Vector

Next we consider the most general case which is described by Eq. (57) where all components of **h** may contribute to the FMR line shape. The sample used here is a single Py strip where both the electric field which drives the current and the magnetic field which drives the magnetization precession are provided by a rectangular waveguide with a horn antennae. The sample chip is mounted at the end of a rectangular waveguide and the Py strip is directed along the short axis of the waveguide. In a waveguide, the electromagnetic fields are well known and in general three components, $h_{x'}, h_y$ and $h_{z'}$ exist. Fig. 22(a) shows both the FMR and perpendicular standing SWR at $\theta_H = 45°$. Indeed both the amplitude and the line shape are different for the two FMR peaks located at H and $-H$, which indicates the existence of multiple **h** field components due to the symmetry properties under $\theta_H \to \theta_H + 180°$ and Eq. (57) and Eq. (58) are needed to separate the various **h** components.

This separation is done using the Lorentz and dispersive amplitudes determined from a fit to the FMR which are plotted as a function of θ_H in Fig. 22(b) and (c) for $\omega/2\pi = 12$ and 11.2 GHz respectively. A fit using Eq. (58) for both the Lorentz and dispersive amplitudes allows a separation of the contributions from each of the $h_{x'}, h_y$ and $h_{z'}$ fields based on the their different contributions to the θ_H dependence of the line shape. The relative phase can simply be determined from the ratio of the Lorentz to dispersive amplitude of a given θ_H dependent term.

The results of the fit are shown in Table 1 where $\gamma/2\pi = 28.0$ μ_0GHz/T, $\mu_0 M_0$

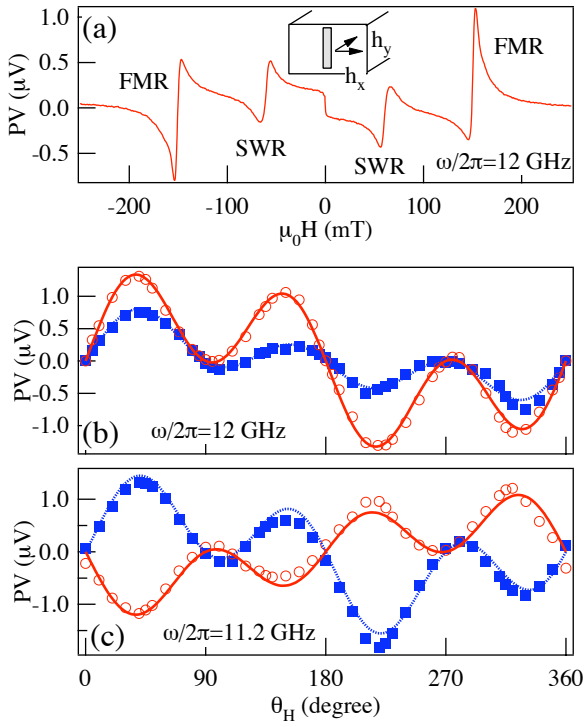

Figure 22: Data shown for a single Py strip with precession driven by horn antennae field. The strip dimensions are 3 mm × 50 μm × 45 nm. (a) Spectra showing distinct resonances due to FMR and perpendicular standing SWR at $\omega/2\pi = 12$ GHz. (b) Separated Lorentz and dispersive line shapes (circles/red and squares/blue respectively) as a function of θ_H from a fit to Eq. (57) at $\omega/2\pi = 12$ GHz and (c) $\omega/2\pi = 11.2$ GHz.

Table 1: Angular separation of **h** field components for 12 and 11.2 GHz.

	12 GHz	11.2 GHz
$\|h_{x'}\|$	1	1
$\|h_y\|$	0.02	0.14
$\|h_{z'}\|$	0.19	0.37
$\Phi_{x'}$	-23°	50°
Φ_y	40°	-30°
$\Phi_{z'}$	-33°	82°

= 0.97 T and $\mu_0 H_r$ = 152 mT were used. The amplitudes of the different **h** field components have been normalized with respect to the $h_{x'}$ component. At both 11.2 and 12 GHz the $h_{x'}$ field is much larger than h_y or $h_{z'}$ showing that the $h_{x'}$ field is primarily responsible for driving the magnetization precession which is expected

based on the wave propagation in a horn antennae.

In changing from 11.2 to 12 GHz the relative phase for each component is seen to change. Therefore even in the case of a complex line shape produced by multiple **h** field components, a θ_H measurement allows the individual contributions to be separated and the relative phase shifts are found to be non-zero.

4.5 A "Well Controlled" Sample

Finally we will discuss the issue of a well controlled sample. A set of first generation spin dynamos shown in the inset of Fig. 23(a) was fabricated with different Py thickness d. Two Py strips, denoted by S1 and S2, are deposited, one in each center of the G-S strips and the sample is kept symmetric with respect to the S strip. The lateral dimensions are identical for all samples which is warranted by the lithography and lift off techniques used. We will verify that even in such a sample which is "well controlled" during fabrication, the phase cannot be controlled.

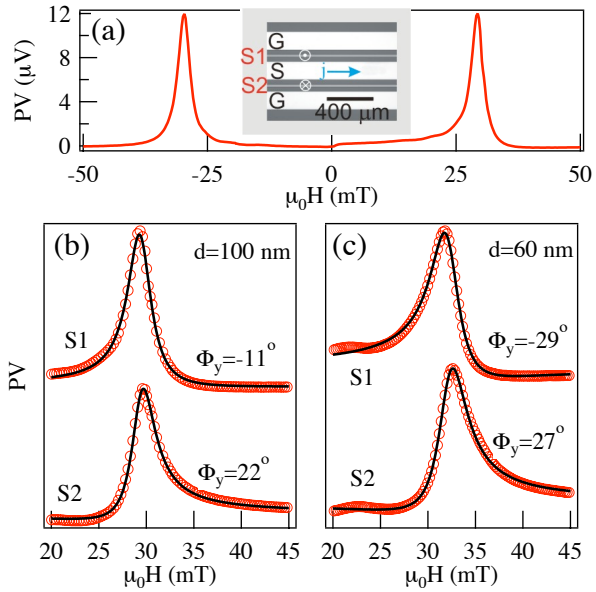

Figure 23: (a) FMR observed in a first generation spin dynamo. Inset shows the first generation spin dynamo structure with two Py strips labeled S1 and S2. (b) FMR for Py thickness $d = 100$ nm for both S1 and S2. In S1 $\Phi_y = -11°$, while in S2 the line shape is slightly more asymmetric and $\Phi_y = 22°$. (c) For $d = 60$ nm the relative phase is $\Phi_y = -29°$ for S1 and $\Phi_y = 27°$ for S2.

The current and rf magnetic field are induced in the Py via a current directly injected into the CPW. The sample geometry is analogous to the first sample already discussed and the dominant driving field will be in the y direction. The FMR shown

in Fig. 23(a) for the sample with $d = 100$ nm at $\omega/2\pi = 5$ GHz shows a symmetric Lorentz line shape and furthermore the FMR for $+H$ and $-H$ are identical. A careful fitting results in Φ_y = -11° being found. Interestingly the concurrent measurement for another Py strip in the same chip has a different $\Phi_y = 22°$. We can further compare the Φ_y for another sample with a different thickness, $d = 60$ nm. Here for S1, Φ_y = -29° and for S2, $\Phi_y = 27°$. Similar to the $d = 100$ nm sample, the relative phase is different for S1 and S2. Therefore it is not appropriate to consider a sample which is well controlled during fabrication to also have a well controlled relative phase.

5 Conclusions

The coupling between current and magnetization in a ferromagnetic microstrip provides a powerful tool for the study of spin dynamics by enabling the electrical detection of FMR. Due to the coherent nature of this coupling, the resulting dc voltage depends strongly on the relative phase between the rf electric and magnetic fields used to drive the current and magnetization respectively. Therefore not only does electrical FMR detection provide a route to study the relative phase, but it also necessitates calibrating the relative phase prior to performing electrically detected FMR experiments. Regardless of the FMR driving field, and even in the general case of multiple components driving FMR, the relative phase between the rf electric and magnetic field is observed to be sample and frequency dependent and non-zero. This non-zero phase results in both symmetric and antisymmetric Lorentz contributions to the FMR line shape, making Φ an important parameter when performing experiments based on characterizing the electrically detected FMR. The Φ dependence of the line shape symmetry also changes based on which component of the rf **h** field is responsible for driving the FMR precession meaning that the line shape itself cannot be used to determine Φ directly. For instance a purely antisymmetric line shape could correspond to $\Phi_{x'} = 0°$ if the FMR is driven by $h_{x'}$, or to $\Phi_y = 90°$ if the FMR is driven by h_y. Therefore to properly measure the relative phase, the **h** field components must be separated, making a θ_H measurement necessary. Using such a measurement Φ has been observed to change from 0° to 90° in a narrow frequency range (0.6 GHz) resulting in a change from an antisymmetric to symmetric line shape demonstrating the large effect the relative phase has on the FMR line shape. Furthermore such changes cannot be well controlled even in a sample which is well controlled during fabrication. Therefore in our opinion Φ cannot be predicted and should be calibrated for each sample, at each frequency and for each measurement cycle. A possible method for such a Φ calibration is the technique of spintronic Michelson interferometry, which could be used to accurately separate the dispersive and Lorentz line shapes in electrically detected FMR experiments in order to help resolve the γ_{SH} controversy.

Acknowledgements

I would like to thank Dr. Can-Ming Hu for the very productive and inspiring summer I was able to spend working in his lab, and for the opportunity to carry on that work through this thesis project, which was a great way to spend my final undergraduate year. Thank you to Dr. Yongsheng Gui for all his help in the lab and for his clear explanations of anything I had questions about. I was also fortunate enough to work with a great group of researchers in Dr. Hu's lab and would like to extend my appreciation to Zhongxing Chao, Dr. Xiao-Long Fan, Xiaofeng Zhu, and Dr. Andre Wirthmann.

Appendices

A Determining Φ in a Multilayer system

In this appendix we outline an approach to calculate the electric and magnetic fields in a multilayer structure. Once both fields are calculated the phase can be compared to determine the relative electromagnetic phase. Rather than performing such a calculation with a waveguide field with all the sample parameters we consider the case of a plane wave moving through the multilayer structure. There are some unanswered questions regarding this calculation which are presented here.

To determine the relative electromagnetic phase we must consider the propagation of electromagnetic waves in a dispersive medium, which introduces a phase shift through an imaginary wave vector. The most common example is a conductor. Such propagation can be characterized by three material parameters; the permittivity, ϵ, permeability, μ and conductivity, σ. Maxwell's equations admit a plane wave solution with the wave vector given by $\bar{k}^2 = \omega^2\mu\left(\epsilon + i\frac{\sigma}{\omega}\right)$. This has the same form as the wave vector for propagation in a non-conducting medium with $\epsilon \to \bar{\epsilon} = \epsilon + i\frac{\sigma}{\omega}$. This replacement can also be used to determine the complex index of refraction, $n = c\sqrt{\mu\bar{\epsilon}}$.

Consider a plane wave traveling in the z direction and polarized along the x axis which can travel through m layers of different thickness, as shown in Fig. 24.

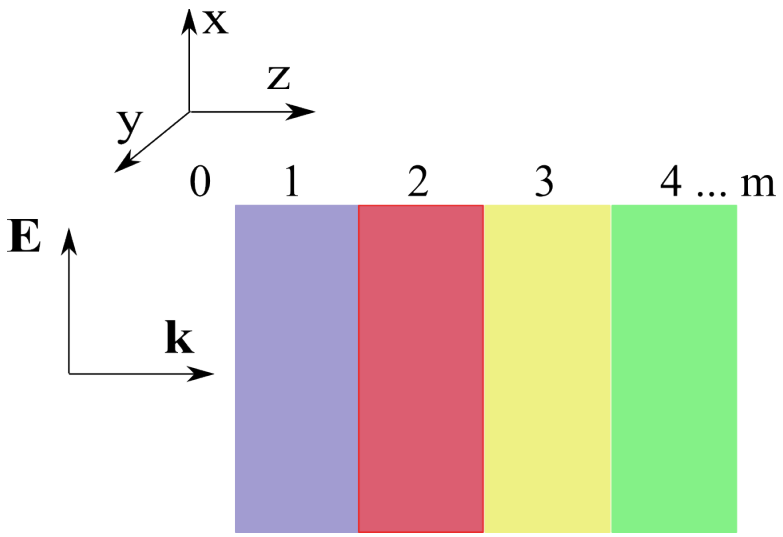

Figure 24: Plane wave propagating through multilayer structure.

As the wave propagates it will be reflected and transmitted at each interface so that in each layer there is a right (E_{mr}) and left (E_{ml}) moving component. According to the boundary conditions of Maxwell's equations, the field and its derivative should be continuous at each interface. In the mth layer the field and its derivative as a

function of position are

$$E_m(z) = E_{mr}e^{ik_m z} + E_{ml}e^{-ik_m z},$$
$$F_m(z) = \frac{dE_m(z)}{dz} = ik_m E_{mr}e^{ik_m z} - ik_m E_{ml}e^{-ik_m z}. \quad (72)$$

After traveling a distance d, we have $E_m(z+d) = E_{mr}e^{ik_m z}e^{ik_m d} + E_{ml}e^{-ik_m z}e^{-ik_m d}$ and $F_m(z+d) = ik_m E_{mr}e^{ik_m z}e^{ik_m d} - ik_m E_{ml}e^{-ik_m z}e^{-ik_m d}$. This allows us to define a transfer matrix for the mth layer which propagates waves a distance d through the mth layer,

$$\begin{pmatrix} E_m(z+d) \\ F_m(z+d) \end{pmatrix} = \begin{pmatrix} \cos(k_m d) & \frac{1}{k_m}\sin(k_m d) \\ -k_m \sin(k_m d) & \cos(k_m d) \end{pmatrix} \begin{pmatrix} E_m(z) \\ F_m(z) \end{pmatrix} = C_m \begin{pmatrix} E_m(z) \\ F_m(z) \end{pmatrix}. \quad (73)$$

If the wave travels through a distance z_m through m layers and we take the 0 of the z axis to be at the interface between the 0^{th} and the 1^{st} layers, we can then write the field at the boundary of the m^{th} layer as

$$\begin{pmatrix} E_m(z_m) \\ F_m(z_m) \end{pmatrix} = \prod_{i=1}^{m} C_i \begin{pmatrix} E_0(0) \\ F_0(0) \end{pmatrix} = \begin{pmatrix} M_{11} & M_{12} \\ M_{21} & M_{22} \end{pmatrix} \begin{pmatrix} E_0(0) \\ F_0(0) \end{pmatrix}. \quad (74)$$

The distance d_n used to calculate the transfer matrix C_n will now be the thickness of the nth layer. If we want to calculate the field at some point d into the last layer rather than at the boundary of the last layer, the m^{th} matrix C_m should use the distance d rather than thickness of the layer.

The field at a distance z_m can then be determined from the incoming field as

$$E_m(z_m) = M_{11}E_0(0) + M_{12}F_0(0),$$
$$F_m(z_m) = M_{21}E_0(0) + M_{22}F_0(0). \quad (75)$$

Since there is no left traveling wave in the m^{th} layer we have,

$$E_m(z_m) = E_{mr}e^{ik_m z_m},$$
$$F_m(z_m) = ik_m E_{mr}e^{ik_m z_m}. \quad (76)$$

Using Eq. 75 and Eq. 76, $F_0(0)$ can be written in terms of $E_0(0)$,

$$F_0(0) = \frac{(M_{21} - ik_m M_{11})E_0(0)}{ik_m M_{12} - M_{22}} = \beta E_0(0). \quad (77)$$

Since $F_0(0) = ik_0 E_{0r} - ik_0 E_{0l}$ and $E_0(0) = E_{0r} + E_{0l}$, the left traveling wave in the 0^{th} layer, E_{0l}, can be written in terms of the incoming wave, E_{0r} as,

$$E_{0l} = \frac{ik_0(ik_m M_{12} - M_{22}) - (M_{21} - ik_m M_{11})}{ik_0(ik_m M_{12} - M_{22}) + (M_{21} - ik_m M_{11})} E_{0r} = \eta E_{0r}. \tag{78}$$

Therefore if the incoming electric field, E_{0r} is specified, the total wave in the 0^{th} layer is, $E_0(0) = E_{0r}(1+\eta)$, and we can determine the electric field in the n^{th} layer (n < m),

$$E_n = N_{11}E_0(0) + N_{12}\beta E_0(0) = [E_{0r}(1+\eta)](N_{11} + \beta N_{12}). \tag{79}$$

where N_{ij} are the matrix elements of $\prod_{i=1}^{n} C_i$.

If the material and thickness parameters of each layer are specified, and a plane wave of known frequency is used, each transfer matrix can be calculated and Eq. 79 would yield a complex number for the electric field which could be turned into an amplitude and phase. The next step is then to calculate the magnetic field in a given layer, which is where various questions are raised.

Based on Faraday's law the plane waves solutions for $\mathbf{E}$ and $\mathbf{H}$ are related by $\mathbf{H}_m = \frac{k_m}{\mu_m \omega} \widehat{\mathbf{k}}_m \times \mathbf{E}_m$. If we have the electric field in the m^{th} layer this would mean that we should be able to calculate $\mathbf{H}_m$ using the wave vector $\mathbf{k}_m$. However this means that regardless of which layer we are in the phase difference will only depend on the phase of $\mathbf{k}_m$ in that layer. This means that the phase would be a local property and that the reflection and transmission of the layers does not play a role; no matter how $\mathbf{E}_m$ would be calculated, the phase shift would be the same as long as $\mathbf{k}_m$ was the same. Also when the wave would go from a non-conducting to conducting layer, the phase would jump to 45°, and then go back to 0° when the wave goes back into a non-conductor. Of course one test of such a calculation would be to look at the limiting case of a perfect conductor where the phase shift should be 45°, and if we use this scheme to compute the phase shift in something like copper, the phase does come out to be 45°, but this is not a true test of the calculation, since we would obtain this result independent of the other layers.

If instead we would calculate the incoming magnetic wave using $\mathbf{H}_m = \frac{k_m}{\mu_m \omega} \widehat{\mathbf{k}}_m \times \mathbf{E}_m$ based on a specified incoming electric wave, we could then propagate the magnetic wave through in the same way as the electric wave. However this calculation would be exactly the same as the electric field calculation, and the only phase shift would be due to the wave vector in the first medium. Clearly this would not be correct since the phase shift in an infinite conducting sheet would then come out to be zero if the wave entered from air.

Neither of the above two methods seems reliable and a new way of calculating the magnetic field is necessary. The purpose of this calculation was to show in a simple case that the relative phase was non-zero, since many people believe it will be inherently zero and as a result, the FMR line shape will only have a dispersive or Lorentz line shape, but not both. Of course such a simple calculation cannot be applied directly to a real setup where the waves will no longer be planar, the boundary conditions become much more complex and the spatial distribution of fields

is more complicated. Nevertheless it would be useful to show that in a thin multilayer struction $\Phi \neq 0$. Even if the phase would turn out to be only locally dependent on the sample as the result from Faraday's law would suggest, this would still prove the point that the relative phase is non-zero in the multilayer structure, but further work is needed to verify this.

References

[1] N. Mo, C.E. Patton, *Local ferromagnetic resonance measurement techniques*, Rev. Sci. Instrum. **79**, 040901 (2008).

[2] J. H. E. Griffiths, *Anomolous high-frequency resistance of ferromagnetic metals*, Nature. **158**, 670 (1946).

[3] C. Kittel, *Interpretation of anomalous Larmor frequencies in ferromagnetic resonance experiments*, Phys. Rev. **71**, 270 (1947).

[4] C. Kittel, *On the theory of ferromagnetic resonance absorption*, Phys. Rev. **73**, 155 (1948).

[5] Y.S. Gui, N. Mecking, X. Zhou, Gwyn Williams, C.-M. Hu, *Realization of a room-temperature spin dynamo: the spin rectification effect*, Phys. Rev. Lett. **98**, 107602 (2007).

[6] A. Wirthmann, Xiaolong Fan, Y.S. Gui, K. Martens, G. Williams, J. Dietrich, G.E. Bridges, C.-M. Hu, *Direct phase probing and mapping via spintronic Michelson interferometry*, Phys. Rev. Lett. **105**, 017202 (2010).

[7] M.I. D'yakonov, V.I. Perel, *Possibility of orienting electron spins with current*, Sov. Phys. JETP Lett. **13**, 467 (1971).

[8] M.I. D'yakonov, V.I. Perel, *Current-induced spin orientation of electrons in semiconductors*, Phys. Lett. A **35**, 459 (1971).

[9] J. E. Hirsch, *Spin Hall effect*, Phys. Rev. Lett. **83**, 1834 (1999).

[10] Y. Kato, R.C. Myers, A.C. Gossard, D.D. Awshalom *Observation of the spin Hall effect in semiconductors*, Science. **306**, 1910 (2004).

[11] J. Wunderlich, B. Kaestner, J. Sinova, T. Jungwirth, *Experimental observation of the spin Hall effect in a two-dimensional spin-orbit coupled semiconductor system*, Phys. Rev. Lett. **94**, 047204 (2005).

[12] O. Mosendz, J.E. Pearson, F.Y. Fradin, G.E.W. Bauer, S.D. Bader, A. Hoffmann, *Quantifying spin Hall angles from spin pumping: experiments and theory*, Phys. Rev. Lett. **104**, 046601 (2010).

[13] J. Inoue, H. Ohno, *Taking the Hall effect for a spin*, Science. **309**, 2004 (2005).

[14] Y. Tserkovnyak, A. Brataas, G.E.W. Bauer, *Spin pumping and magnetization dynamics in metallic multilayers*, Phys. Rev. B. **66**, 224403 (2002).

[15] Y. Tserkovnyak, A. Brataas, G.E.W. Bauer, *Enhanced Gilbert damping in thin ferromagnetic films*, Phys. Rev. B. **88**, 117601 (2002).

[16] X. Wang, G.E.W. Bauer, B.J. van Wees, A. Brataas, Y. Tserkovnyak, *Voltage generation by ferromagnetic resonance at a nonmagnet to ferromagnet contact*, Phys. Rev. Lett. **97**, 216602 (2006).

[17] A. Brataas, Y. Tserkovnyak, G.E.W. Bauer, B.I. Haperin, *Spin battery operated by ferromagnetic resonance*, Phys. Rev. B. **66**, 060404(R) (2002).

[18] L. Berger, *Generation of dc voltages by a magnetic multilayer undergoing ferromagnetic resonance*, Phys. Rev. B. **59**, 11465 (1999).

[19] T. Seki, Y. Hasegawa, S. Mitani, S. Takahashi, H. Imamura, S. Maekawa, J. Nitta, K. Takanashi, *Giant spin Hall effect in perpendicularly spin-polarized FePt/Au devices*, Nature Mater. **7**, 175 (2008).

[20] G. Mihajlovic, J.E. Pearson, M.A. Garcia, S.D. Bader, A. Hoffmann, *Negative nonlocal resistance in mesoscopic gold Hall bars: absence of the giant spin Hall effect*, Phys. Rev. Lett. **103**, 166601 (2009).

[21] K. Ando, S. Takahashi, K. Harii, K. Sasage, J. Ieda, S. Maekawa, E. Saitoh, *Electric manipulation of spin relaxation using the spin Hall effect*, Phys. Rev. Lett. **101**, 036601 (2008).

[22] T. Kimura, Y. Otani, T. Sato, S. Takahashi, S. Maekawa, *Room-temperature reversible spin Hall effect*, Phys. Rev. Lett. **98**, 156601 (2007).

[23] L. Liu, T. Moriyama, D. C. Ralph, R. A. Buhrman, *Spin-torque ferromagnetic resonance induced by the spin Hall effect*, Phys. Rev. Lett. **106**, 036601 (2011).

[24] S. Zhang, *spin Hall effect in the presence of spin diffusion*, Phys. Rev. Lett. **85**, 393 (2000).

[25] J. D. Jackson, *Classical Electrodynamics*, (Wiley, New York, 1998), 3^{th} ed.

[26] D. J. Griffiths. *Introduction to Electrodynamics*, (Prentice Hall, New Jersy, 1999), 3^{th} ed.

[27] C. Kittel, *Introduction to Solid State Physics*, (John Wiley & Sons, Inc., New York, 2004), 8^{th} ed.

[28] N. Mecking, A comprehensive study of the AMR-induced microwave photovoltage, photocurrent and photoresistance in permalloy microstrips, Ph.D. thesis, University of Hamburg.

[29] B. Lax, K.J. Button, *Microwave Ferrites and Ferrimagnetics*, (McGraw Hill, New York, 1962).

[30] R.W. Damon, *Ferromagnetic Resonance at High Power* in *Magnetism, a treatise on modern theory and materials*, (Academic Press, 1963).

[31] N. Mecking, Y.S. Gui, C.-M. Hu, *Microwave photovoltage and photoresistance effects in ferromagnetic microstrips*, Phys. Rev. B. **76**, 224430 (2007).

[32] Z. Zhi-Dong, *Spin waves in thin films, superlattices and multilayers* in *Handbook of think film materials: Nanomaterials and magnetic thin films, Volume 5*, (Academic Press, 2002).

[33] X. F. Zhu, M. Harder, A. Wirthmann, B. Zhang, W. Lu, Y. S. Gui, C.-M. Hu, *Dielectric measurements via a phase-resolved spintronic technique* Phys. Rev. B. **83**, 104407 (2011).

[34] X. F. Zhu, M. Harder, J. Tayler, A. Wirthmann, Bo Zhang, W. Lu, Y. S. Gui, C.-M. Hu, *Nonresonant spin rectification in the absence of an external applied magnetic field*, **83**, 140402 (2011).

[35] H.J. Juretschke, *Electromagnetic theory of dc effects in ferromagnetic resonance*, J. Appl. Phys. **31**, 1401 (1960).

[36] A.A. Michelson, E.W. Morley *On the relative motion of the earth and the luminiferous ether*, Am. J. Sci. **34**, 333 (1887).

[37] O.S. Heavens, *Optical Properties of Thin Solid Films*, (Dover, New York, 1965).

[38] M. Born, E. Wolf *Principles of optics: electromagnetic theory of propagation, interference and diffraction of light*, (Oxford, New York, 1975).

Google

Scholar

Michael Harder

Analysis of the line shape of electrically detected ferromagnetic resonance

Authors	M Harder, ZX Cao, YS Gui, XL Fan, C-M Hu
Publication date	2011/8/8
Journal	Physical Review B
Volume	84
Issue	5
Pages	054423
Publisher	American Physical Society
Description	Abstract This work reviews and examines two particular issues related with the new technique of electrical detection of ferromagnetic resonance (FMR). This powerful technique has been broadly applied for studying magnetization and spin dynamics over the past ten years. The first issue is the relation and distinction between different mechanisms that give rise to a photovoltage via FMR in spintronic devices, and the second is the proper analysis of the FMR line shape, which has become the “Achilles heel” in interpreting experimental ...
Total citations	Cited by 107

Scholar articles

Analysis of the line shape of electrically detected ferromagnetic resonance
M Harder, ZX Cao, YS Gui, XL Fan, CM Hu - Physical Review B, 2011
Cited by 107 - Related articles - All 7 versions

PHYSICAL REVIEW B **84**, 054423 (2011)

Analysis of the line shape of electrically detected ferromagnetic resonance

M. Harder,[1] Z. X. Cao,[1,2] Y. S. Gui,[1] X. L. Fan,[1,3] and C.-M. Hu[1,*]

[1]*Department of Physics and Astronomy, University of Manitoba, Winnipeg, Canada R3T 2N2*

[2]*National Lab for Infrared Physics, Shanghai Institute of Technical Physics, Chinese Academy of Science, Shanghai 200083, People's Republic of China*

[3]*The Key Lab for Magnetism and Magnetic Materials of Ministry of Education, Lanzhou University, Lanzhou 730000, People's Republic of China*

(Received 9 May 2011; revised manuscript received 30 June 2011; published 8 August 2011)

This work reviews and examines two particular issues related with the new technique of electrical detection of ferromagnetic resonance (FMR). This powerful technique has been broadly applied for studying magnetization and spin dynamics over the past ten years. The first issue is the relation and distinction between different mechanisms that give rise to a photovoltage via FMR in spintronic devices, and the second is the proper analysis of the FMR line shape, which has become the "Achilles heel" in interpreting experimental results, especially for either studying the spin pumping effect or quantifying spin Hall angles via the electrically detected FMR.

DOI: 10.1103/PhysRevB.84.054423 PACS number(s): 85.75.−d, 75.40.Gb, 76.50.+g, 42.65.−k

I. INTRODUCTION

Electrical detection of ferromagnetic resonance (FMR) in ferromagnets (FM) is a powerful new experimental tool which has transformed the research on spin and magnetization dynamics.[1–32] Over the past ten years, this technique has generated a great deal of interest in the communities of magnetism, spintronics, and microwave technologies. It has been broadly applied for studying diverse material structures, ranging from ferromagnetic thin films such as Py (permalloy, $Ni_{80}Fe_{20}$),[3,6,11,13], CrO_2,[14] Fe_3O_4,[14] single crystal Fe,[16] GaMnAs,[17] and $La_{1-x}Sr_xMnO_3$,[18] bilayer devices such as Py/Pt,[7,8,19,20,24,25] Py/Au,[19,20] Py/GaAs,[21] and $Y_3Fe_5O_{12}$/Pt,[22,23] to a variety of magnetic tunneling junctions (MTJ) based on magnetic multilayers.[4,9,10,15] From a technical standpoint, its high sensitivity has made it possible to quantitatively determine spin boundary conditions[26] and to directly measure nonlinear magnetization damping,[27–29] the quasiparticle mass for the domain wall,[30] the phase diagram of the spin-transfer driven dynamics[2] and various kinds of parametric spin wave excitations.[2,31,32] Its capability to probe the interplay of spins, charges, and photons has been utilized for studying spin rectification,[11,12] spin pumping,[7] spin torque,[15] and spin Hall effects,[19,24,25] which have led to the proposing and realization of novel dynamic spintronic devices such as the spin battery,[7,33–36] spin diode,[4,10,15] spin dynamo,[11,12] and spin demodulator.[37] Very recently, its ability to detect coherent processes[38–40] has enabled electrical probing of the spin-resonance phase and the relative phase of electromagnetic waves,[38] which pave new ways for microwave sensing,[41] nondestructive imaging,[38] and dielectric spectroscopy.[39] Such a coherent capability is especially exciting as it resembles the latest achievement in semiconductor spintronics, where a new platform for coherent optical control of spin/charge currents has been developed by using nonresonant quantum interferences.[42–44]

From the physical standpoint, many different effects may generate a time-independent dc voltage in magnetic materials via the FMR. Reported mechanisms involve spin rectification,[11,12] spin pumping,[7] spin torque,[15] spin diode,[4,10,15] spin Hall,[24] and inverse spin Hall effects.[8,19,20,25] Two major issues stand out here. (1) A unified picture clarifying the relations and distinctions between such diverse mechanisms has not been established, which leads to increasing controversy and confusion in interpreting and understanding experimental results. A stunning example of this issue is found in the very recent studies of the spin Hall effect via electrically detected FMR, where two similar experiments[19,24] performed on similar devices were interpreted completely differently.[45] (2) When more than one mechanism simultaneously plays a role in the FMR generated dc voltage, proper interpretation requires a quantitative analysis of the FMR line shape. In our opinion, such a seemingly trivial issue has become the "Achilles heel" of this powerful experimental technique, especially in recent studies of spin pumping and the spin Hall effect via electrically detected FMR. The purpose of this article is to address these two critical issues with a brief review of the key physics of this subject, followed by systematically measured experimental data with detailed theoretical analysis.

This paper is split into three main sections. First we provide a brief review of different mechanisms which may generate the photovoltage via the FMR. Then we use the dynamic susceptibility obtained from a solution of the Landau-Lifshitz-Gilbert equation to derive analytical formulas for analyzing the line shape and the symmetry properties of the photovoltage generated through spin rectification. Finally we present experimental results measured from different samples, at different frequencies, and in different experimental configurations, showing that the FMR line shape is determined by the relative phase of microwaves which is sample and frequency dependent.

II. A BRIEF REVIEW OF ELECTRICAL DETECTION OF FMR

Under microwave excitation at angular frequency ω, the rf electric ($\mathbf{e}$) and magnetic ($\mathbf{h}$) fields inside a ferromagnetic material can be described as $\mathbf{e} = \mathbf{e}_0 e^{-i\omega t}$ and $\mathbf{h} = \mathbf{h}_0 e^{-i(\omega t - \Phi)}$, respectively. Note that in general, due to the inevitable losses of microwaves propagating inside the ferromagnetic material,

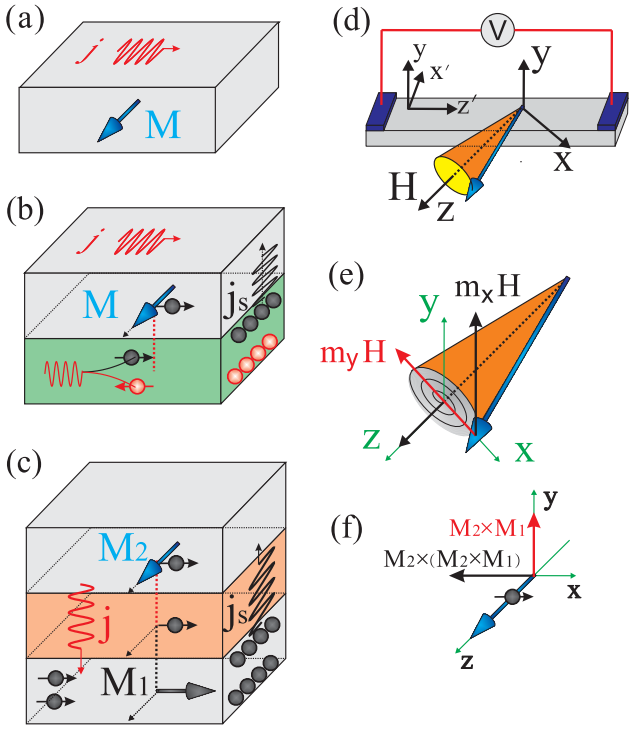

FIG. 1. (Color online) Dynamic response of magnetic structures under microwave irradiation: (a) Single thin film layer where the spin rectification is due to the magnetic field torque as shown in (e). (b) Magnetic bilayer device which has two rf currents $\mathbf{j}$ and $\mathbf{j}_s$ with different spin polarizations. Therefore spin rectification is due to both magnetic field and spin torques. (c) Magnetic tunneling junction with both $\mathbf{j}$ and $\mathbf{j}_s$. (d) Coordinate system for single ferromagnetic microstrips measured in this work under an in-plane applied static magnetic field $\mathbf{H}$. The z' axis is fixed along the strip and the direction of current flow, while the z axis is rotated to follow the direction of $\mathbf{H}$. (e) Components of magnetic field torque. (f) Spin torque in magnetic tunneling junction.

there is a phase difference Φ between the dynamic $\mathbf{e}$ and $\mathbf{h}$ fields. Such a relative phase is determined by the frequency-dependent wave impedance of the materials.[46] As shown in Fig. 1, the rf $\mathbf{e}$ field drives a rf current $\mathbf{j} = \sigma\mathbf{e}$, while the rf $\mathbf{h}$ field exerts a field torque on the magnetization and drives it to precess around its equilibrium direction [Fig. 1(e)]. Such a magnetization precession is described by the nonequilibrium magnetization $\mathbf{m} = \hat{\chi}\mathbf{h}$. Here σ and $\hat{\chi}$ are the high-frequency conductivity and Polder tensor, respectively. Note that due to the resonance nature of the precession, $\mathbf{m}$ lags $\mathbf{h}$ by a spin resonance phase Θ. However, despite the phase of Φ and Θ, the dynamic $\mathbf{j}$ and $\mathbf{m}$ keep the coherence of their respective driving fields, so that the product of any combination of their components may generate a time-independent signal proportional to $\langle \mathrm{Re}(\tilde{j}) \cdot \mathrm{Re}(\tilde{m}) \rangle$, where $\langle\ \rangle$ denotes the time average. The amplitude of such a signal depends on the phase difference of $\mathbf{j}$ and $\mathbf{m}$, which can be easily understood from the trigonometric relation $\langle \cos(\omega t) \cdot \cos(\omega t - \Phi) \rangle = \cos(\Phi)/2$. This is the spin rectification[11] as we highlight in Table I. For transport measurements on magnetic structures under microwave irradiation, various magnetoresistance effects such as anisotropic magnetoresistance (AMR), giant magnetoresistance (GMR), and tunneling magnetoresistance (TMR) make nonlinear corrections to Ohm's law via their corresponding magnetoresistance terms,[12] which typically lead to the product of $\mathbf{j}$ and $\mathbf{m}$. Such h-field torque induced spin rectifications are listed in Table I by the terms labeled V_{SR}^{h}. The earliest report on the measurement of V_{SR}^{h} dates to Juretschke's pioneering paper[47] published in 1960, although the power sensitivity achieved at that time was too small to be practically used (it was about 3 orders of magnitude smaller than that found in Ref. 11). The general feature of V_{SR}^{h} is that its amplitude depends on both the relative phase Φ and the spin resonance phase Θ, which leads to a characteristic phase signature of the FMR line shape.[38,39]

Similar to the effect of the rf $\mathbf{h}$ field torque, a spin torque induced by a spin polarized current may also drive magnetization precession. For example, in a bilayer [Fig. 1(b)] made of a ferromagnetic layer and a nonmagnetic layer with spin-orbit coupling,[24] in addition to the rf current $\mathbf{j}$ flowing in the ferromagnetic layer, the rf $\mathbf{e}$ field also induces a rf charge current flowing in the nonmagnetic layer. Via the spin Hall effect in such a nonmagnetic layer with spin-orbit coupling, the rf charge current can be converted into a spin current $\mathbf{j}_s$, which may flow into the ferromagnetic layer and then drive the magnetization precession via the spin torque. Such a spin torque induced nonequilibrium magnetization can be described by $\mathbf{m} = \hat{\chi}_j \mathbf{j}_s$, where the spin-torque susceptibility tensor $\hat{\chi}_j$ introduces a spin resonance phase ϑ that is different from Θ in $\hat{\chi}$. Following a similar consideration for the h-field induced spin rectification, a photovoltage depending on the spin torque may be generated in the ferromagnetic layer. This is the physical origin of the spin torque induced spin rectification effect,[24] which is listed in Table I by the term labeled V_{SR}^{s}. In MTJ [Fig. 1(c)], the spin polarized current $\mathbf{j}_s$ can be directly generated in the ferromagnetic layer where the magnetization is pinned along a different direction than that of the free layer. It tunnels into the free layer and drives the magnetization precession via the spin torque [Fig. 1(f)]. The spin torque induced spin rectification signal in MTJ has been measured in spin diodes,[4,10,15] which is also listed in Table I by the term labeled V_{SR}^{s}.

Over the past few years, systematic studies on spin rectifications induced by the h-field torque (V_{SR}^{h}) and spin torque (V_{SR}^{s}) have been performed, respectively, at the University of Manitoba[11,12,16,17,26–28,38,39,41] and Cornell University.[2,9,15,24,50] It has been found that due to the coherent nature of spin rectification, both V_{SR}^{h} and V_{SR}^{s} depend on the phase difference between $\mathbf{j}$ and $\mathbf{m}$. However, only the field torque spin rectification (V_{SR}^{h}) can be controlled by the relative phase Φ of the microwaves.[38]

In addition to such coherent spin rectification effects, it is known that at the interface between a ferromagnetic and a nonmagnetic layer, microwave excitation may generate a spin polarized current flowing across the interface via the spin pumping effect.[33] This effect has been observed in a few striking experiments by measuring either transmission electron spin resonance[48] or enhanced magnetization damping.[49] It involves FMR, exchange coupling, and nonequilibrium spin diffusion. An intuitive physical picture of spin pumping was given by the classical paper of Silsbee *et al.*[48] published in 1979, which used a phenomenological model to highlight the key mechanism of dynamic exchange coupling between

the precessing magnetization and the spin polarized current. Such a dynamic coupling significantly "amplifies" the effect of the rf **h** field in generating nonequilibrium spins, which diffuse across the ferromagnetic (FM) /normal metal (NM) interface to form the spin polarized current. Microscopically, spin pumping is a consequence of spin dependent reflectivity and transmission parameters of NM electrons at the FM/NM interface. Spin mixing conductance is the main parameter driving spin pumping, which was rigorously derived by Tserkovnyak *et al.*[33] Theoretical derivation is not trivial but the picture behind it is very clear and using magnetoelectronics Kirchhoff's laws[33] one can easily apply such a derivation to different dynamical configurations. It has been proposed that the spin current generated via spin pumping may also induce a photovoltage, either across the interface in a spin battery,[7,34–36] or within the nonmagnetic layer via the inverse spin Hall effect.[8,19,20,25] Recent experiments performed on magnetic bilayers[24] have suggested that spin-pumping induced dc voltage (the term V_{SP} in Table I) is about two orders of magnitude smaller than spin torque induced spin rectification (the term labeled V_{SR}^{s}). In contrast to phase sensitive coherent spin rectification effects, the proposed spin-pumping photovoltage is based on incoherent spin diffusion and FMR absorption. Hence, the anticipated FMR line shape of V_{SP} is symmetric and phase independent.

From the above discussion, it is clear that the line shape analysis plays the essential role in distinguishing the microwave photovoltage generated by different mechanisms. This issue has been partially addressed by a number of theoretical[50,51] and experimental works[4,10,15] studying nanostructured MTJs where the photovoltage is dominated by the spin torque induced spin rectification. Enlightened by these works and also based on our own previous studies,[12,38] we discuss in the following the critical issue of FMR line shape analysis in microstructured devices, where the field and spin torque induced spin rectification may have comparable strength. Our theoretical consideration and experimental data demonstrate the pivotal role of the relative phase Φ, which was often underestimated in previous studies. Via systematic studies with different device structures, measurement configurations and frequency ranges, we find that Φ has to be calibrated at different microwave frequencies for each device independently. Hence our results are in strong contradiction with the recent experiment performed on microstructured magnetic bilayers for quantifying the spin Hall angles, where Φ was set to zero for all devices at all microwave frequencies[19,20] based on the results of line shape analysis performed on reference samples.[52]

III. FMR LINE SHAPE

A. The characteristic signature

From Table I the role of the phase in the FMR line shape symmetry can be understood by considering the spin rectified voltage $V \propto \langle \mathrm{Re}(\tilde{j}) \cdot \mathrm{Re}(\tilde{m}) \rangle$. For spin rectification induced by the field torque, depending on the experimental configuration, at least one matrix component χ of the Polder tensor $\widehat{\chi}$ will drive the FMR; whether an on or off-diagonal component is responsible for the magnetization precession depends on the measurement configuration. Since $\mathbf{m} = \widehat{\chi}\mathbf{h}$, $\mathrm{Re}(\tilde{m}) \propto \mathrm{Re}(\chi)\cos(\omega t - \Phi) + \mathrm{Im}(\chi)\sin(\omega t - \Phi)$. Therefore after time averaging a time independent dc voltage is found $V(\Phi) \propto [\mathrm{Re}(\chi)\cos(\Phi) - \mathrm{Im}(\chi)\sin(\Phi)]$. It is well known that for diagonal matrix elements, $\mathrm{Re}(\chi)$ has a dispersive line shape while $\mathrm{Im}(\chi)$ has a symmetric line shape. However, since the on- and off-diagonal susceptibilities differ by a phase of 90°, if the FMR is driven by an off-diagonal susceptibility, the roles are reversed and $\mathrm{Re}(\chi)$ has a symmetric line shape while $\mathrm{Im}(\chi)$ has a dispersive line shape.

Based on the simple argument leading to the above $V(\Phi)$ expression, one can see that the line shape symmetry has a characteristic dependence on the relative phase Φ between electric and magnetic fields. Thus when measuring FMR based on the field torque induced spin rectification effect, it is important to consider the relative phase, whereas for a spin pumping measurement which measures $|\mathbf{m}|^2$, or for a spin torque induced spin rectification which involves $|\mathbf{j}|^2$, the relative phase does not influence the experiment. In the next two sections, a detailed analysis is given by solving the Landau-Lifshitz-Gilbert equation, which leads to analytical formulas describing the symmetric and dispersive line shapes for different measurement configurations.

B. The dynamic susceptibility

The Landau-Lifshitz-Gilbert equation provides a phenomenological description of ferromagnetic dynamics based

TABLE I. Relation and distinctions between different mechanisms for microwave photovoltages induced by FMR. (For simplicity we consider only one matrix element of $\hat{\chi}$ and $\hat{\chi}_j$ which is responsible for the spin rectification. $\tilde{j}$ and $\tilde{m}$ denote a corresponding component of the time-dependent current and magnetization, respectively.)

rf driving Effect	$\tilde{e} = e_0 e^{-i\omega t}$ Ohm's law	$\tilde{j} = j_0 e^{-i\omega t}$ Spin Hall	$\tilde{h} = h_0 e^{-i(\omega t - \Phi)}$ Field torque		$\tilde{j}_s = j_S e^{-i\omega t}$ Spin torque	Spin rectification[a,b]		Spin pumping[c]
dc voltage						$V \sim \langle Re(\tilde{j}) \cdot Re(\tilde{m}) \rangle$		$V \sim \lvert\tilde{h}\rvert^2$
Thin film	$\tilde{j} = \sigma\tilde{e}$		$\tilde{m} = \chi e^{i\Theta}\tilde{h}$			$V = V_{SR}^{h} \cdot (e_0 h_0)$		
Bilayer	$\tilde{j} = \sigma\tilde{e}$	$\tilde{j}_s$	$\tilde{m} = \chi e^{i\Theta}\tilde{h}$	+	$\chi_j e^{i\vartheta}\tilde{j}_s$	$V = V_{SR}^{h} \cdot (e_0 h_0) + V_{SR}^{s} \cdot (j_0 j_S)$	+	$V_{SP} \cdot h_0^2$
MTJ	$\tilde{j}, \tilde{j}_s$		$\tilde{m} = \chi e^{i\Theta}\tilde{h}$	+	$\chi_j e^{i\vartheta}\tilde{j}_s$	$V = V_{SR}^{h} \cdot (e_0 h_0) + V_{SR}^{s} \cdot (j_0 j_S)$		

[a] V_{SR}^{h}: Photovoltage caused by h-field torque induced *spin rectification* (including the so-called *AMR photovoltage*).[6,11–13,47]
[b] V_{SR}^{s}: Photovoltage caused by spin torque induced *spin rectification* (also known as the *spin diode effect*).[4,10,15,24]
[c] V_{SP}: Photovoltage caused by *spin pumping*.[7,8,19,20,25]

on a torque provided by the internal magnetic field $\mathbf{H}_i$ which acts on the magnetization $\mathbf{M}$, causing it to precess[53]

$$\frac{d\mathbf{M}}{dt} = -\gamma(\mathbf{M}\times\mathbf{H}_i) + \frac{\alpha}{M}\left(\mathbf{M}\times\frac{d\mathbf{M}}{dt}\right). \quad (1)$$

Here γ is the effective electron gyromagnetic ratio and α is the Gilbert damping parameter which can be used to determine the FMR linewidth ΔH in the linear regime, according to $\Delta H \sim \alpha\omega/\gamma$. For the case of microwave induced ferromagnetic resonance Eq. (1) can be solved by splitting the internal field into dc and rf components and taking the applied dc field $\mathbf{H}$ along the z axis. We can relate the internal field $\mathbf{H}_i = \mathbf{H}_{0i} + \mathbf{h}_i e^{-i\omega t}$ to the applied field through the demagnetization factors N_k, $H_{0iz} = H - N_z M_0$, $h_{ik} = h_k e^{i\Phi_k} - N_k m_k$, where Φ_k is the relative phase shift between the electric and magnetic fields in the kth direction and $\mathbf{M}_0$ is the dc magnetization also along the z axis. With the magnetization separated into dc and rf contributions $\mathbf{M} = \mathbf{M}_0 + \mathbf{m}e^{-i\omega t}$, the solution of Eq. (1) yields the dynamic susceptibility tensor $\widehat{\chi}$ which relates the magnetization $\mathbf{m}$ to the externally applied rf field $\mathbf{h}$,

$$\mathbf{m} = \widehat{\chi}\mathbf{h} = \begin{pmatrix} \chi_{xx} & i\chi_{xy} & 0 \\ -i\chi_{xy} & \chi_{yy} & 0 \\ 0 & 0 & 0 \end{pmatrix}\mathbf{h} = \begin{pmatrix} |\chi_{xx}| & |\chi_{xy}|e^{i\frac{\pi}{2}} & 0 \\ |\chi_{xy}|e^{-i\frac{\pi}{2}} & |\chi_{yy}| & 0 \\ 0 & 0 & 0 \end{pmatrix}\mathbf{h}e^{i\Theta}, \quad (2)$$

where $\Theta = \arctan[\Delta H/(H - H_r)]$ is the spin resonance phase[38] which describes the phase shift between the response and the driving force in terms of the linewidth ΔH and the resonance field H_r which are constant for a fixed frequency. Θ will change from 180° (driving force out of phase) to 0° (driving force in phase) around the resonance position, in a range on the order of ΔH, passing through 90° at resonance. This represents the universal feature of a resonance; the phase of the dynamic response always lags behind the driving force.[54]

To emphasize the resonant feature of the susceptibility tensor elements we define the symmetric Lorentz line shape L, and the dispersive line shape D as

$$L = \frac{\Delta H^2}{(H - H_r)^2 + \Delta H^2}, \qquad D = \frac{\Delta H(H - H_r)}{(H - H_r)^2 + \Delta H^2}. \quad (3)$$

Clearly the spin resonance phase can also be written in terms of L and D as $\Theta = \arctan[\Delta H/(H - H_r)] = \arctan(L/D)$ so that $L \propto \sin(\Theta)$ and $D \propto \cos(\Theta)$. Therefore L and D carry the resonant information of the susceptibility tensor.

Using L and D allows the elements of $\widehat{\chi}$ to be written as $(\chi_{xx}, \chi_{xy}, \chi_{yy}) = (D + iL)(A_{xx}, A_{xy}, A_{yy})$. A_{xx}, A_{xy} and A_{yy} are real amplitudes which are related to the sample properties

$$A_{xx} = \frac{\gamma M_0[M_0 N_y + (H - N_z M_0)]}{\alpha\omega[2(H - N_z M_0) + M_0(N_z + N_y)]}, \quad A_{xy} = -\frac{M_0}{\alpha[2(H - N_z M_0) + M_0(N_z + N_y)]}, \quad A_{yy} = \frac{\gamma M_0[M_0 N_x + (H - N_z M_0)]}{\alpha\omega[2(H - N_z M_0) + M_0(N_z + N_y)]}. \quad (4)$$

Since these amplitudes are real all components of $\widehat{\chi}$ include both a dispersive and a Lorentz line shape determined solely from the $D + iL$ term. However, in a transmission experiment performed using a resonance cavity $|m|^2 \propto L^2 + D^2 = L$ is measured. This product removes the phase dependence carried by L and D and leaves only the Lorentz line shape. For the same reason, the microwave photovoltage induced by spin pumping (the V_{SP} term in Table I) has a symmetric line shape.

The susceptibility for the two cases of in-plane and perpendicularly applied dc magnetic fields can easily be found from Eq. (4) by using the appropriate demagnetization factors. When the lateral dimensions are much larger than the thickness, $N_x = N_z = 0$ and $N_y = 1$ for an in-plane field and $N_x = N_y = 0$ and $N_z = 1$ for a field applied at a small angle from the perpendicular. In this paper we focus on the in-plane case. The line shape analysis for the perpendicular case can be found in Ref. 38. In both cases the form of the susceptibility $\chi \propto D + iL$ describes the ferromagnetic resonance line shape where each element of $\widehat{\chi}$ is the sum of an antisymmetric and symmetric Lorentz line shape. As we describe in the next section, via the V_{SR}^h term of the spin rectification effect, the symmetry properties of the dynamic susceptibility influence the symmetry of the electrically detected FMR which can be controlled by tuning the relative electromagnetic phase Φ.

C. Spin rectification induced by the field torque

The field-torque spin rectification effect results in the production of a dc voltage from the nonlinear coupling of rf electric and magnetic fields. For example, it may follow from the generalized Ohm's law[47,55]

$$\mathbf{J} = \sigma\mathbf{E}_0 - \frac{\sigma\Delta\rho}{\mathbf{M}^2}(\mathbf{J}\cdot\mathbf{M})\mathbf{M} + \sigma R_H \mathbf{J}\times\mathbf{M}, \quad (5)$$

where σ is the conductivity, $\Delta\rho$ is the resistivity change due to AMR, and R_H is the extraordinary Hall coefficient.

As shown in Fig. 2, we use two coordinate systems to describe a long narrow strip under the rotating in-plane magnetic field $\mathbf{H}$. The sample coordinate system $(\widehat{\mathbf{x}}', \widehat{\mathbf{y}}', \widehat{\mathbf{z}}')$ is fixed with the sample length along the z' direction and the sample width in the x' direction. The measurement coordinate system $(\widehat{\mathbf{x}}, \widehat{\mathbf{y}}, \widehat{\mathbf{z}})$ rotates with the $\mathbf{H}$ direction which is along the $\widehat{\mathbf{z}}$ axis. We define θ_H as the angle between the direction of the strip and the in-plane applied static magnetic field i.e., between the z' and z directions). In both coordinate systems, the $\widehat{\mathbf{y}}$ axis is along the normal of the sample plane. In the case of a sample length much larger than the width, the rf current $\tilde{j} = j_{z'}e^{-i\omega t}$ flows along the strip direction z'. In this geometry the field due to the Hall effect will only be in the transverse direction and will not generate a voltage along the strip. Taking the time average of the electric field integrated along the z' direction, the photovoltage is found as[11,12]

$$V = \frac{\Delta R}{M_0}\langle \mathrm{Re}(\tilde{j})\cdot\mathrm{Re}(\tilde{m}_x)\rangle \sin(2\theta_H), \quad (6)$$

where ΔR is the resistance change due to the AMR effect and the $\sin(2\theta_H)$ term is a result of the AMR effect which couples $\mathbf{J}$ and $\mathbf{M}$.

The susceptibility tensor given by Eqs. (2) and (4) can be used to write $\tilde{m}_x$ in terms of the rf $\mathbf{h}$ field. Since $\mathbf{M}_0$ and $\mathbf{H}$ are

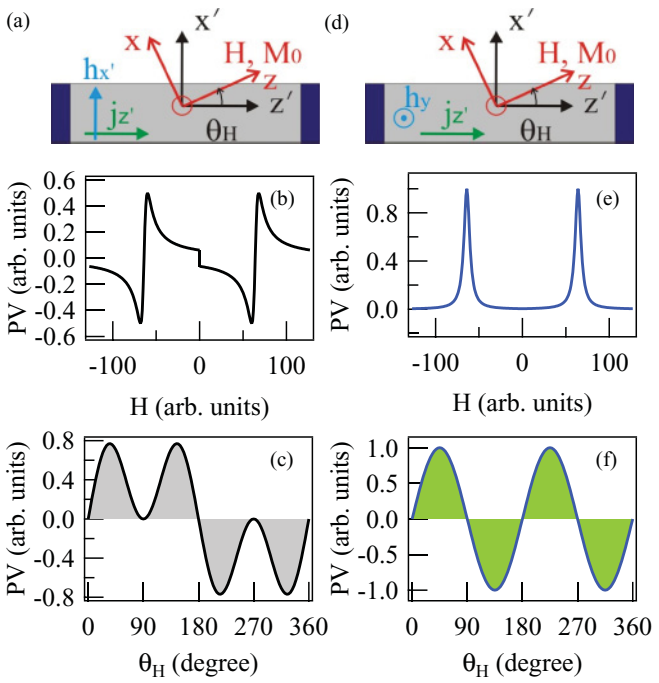

FIG. 2. (Color online) Left panel (a) Coordinate system for an in-plane dc H field applied along the z axis at an angle θ_H with respect to the z' axis, with a rf h field along the x' axis. (b) The calculated photovoltage (PV) spectrum at $\theta_H = 45^\circ$ and (c) the calculated amplitude of the PV spectrum at FMR as a function of θ_H according to Eq. (9). Right panel (d)–(f) are the same as (a)–(c), respectively, but with a rf h field along the y axis, and calculations are according to Eq. (10). In both cases, Φ is assumed to be zero for simplicity.

both along the z axis, only the components of **h** perpendicular to **z** will contribute to **m**. However, since the rf current flows in the z' direction, to calculate the rectified voltage, $\tilde{m}_x$ must be transformed into the (x', y, z') coordinate system by using the rotation $(\hat{\mathbf{x}}, \hat{\mathbf{y}}, \hat{\mathbf{z}}) = [\cos(\theta_H)\hat{\mathbf{x}}' - \sin(\theta_H)\hat{\mathbf{z}}', \hat{\mathbf{y}}, \sin(\theta_H)\hat{\mathbf{x}}' + \cos(\theta_H)\hat{\mathbf{z}}']$, which introduces an additional θ_H dependence into the photovoltage. We find that the photovoltage can be written in terms of the symmetric and antisymmetric Lorentz line shapes L and D as

$$V = \frac{\Delta R}{2M_0} j_{z'}(A_L L + A_D D), \tag{7}$$

where

$$\begin{aligned} A_L &= \sin(2\theta_H)[-A_{xx}h_{x'}\cos(\theta_H)\sin(\Phi_{x'}) \\ &\quad - A_{xy}h_y\cos(\Phi_y) + A_{xx}h_{z'}\sin(\theta_H)\sin(\Phi_{z'})], \\ A_D &= \sin(2\theta_H)[A_{xx}h_{x'}\cos(\theta_H)\cos(\Phi_{x'}) \\ &\quad - A_{xy}h_y\sin(\Phi_y) - A_{xx}h_{z'}\sin(\theta_H)\cos(\Phi_{z'})], \end{aligned} \tag{8}$$

and $\Phi_{x'}, \Phi_y$, and $\Phi_{z'}$ are the relative phases between electric and magnetic fields in the x', y, and z' directions, respectively.

The amplitudes of the Lorentz and dispersive line shape contributions show a complex dependence on the relative phases for the x', y, and z' directions and in general both line shapes will be present. However, depending on the experimental conditions, this dependence may be simplified. For instance, when $h_{x'}$ is the dominate driving field as shown in Fig. 2(a), we may take $h_y = h_{z'} \approx 0$ and $\Phi_{x'} = \Phi$, which results in

$$\begin{aligned} V = &-\frac{\Delta R}{2M_0} j_{z'} A_{xx} h_{x'} \cos(\theta_H)\sin(2\theta_H) \\ &\times [L\sin(\Phi) - D\cos(\Phi)]. \end{aligned} \tag{9}$$

From Eq. (9) we see that the photovoltage line shape changes from purely symmetric to purely antisymmetric in 90° intervals of Φ, being purely antisymmetric when $\Phi = n \times 180^\circ$ and purely symmetric when $\Phi = (2n+1) \times 90^\circ, n = 0, \pm 1, \pm 2 \ldots$.

As shown in Figs. 2(b) and 2(c), the photovoltage in Eq. (9) also shows symmetries depending on the static field direction θ_H. Since $\mathbf{H} \to -\mathbf{H}$ corresponds to $\theta_H \to \theta_H + 180^\circ$, $V(H) = -V(-H)$. Furthermore, at $\theta_H = n \times 90^\circ, n = 0, \pm 1, \pm 2, \ldots$ the voltage will be zero.

Similarly when h_y dominates as shown in Fig. 2(d), we take $h_{x'} = h_{z'} \approx 0$ and $\Phi_y = \Phi$ which results in a voltage

$$\begin{aligned} V = &-\frac{\Delta R}{2M_0} j_{z'} A_{xy} h_y \sin(2\theta_H) \\ &\times [L\cos(\Phi) + D\sin(\Phi)]. \end{aligned} \tag{10}$$

The symmetry properties are now such that the line shape is purely symmetric when $\Phi = n \times 180^\circ$ and purely antisymmetric when $\Phi = (2n+1) \times 90^\circ, n = 0, \pm 1, \pm 2 \ldots$. Also the photovoltage determined by Eq. (10) is now symmetric with respect to H under $\theta_H \to \theta_H + 180^\circ$ so that $V(H) = V(-H)$ as shown in Fig. 2(e). Therefore, experimentally the different symmetry of the FMR at H and $-H$ can be used as an indication of which component of the **h** field is dominant.

Both Eqs. (9) and (10) demonstrate that a change in the relative electromagnetic phase is expected to result in a change in the line shape of the electrically detected FMR. It is worth noting that when the relative phase $\Phi = 0$, the line shape is purely antisymmetric for FMR driven by $h_{x'}$ and purely symmetric for FMR driven by h_y as illustrated in Figs. 2(b) and 2(e), respectively. In the general case when $\tilde{m}_x$ is driven by multiple **h** components, Eq. (7) must be used in combination with angular (θ_H) dependent measurements in order to distinguish different contributions.

We also note that the above theoretical line shape analysis in the in-plane magnetic field case is consistent with our previous line shape study[38] in the perpendicular field case. In Ref. 38 we have established spintronic Michelson interferometry which enabled the demonstration of external control of the relative phase Φ. By applying such a novel technique, the measured response of the photovoltage line shape[38,39] was found to change its symmetry and polarity in 90° and 180° cycles of Φ, respectively, in excellent agreement with our line shape theory.

D. The physics of Φ

It is clear therefore that for field torque induced spin rectification, the relative phase Φ between the microwave electric and magnetic fields plays the pivotal role in the FMR line shape. Note that Φ is a material and frequency dependent property which is related to the losses in the system.[46,57,58] When a plane electromagnetic wave propagates through free space the electric and magnetic fields are in phase and orthogonal to each other.[56] However when the same electromagnetic

wave travels through a dispersive medium where the wave vector is complex, the imaginary contribution can create a phase shift between electric and magnetic fields. The most well known example is that of a plane electromagnetic wave moving in a conductor[46] where Faraday's law gives a simple relation between electric and magnetic fields $\omega\mu\mathbf{h} = \mathbf{k} \times \mathbf{e}$. Therefore the complex part of the wave vector $\mathbf{k}$ will induce a phase shift between electric and magnetic fields. Although the field will exponentially decay inside a conductor, it will still penetrate a distance on the order of the skin depth, and in a perfect conductor the conductivity, which produces an imaginary dielectric constant, will result in a phase shift of 45° between the electric and magnetic fields.[46]

In a complex system such as an experimental set up involving waveguides, coaxial cables, bonding wires, and a sample holder, which are required for electrical FMR detection, one cannot simply argue that Faraday's law itself is sufficient to explain the phase difference between the magnetic and electric field components. One needs to solve Maxwell's equations in their entirety by including full electromagnetic wave propagation with the relevant boundary conditions. The presence of electrical leads for measurement of dc voltage makes this problem very difficult. Nevertheless losses in the system which can be characterized in a variety of ways, such as through the wave impedance,[57,58] will lead to a phase shift between electric and magnetic fields which will influence the FMR line shape.

Although the physics of Φ is in principle contained in Maxwell's equations, due to the lack of technical tools for simultaneously and coherently probing both $\mathbf{e}$ and $\mathbf{h}$ fields, the effect of the relative phase had often been ignored until the recent development of spintronic Michelson interferometry.[38] In the following we provide systematically measured data showing the influence of the relative phase Φ on the line shape of FMR which is driven by different $\mathbf{h}$ field components.

IV. EXPERIMENTAL LINE SHAPE MEASUREMENTS

A. h_y dominant FMR

In order to use the h_y field to drive FMR a first generation spin dynamo was used where a Cu/Cr coplanar waveguide (CPW) was fabricated beside a Py microstrip with dimension 300 μm × 20 μm × 50 nm on a SiO_2/Si substrate as shown in Fig. 3(a). A microwave current is directly injected into the CPW and flows in the z' direction inducing a current in the Py strip also along the z' axis. In this geometry the dominant rf $\mathbf{h}$ field in the Py will be the Oersted field in the y direction produced according to Ampère's law. This field will induce FMR precession with the same cone angle independent of the in-plane orientation of the static field $\mathbf{H}$.

The AMR resistance depends on the orientation of the magnetization relative to the current and follows the relation $R(H) = R(0) - \Delta R \sin^2(\theta_M)$, where θ_M (not shown) is the angle between the magnetization and the current direction. For Py the AMR effect, which is responsible for the spin rectification, is observed to produce a resistance change of $\Delta R/R(0) \sim 0.4\%$. When $\mathbf{H}$ is applied along the x' axis, that is, the in-plane hard axis, the magnetization $\mathbf{M}$ tends to align toward the static field $\mathbf{H}$ and the angle θ_M is determined by $\sin(\theta_M) = H/H_A$ for $H < H_A$, where $H_A = N_{x'}M_0$ is the in-plane shape anisotropy field. The measured data (symbols) shown in Fig. 3(c) is fit (solid curve) according to $R(H) = R(0) - \Delta R \sin^2(\theta_M)$ with $R(0) = 112.66\Omega$, $\Delta R = 0.47\Omega$, $\mu_0 H_A = 4.0$ mT, and $N_{x'} = 0.004$.

Figure 3(d) shows that the line shape at $\theta_H = 120°$ and $\omega/2\pi = 5$ GHz is almost purely dispersive, indicating that at this frequency $\Phi \sim 90°$ according to Eq. (10). The θ_H dependence of H_r is shown in Fig. 3(e) and can be well fit by the function $\omega = \gamma\sqrt{[|H_r| + H_A\cos(2\theta_H)][|H_r| + M_0 - H_A(1 + \sin^2(\theta_H)]}$ by

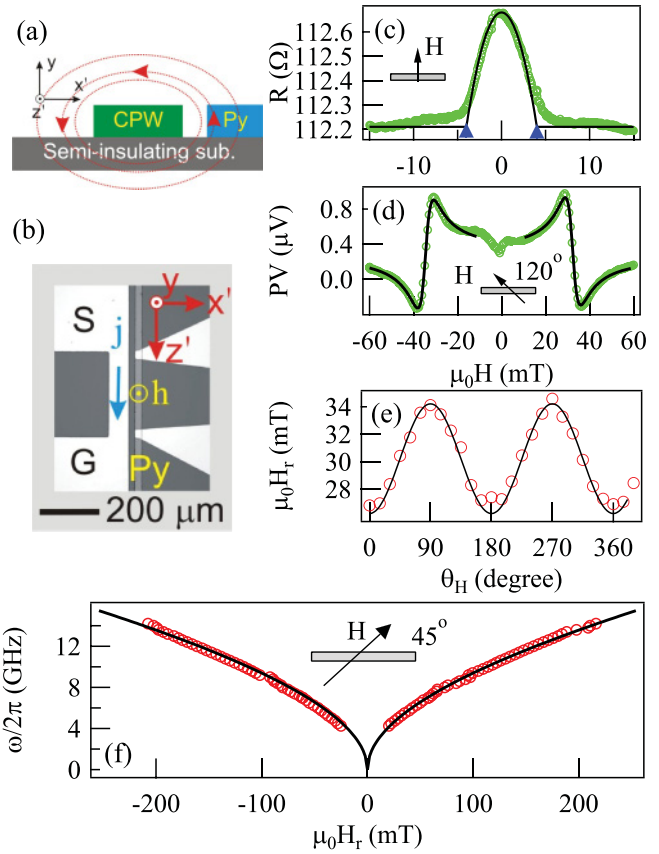

FIG. 3. (Color online) (a) Cross-sectional view of a schematic diagram showing the first generation spin dynamo where the Py strip is located beside the CPW. The dominate magnetic field in the Py is the Oersted field (indicated by circulating red arrows) in the y direction due to the current in the CPW. (b) Top view micrograph of the device showing the microwave current flowing in the shorted CPW and the direction of microwave h field on the Py strip. S and G denote the signal and ground line of the CPW, respectively. The Py microstrip is connected by two electrical leads in triangular shapes. (c) Magnetoresistance at $\theta_H = 90°$. AMR is seen to be ~0.4%. Arrows denote the anisotropic field $\mu_0 H_A = 4.0$ mT. Open circles are experimental data and solid curve is the fitting result using $R(0) = 112.66\Omega, \Delta R = 0.47\Omega, H_A = 4.0$ mT. (d) Electrically detected FMR at $\theta_H = 120°$ and $\omega/2\pi = 5$ GHz showing an almost purely dispersive line shape ($\Phi \simeq 90°$). Fit is according to Eq. (10) with $\mu_0\Delta H = 3.6$ mT, $\mu_0 H_r = 32.2$ mT. (e) Oscillating H_r dependence on the static field direction θ_H with amplitude $2H_A$. (f) Dependence of FMR frequency on the resonant field H_r at $\theta_H = 45°$. Open circles are experimental data and the solid line is the fit according to $\omega = \gamma\sqrt{|H_r|(|H_r| + M_0)}$.

taking the shape anisotropy field H_A along the x' axis into account.[59] As expected, the amplitude of these oscillations is $\mu_0 H_A = 4.0$ mT. The frequency dependence of H_r at $\theta_H = 45^\circ$ is shown in Fig. 3(f) and is fit using $\omega = \gamma\sqrt{|H_r|(|H_r| + M_0)}$ with $\gamma/2\pi = 29.0\mu_0$ GHz/T and $\mu_0 M_0 = 1.0$ T.

By systematically measuring the line shape as a function of the microwave frequency, we observe the interesting results of Fig. 4. The FMR line shape is observed to change from almost purely dispersive at $\omega/2\pi = 5$ GHz to almost purely symmetric at $\omega/2\pi = 5.56$ GHz. As discussed before, the line shape may be affected by the **h** orientation, that is, different **h** vector components will affect the line shape differently. Hence, if changing the microwave frequency changes the dominant driving field, the line shape may change. To rule out such a possibility an angular dependent experiment was performed to measure the line shape at different θ_H for each frequency ω. The results are plotted on the right panel of Fig. 4 which shows the sinusoidal curves for the Lorentz A_L and dispersive A_D amplitudes (dashed and solid curves, respectively) as a function of the static field angle θ_H. Both the Lorentz and dispersive amplitudes are found to follow a $\sin(2\theta_H)$ dependence on the field angle in agreement with Eq. (10) indicating that the magnetization precession is indeed dominantly driven by the h_y field. Therefore the line shape change indicates that the relative phase Φ is frequency dependent. As shown in Fig. 5(a), at $\omega/2\pi = 5$ GHz the amplitude of A_D is approximately one order of magnitude larger than A_L, while at $\omega/2\pi = 5.56$ GHz A_D is one order of magnitude less than A_L. Such a large change in A_L/A_D shows that in a microwave frequency range as narrow as 0.6 GHz, the relative phase Φ can change by 90°. Figure 5(b) shows Φ determined by using Eq. (10), which smoothly changes with microwave frequency except for a feature near 5.18 GHz, which is possibly caused by a resonant waveguide mode at this frequency.

Such a large change of Φ within a very narrow range of microwave frequency indicates the complexity of wave physics. Note that microwaves at ~5 GHz have wavelengths on the order of a few centimeters which are much larger than the submillimeter sample dimensions. Consequently, the microwave propagation depends strongly on the boundary conditions of Maxwell's equations which physically include the bonding wire, chip carrier, as well as the sample holder. This is similar to the microwave propagation in a waveguide where the field distribution, that is, the waveguide modes, are known to depend strongly on boundary conditions and frequency.[60] Despite the complex wave properties, the key message of our results is clear and consistent with the consideration of the physics of the relative phase: it shows

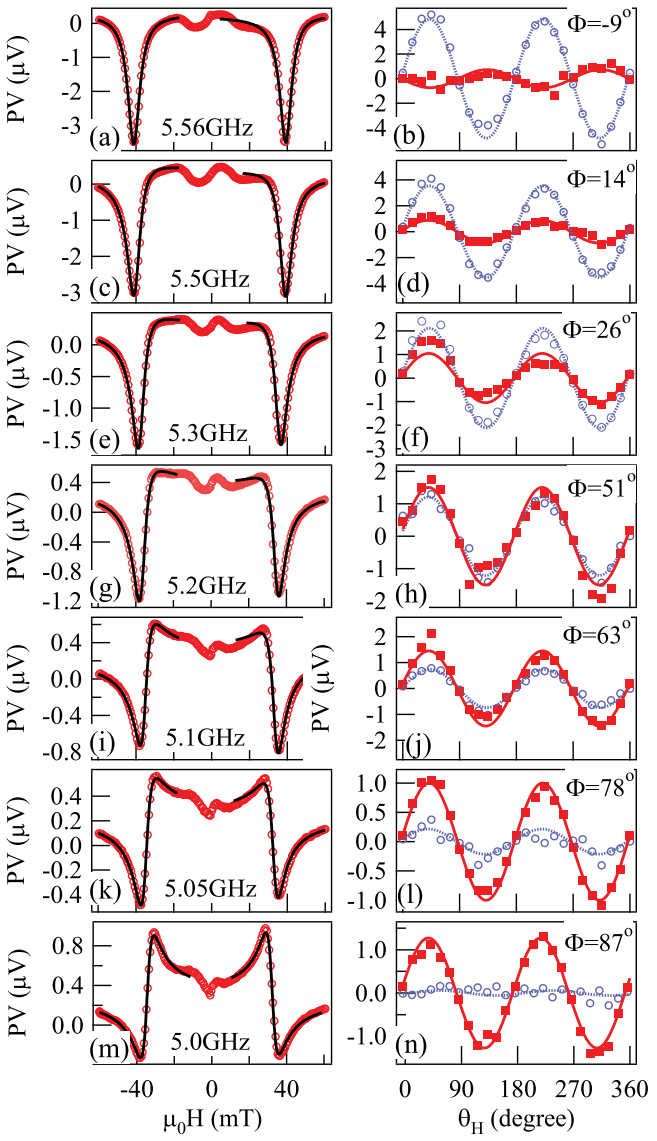

FIG. 4. (Color online) Data shown for a first generation spin dynamo. FMR spectra at $\theta_H = 120^\circ$ for several frequencies from 5.0 to 5.56 GHz with corresponding Lorentz and dispersive amplitudes as a function of θ_H. Circles and squares indicate the Lorentz and dispersive amplitudes of Eq. (10), respectively, and show a $\sin(2\theta_H)$ dependence as expected. Solid and dashed curves are $\sin(2\theta_H)$ functions.

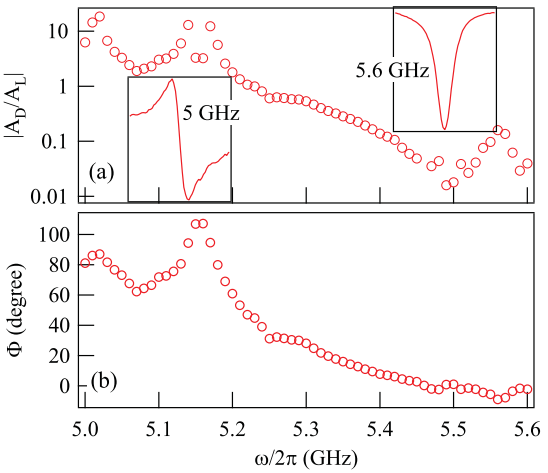

FIG. 5. (Color online) (a) The A_D/A_L ratio as a function of $\omega/2\pi$ showing the line shape change from dispersive at 5 GHz (left inset) to Lorentz at 5.6 GHz (right inset) with a step size of 0.01 GHz. (b) Φ dependence on $\omega/2\pi$ over same frequency interval showing the same dependence as A_D/A_L.

that in order to properly analyze the FMR line shape, Φ has to be determined for each frequency independently.

B. $h_{x'}$ dominant FMR

In order to drive the FMR using the rf field in the x' direction, $h_{x'}$, a second generation spin dynamo, was fabricated with the Py strip underneath the CPW as shown in Fig. 6. In this case the 300 μm $\times$ 7 μm $\times$ 100 nm Py strip is underneath the Cu/Cr coplanar waveguide which is fabricated on a SiO_2/Si substrate. Again a microwave current is directly injected into the CPW and induces a current in the z' direction in the Py strip. The dominant rf field in the Py is still the Oersted field, but due to the new geometry it is in the x' direction.

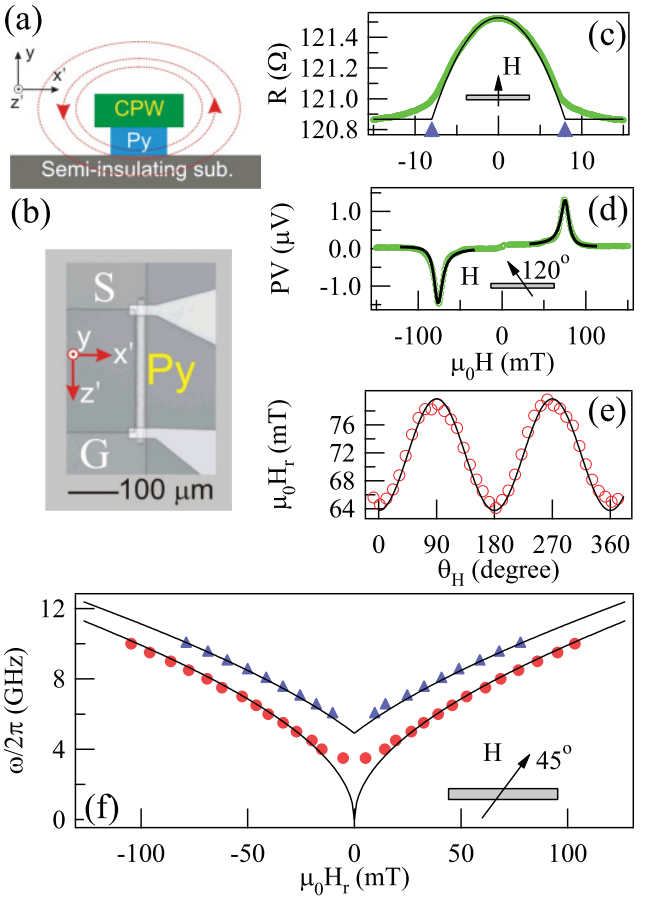

FIG. 6. (Color online) (a) Cross-sectional view of a schematic diagram showing the second generation spin dynamo where the Py strip is located underneath the CPW. In this case the dominant magnetic field in the Py is the Oersted field (indicated by circulating red arrows) in the x' direction due to the field in the CPW. (b) Top view micrograph of the Py microstrip underneath the shorted CPW (S and G denote the signal and ground line of the CPW, respectively). The Py microstrip is connected by two electrical leads in triangular shapes. (c) Magnetoresistance at $\theta_H = 90^\circ$. AMR is seen to be ~0.5%. Arrows denote the anisotropic field $\mu_0 H_A = 8.0$ mT. Open circles are experimental data and solid curve is the fitting result using $R(0) = 121.53\Omega$ and $\Delta R = 0.66\Omega$. (d) Electrically detected FMR at $\theta_H = 120^\circ$ and $\omega/2\pi = 8$ GHz showing a nearly symmetric Lorentz line shape. Fit is according to Eq. (10) with $\mu_0 \Delta H = 6.0$ mT, $\mu_0 H_r = 76.5$ mT, and $\Phi = -102^\circ$. (e) Oscillating H_r dependence on the static field direction θ_H with amplitude $2H_A$. (f) Dependence of FMR frequency on the resonant field H_r at $\theta_H = 45^\circ$. Solid circles show the FMR frequency dependence while the solid triangles are the standing SWR frequency dependence. The solid line is a fit to $\omega = \gamma\sqrt{|H_r|(|H_r| + M_0)}$.

Due to the smaller width and larger thickness, the demagnetization factor $N_{x'} = 0.008$ is twice that in the first generation sample. This corresponds to $\mu_0 H_A = 8.0$ mT as indicated by the broader AMR curve in Fig. 6(c). This value is further confirmed by the H_r vs θ_H plot shown in Fig. 6(e). Figure 6(f) shows the frequency dependence of H_r for FMR (circles) and for the first perpendicular standing spin wave resonance (SWR) (triangles) measured at $\theta_H = 45^\circ$. The frequency dependence of H_r follows $\omega = \gamma\sqrt{(|H_r| + H_{ex})(|H_r| + M_0 + H_{ex})}$ where H_{ex} is the exchange field. In Fig. 6(f) the standing SWR is fit using $\gamma/2\pi = 29.0\mu_0$ GHz/T, $\mu_0 H_{ex} = 30$ mT, and $\mu_0 M_0 = 1.0$ T.

Similar to the results presented in the previous section, the line shape of FMR measured on the second generation sample is also found to be frequency dependent (not shown). Hence, Φ is found to be nonzero in the general case. For example, at $\omega/2\pi = 8$ GHz, the line shape is found to be nearly symmetric, as shown in Fig. 6(d) for the FMR measured at $\theta_H = 120^\circ$, which indicates Φ is close to -90° at this frequency. Note that our result is in direct contrast with the recent study of Refs. 19 and 20, where experiments were measured in the same configuration and where it was suggested that $\Phi = 0^\circ$ for all samples at all frequencies.

While the line shape and hence the relative phase is found to be frequency dependent, Φ is expected to be independent of the static field direction θ_H. This is confirmed in Fig. 7(a) which shows the line shape measured at several values of θ_H in 10° increments. The data can be fit well using Eq. (9) with a constant $\Phi = -102^\circ$ for all θ_H. It confirms that the FMR is driven by a single **h** component, in this case the $h_{x'}$ field, and that Φ does not depend on θ_H. In Fig. 7(b) the θ_H dependence of A_L and A_D (solid/circles and dashed/squares, respectively) is shown. The circles and squares are experimental data while the solid and dashed lines are fitting results using a $\sin(2\theta_H)\cos(\theta_H)$ function according to Eq. (9). It provides further proof that the $h_{x'}$ field is responsible for driving the FMR in this sample.

While the results from both the first and second generation spin dynamos show consistently that Φ is sample and frequency dependent, the second generation spin dynamos exhibit special features in comparison with the first generation spin dynamos: the reduced separation between the Py strip and CPW enhances the $h_{x'}$ field so that the linewidth ΔH is enhanced by nonlinear magnetization damping,[27,28,61] which depends on the cone angle θ of the precession via the relation $\theta \sim h_{x'}\cos(\theta_H)/\Delta H(\theta)$. As shown in Fig. 7(c), ΔH is found to oscillate between 4.0 and 9.0 mT as θ_H changes. At $\theta_H = 0^\circ$, $\theta \sim h_{x'}/\Delta H$ and the cone angle is at its largest (about 4°). As θ_H increases from 0° and moves toward 90°, θ decreases so that the nonlinear damping contribution to ΔH decreases. Using the cone angle calculated from Fig. 7(c), we plot in Fig. 7(d) $\Delta H(\theta)$ as a function of the cone angle. It shows that ΔH has a quadratic dependence on the precession cone angle, which is in agreement with our previous study in the perpendicular **H**-field configuration.[27,28] We note that

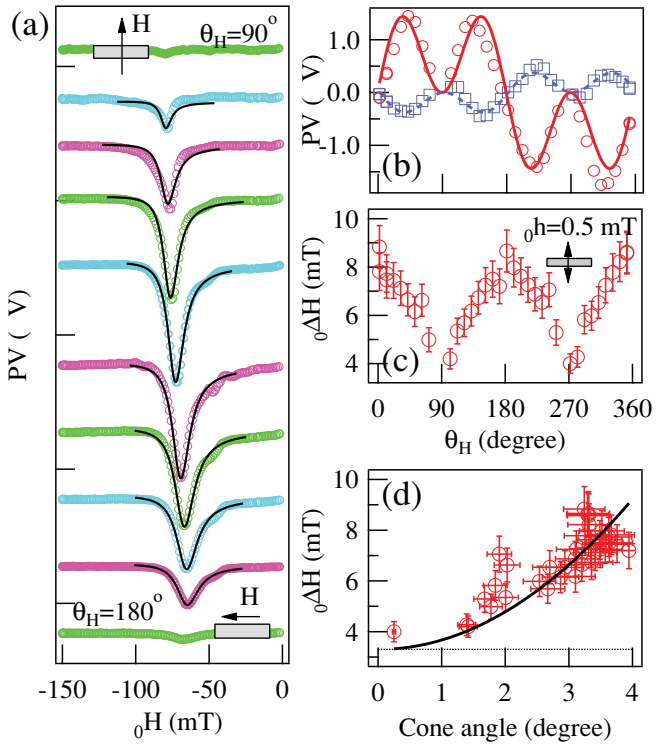

FIG. 7. (Color online) Data shown for a second generation spin dynamo. (a) FMR line shape at fixed frequency, $\omega/2\pi = 8$ GHz for several θ_H from 90° to 180° in steps of 10°. Open circles are experimental data and solid lines are fits using Eq. (9) with $\Phi = -102°$ fixed. (b) A_D and A_L shown in squares and circles respectively as a function of θ_H. Fitting curves are $\sin(2\theta_H)\cos(\theta_H)$ functions. (c) ΔH for several values of θ_H showing an oscillation with θ_H. (d) Nonlinear dependence of linewidth ΔH on the cone angle. Dashed line is the expected linear Gilbert damping whereas the data follows the quadratic dependence shown by the solid line.

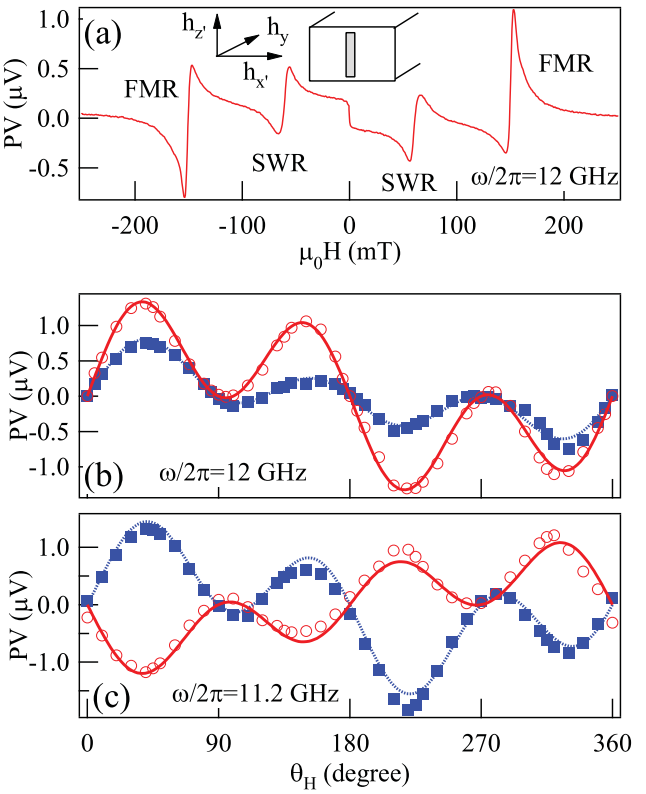

FIG. 8. (Color online) Data shown for a single Py strip with precession driven by horn antennae field. The strip dimensions are 3 mm × 50 μm × 45 nm. (a) Spectra showing distinct resonances due to FMR and SWR at $\omega/2\pi = 12$ GHz. (b) Separated Lorentz and dispersive line shapes (circles and squares, respectively) as a function of θ_H from a fit to Eq. (7) at $\omega/2\pi = 12$ GHz and (c) $\omega/2\pi = 11.2$ GHz.

for cone angles above only a few degrees, the nonlinear damping already dominates the contribution to ΔH. Hence, angular-dependent oscillations in the FMR linewidth provide a convenient way for verifying whether nonlinear effects may influence the electrically detected FMR.

C. Arbitrary *h* vector

Next we consider the most general case which is described by Eq. (7) where all components of **h** may contribute to the FMR line shape. The sample used here is a single Py strip where a waveguide with a horn antennae provided both the electric and magnetic driving fields. The sample chip is mounted near the center, at the end of a rectangular waveguide and the Py strip is directed along the short axis of the waveguide.

In a waveguide, the electromagnetic fields are well known and in general three components, $h_{x'}$,h_y, and $h_{z'}$ exist.[60] Figure 8(a) shows both the FMR and perpendicular standing SWR measured at $\theta_H = 45°$. Indeed both the amplitude and the line shape are different for the two FMR peaks located at H and $-H$, which indicates the existence of multiple **h** field components and Eqs. (7) and (8) are needed to separate them.

This separation is done using the Lorentz and dispersive amplitudes determined from a fit to the FMR which are plotted as a function of θ_H in Figs. 8(b) and 8(c) for $\omega/2\pi = 12$ and 11.2 GHz, respectively. A fit using Eq. (8) allows a separation of the contributions from each of the $h_{x'}$,h_y, and $h_{z'}$ fields based on the their different contributions to the θ_H dependence of the line shape.

The results of the fit have been tabulated in Table II where $\gamma/2\pi = 28.0\mu_0$ GHz/T, $\mu_0 M_0 = 0.97$ T and $\mu_0 H_r = 152$ mT were used. The amplitudes of the different **h** field components have been normalized with respect to the $h_{x'}$ component. At both 11.2 and 12 GHz the $h_{x'}$ field is much larger than h_y or

TABLE II. Angular separation of **h** field components for 12 and 11.2 GHz.

	12 GHz	11.2 GHz
$\lvert h_{x'}\rvert$	1	1
$\lvert h_y\rvert$	0.02 ± 0.10	0.14 ± 0.07
$\lvert h_{z'}\rvert$	0.19 ± 0.06	0.37 ± 0.10
$\Phi_{x'}$	$-23 \pm 2°$	$50 \pm 2°$
Φ_y	$40 \pm 24°$	$-30 \pm 18°$
$\Phi_{z'}$	$-33 \pm 7°$	$82 \pm 5°$

$h_{z'}$, which is expected based on the wave propagation in a horn antennae.

We note that in this case with the device as long as 3 mm, the phase angle might change with position along the length of the device to an extent where a spread of angles should be taken into consideration. Nevertheless, even by using the crudest approximation to fit the data as if there is a single phase angle between each pair of e and h components, the relative phase for each component is seen to change significantly from 11.2 to 12 GHz. Therefore even in the case of a complex line shape produced by multiple **h** field components, by separating the individual contributions of the rf magnetic field via angular dependence measurements, the relative phase Φ of each field component is found to be frequency dependent.

D. Additional influences on Φ

In addition to the frequency and sample dependencies, the relative phase Φ may also depend on the lead configuration and wiring conditions of a particular device, as we have mentioned in Sec. IV A. Here we address such additional influences by using the first generation spin dynamos[11] shown in the inset of Fig. 9(a). Two spin dynamos with the same lateral dimensions but different Py thickness d are studied. Each spin dynamo involves two identical Py strips denoted by S1 and S2, one in each center of the G-S strips of the CPW, which are placed symmetrically with respect to the S strip. The current and rf **h** field are induced in the Py via a microwave current directly injected into the CPW. Similar to the sample discussed in Sec. IV A, h_y is the dominant field which drives the FMR.

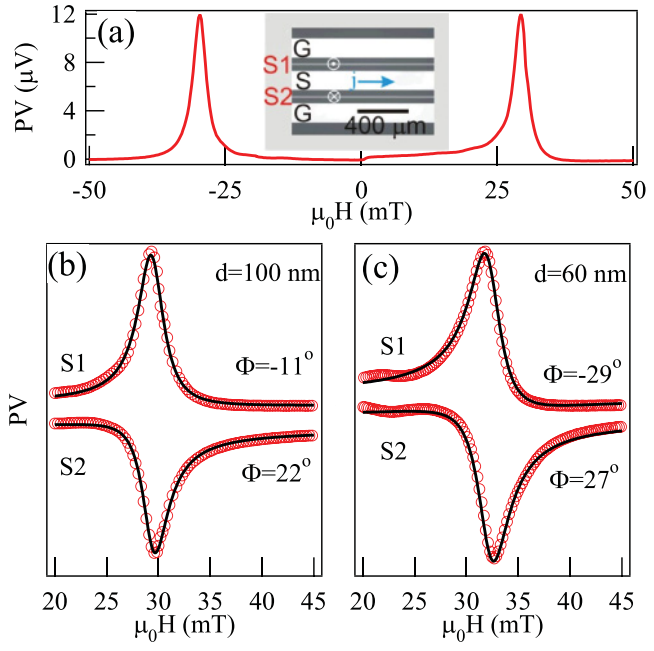

FIG. 9. (Color online) (a) FMR observed in a first generation spin dynamo. Inset shows the device structure with two Py strips labeled S1 and S2. (b) FMR for Py thickness $d = 100$ nm for both S1 and S2. In S1 $\Phi = -11^\circ$, while in S2 the line shape is slightly more asymmetric and $\Phi = 22^\circ$. (c) For $d = 60$ nm the relative phase is $\Phi = -29^\circ$ for S1 and $\Phi = 27^\circ$ for S2.

As shown in Fig. 9(a), FMR measured at $\omega/2\pi = 5$ GHz on the sample S1 with $d = 100$ nm shows a nearly symmetric Lorentz line shape and a field symmetry of $V(H) = V(-H)$. From the FMR line shape fitting, $\Phi = -11^\circ$ is found. Interestingly, as shown in Fig. 9(b), the FMR of the sample S2 of the same spin dynamo measured under the same experimental conditions shows a different line shape from which a different $\Phi = 22^\circ$ is found. We can further compare Φ measured on the other spin dynamo with a different Py thickness of $d = 60$ nm, also at $\omega/2\pi = 5$ GHz. Here for S1, $\Phi = -29^\circ$ while for S2, $\Phi = 27^\circ$. Again, the relative phase is found to be different for S1 and S2. These results demonstrate that due to additional influences such as different lead configuration and wiring conditions, even for samples with the same lateral dimensions Φ in each device is not necessarily the same. It demonstrates clearly that the relative phase Φ cannot be simply determined by analyzing the FMR line shape measured on a reference device. We note that our previous experiment performed using spintronic interferometry[38] also manifested similar sensitivity of the relative phase to the lead configuration and wiring conditions of a particular device.

E. Closing remarks

The experimental data presented above demonstrate the importance of the difference in the phase between the magnetic and electric field components and the role of the orientation of the rf magnetic field with respect to the film surface. Interpretation of the data depends on such a phase difference Φ, which is found to be sample and frequency dependent and nonzero in general. This nonzero phase results in both symmetric and antisymmetric Lorentz line shapes in the FMR detected via field-torque induced spin rectification. The Φ dependence of the line shape symmetry changes based on which component of the rf **h** field is responsible for driving the FMR precession. For instance a purely antisymmetric line shape could correspond to $\Phi = 0^\circ$ if the FMR is driven by $h_{x'}$, or to $\Phi = 90^\circ$ if the FMR is driven by h_y, therefore the line shape itself cannot be used to determine Φ directly. To separate the **h** field components an angular (θ_H) dependent measurement is necessary, which allows both **h** as well as the phase to be determined. Using such a measurement Φ has been observed to change from 0° to 90° in a narrow frequency range (0.6 GHz) resulting in a change from an antisymmetric to symmetric line shape demonstrating the large effect the relative phase has on the FMR line shape. Furthermore, Φ is not identical even in samples with the same geometric size. Therefore in our opinion, it is not a reliable approach to determine the pivotal relative phase Φ from different reference samples, as was adopted in some of the most recent studies.[19,20,24] Instead, to quantitatively interpret the measured microwave photovoltage induced by FMR, Φ should be calibrated for each sample, at each frequency, and for each measurement cycle.

V. Summary

We have provided a brief review of the rapidly growing literature on electrical detection of spin dynamics in micro- and nanodevices. We have focused on the important issue of

the relation and distinction between different mechanisms that give rise to the rf photovoltage via FMR in spintronic devices. Such a photovoltage has in general two different types of origins: spin pumping (V_{SP}) and spin rectification (V_{SR}), where the spin rectification may be induced by either rf h field or spin torque, which give rise to the photovoltages V_{SR}^{h} and V_{SR}^{s}, respectively.

We have shown that in order to distinguish different mechanisms which enable the electrical detection of FMR via microwave photovoltages, it is essential to properly analyze the FMR line shape. While spin pumping is an incoherent and interfacial effect which always gives rise to a symmetric FMR line shape in V_{SP}, spin rectification is not restricted at the interface and is caused by coherent coupling between rf current and magnetization. Hence, the FMR line shape of V_{SR} is intriguingly phase dependent and may have both symmetric and antisymmetric components. We have found theoretically that for rf h-field torque induced spin rectification, the FMR line shape of V_{SR}^{h} depends strongly on the relative phase Φ between the rf e and h fields used to drive the current and magnetization, respectively. Analytical formulas have been established to analyze the FMR line shape of V_{SR}^{h}, and our approach based on the dynamic susceptibility can be further generalized to analyze the FMR line shape of spin torque induced photovoltage V_{SR}^{s}.

Based on a systematic study of the measured photovoltage, the FMR line shape of V_{SR}^{h} is observed to depend strongly on the microwave frequency, driving field configuration, sample structure, and even wiring conditions. Therefore we have presented strong evidence that within the standard microwave circuit geometries used to build spintronic devices, it is common for nonzero relative phase Φ to exist at the spin device location. This could cause a skew in the field-swept FMR line shape which, when this phase angle is unknown, can lead to unintentional quantitative errors when extracting individual mechanistic contributions to the photovoltage by fitting the line shapes. Our results imply that for electrically detected FMR which involves both spin Hall and spin rectification effects, the pivotal relative phase must be either directly calibrated or precisely controlled in order to properly analyze the FMR line shape and quantify the spin Hall angle. For such studies, we strongly suggest not to use the unreliable approach of determining Φ from reference samples, but instead recommend applying spintronic Michelson interferometry[38] which enables external control of the relative phase.

ACKNOWLEDGMENTS

We would like to thank B. W. Southern, A. Hoffmann, S. D. Bader, B. Heinrich, D. C. Ralph, G. E. W. Bauer, and S.M. Rezende for discussions. This work has been funded by NSERC, CFI, CMC, and URGP grants (C.-M.H.). Z.X.C. was supported by the National Natural Science Foundation of China Grant No. 10990100.

*hu@physics.umanitoba.ca; URL: http://www.physics.umanitoba.ca/∼hu

[1] M. Tsoi, A. G. M. Jansen, J. Bass, W.-C. Chiang, V. Tsoi, and P. Wyder, Nature (London) **406**, 46 (2000).

[2] S. I. Kiselev, J. C. Sankey, I. N. Krivorotov, N. C. Emley, R. J. Schoelkopf, R. A. Buhrman, and D. C. Ralph, Nature (London) **425**, 380 (2003).

[3] Y. S. Gui, S. Holland, N. Mecking, and C.-M. Hu, Phys. Rev. Lett. **95**, 056807 (2005).

[4] A. A. Tulapurkar, Y. Suzuki, A. Fukushima, H. Kubota, H. Maehara, K. Tsunekawa, D. D. Djayaprawira, N. Watanabe, and S. Yuasa, Nature (London) **438**, 339 (2005).

[5] A. Azevedo, L. H. Vilela Leo, R. L. Rodriguez-Suarez, A. B. Oliveira, and S. M. Rezende, J. Appl. Phys. **97**, 10C715 (2005).

[6] M. V. Costache, S. M. Watts, M. Sladkov, C. H. van der Wal, and B. J. van Wees, Appl. Phys. Lett. **89**, 232115 (2006).

[7] M. V. Costache, M. Sladkov, S. M. Watts, C. H. van der Wal, and B. J. van Wees, Phys. Rev. Lett. **97**, 216603 (2006).

[8] E. Saitoh, M. Ueda, H. Miyajima, and G. Tatara, Appl. Phys. Lett. **88**, 182509 (2006).

[9] J. C. Sankey, P. M. Braganca, A. G. F. Garcia, I. N. Krivorotov, R. A. Buhrman, and D. C. Ralph, Phys. Rev. Lett. **96**, 227601 (2006).

[10] H. Kubota, A. Fukushima, K. Yakushiji, T. Nagahama, S. Yuasa, K. Ando, H. Maehara, Y. Nagamine, K. Tsunekawa, D. D. Djayaprawira, N. Watanabe, and Y. Suzuki, Nat. Phys. **4**, 37 (2007).

[11] Y. S. Gui, N. Mecking, X. Zhou, G. Williams, and C. -M. Hu, Phys. Rev. Lett. **98**, 107602 (2007).

[12] N. Mecking, Y. S. Gui, and C.-M. Hu, Phys. Rev. B **76**, 224430 (2007).

[13] A. Yamaguchi, H. Miyajima, T. Ono, Y. Suzuki, S. Yuasa, A. Tulapurkar, and Y. Nakatani, Appl. Phys. Lett. **90**, 182507 (2007).

[14] S. T. Goennenwein, S. W. Schink, A. Brandlmaier, A. Boger, M. Opel, R. Gross, R. S. Keizer, T. M. Klapwijk, A. Gupta, H. Huebl, C. Bihler, and M. S. Brandt, Appl. Phys. Lett. **90**, 162507 (2007).

[15] J. C. Sankey, Y. T. Cui, J. Z. Sun, J. C. Slonczewski, Robert A. Buhrman, and D. C. Ralph, Nat. Phys. **4**, 67 (2008).

[16] X. Hui, A. Wirthmann, Y. S. Gui, Y. Tian, X. F. Jin, Z. H. Chen, S. C. Shen, and C. -M. Hu, Appl. Phys. Lett. **93**, 232502 (2008).

[17] A. Wirthmann, X. Hui, N. Mecking, Y. S. Gui, T. Chakraborty, C. -M. Hu, M. Reinwald, C. Schüller, and W. Wegscheider, Appl. Phys. Lett. **92**, 232106 (2008).

[18] V. A. Atsarkin, V. V. Demidov, L. V. Levkin, and A. M. Petrzhik, Phys. Rev. B **82**, 144414 (2010).

[19] O. Mosendz, J. E. Pearson, F. Y. Fradin, G. E. W. Bauer, S. D. Bader, and A. Hoffmann, Phys. Rev. Lett. **104**, 046601 (2010).

[20] O. Mosendz, V. Vlaminck, J. E. Pearson, F. Y. Fradin, G. E. W. Bauer, S. D. Bader, and A. Hoffmann, Phys. Rev. B **82**, 214403 (2010).

[21] P. Saraiva, A. Nogaret, J. C. Portal, H. E. Beere, and D. A. Ritchie, Phys. Rev. B **82**, 224417 (2010).

[22] Y. Kajiwara, K. Harii, S. Takahashi, J. Ohe, K. Uchida, M. Mizuguchi, H. Umezawa, H. Kawai, K. Ando, K. Takanashi, S. Maekawa, and E. Saitoh, Nature (London) **464**, 262 (2010).

[23]C. W. Sandweg, Y. Kajiwara, K. Ando, E. Saitoh, and B. Hillebrands, Appl. Phys. Lett. **97**, 252504 (2010).
[24]L. Liu, T. Moriyama, D. C. Ralph, and R. A. Buhrman, Phys. Rev. Lett. **106**, 036601 (2011).
[25]A. Azevedo, L. H. Vilela Leão, R. L. Rodríguez-Suárez, A. F. Lacerda Santos, and S. M. Rezende, Phys. Rev. B **83**, 144402 (2011).
[26]Y. S. Gui, N. Mecking, and C.-M. Hu, Phys. Rev. Lett. **98**, 217603 (2007).
[27]Y. S. Gui, A. Wirthmann, N. Mecking, and C.-M. Hu, Phys. Rev. B **80**, 060402(R) (2009).
[28]Y. S. Gui, A. Wirthmann, and C.-M. Hu, Phys. Rev. B **80**, 184422 (2009).
[29]C. T. Boone, J. A. Katine, J. R. Childress, V. Tiberkevich, A. Slavin, J. Zhu, X. Cheng, and I. N. Krivorotov, Phys. Rev. Lett. **103**, 167601 (2009).
[30]D. Bedau, M. Kläui, S. Krzyk, U. Rüdiger, G. Faini, and L. Vila, Phys. Rev. Lett. **99**, 146601 (2007).
[31]S. Bonetti, V. Tiberkevich, G. Consolo, G. Finocchio, P. Muduli, F. Mancoff, A. Slavin, and J. Åkerman, Phys. Rev. Lett. **105**, 217204 (2010).
[32]S. Urazhdin, V. Tiberkevich, and A. Slavin, Phys. Rev. Lett. **105**, 237204 (2010).
[33]Y. Tserkovnyak, A. Brataas, G. E. W. Bauer, and B. I. Halperin, Rev. Mod. Phys. **77**, 1375 (2005).
[34]L. Berger, Phys. Rev. B **59**, 11465 (1999).
[35]A. Brataas, Y. Tserkovnyak, G. E. W. Bauer, and B. I. Halperin, Phys. Rev. B **66**, 060404 (2002).
[36]X. Wang, G. E. W. Bauer, B. J. van Wees, A. Brataas, and Y. Tserkovnyak, Phys. Rev. Lett. **97**, 216602 (2006).
[37]A. Yamaguchi, H. Miyajima, S. Kasai, and T. Ono, Appl. Phys. Lett. **90**, 212505 (2007).
[38]A. Wirthmann, X. Fan, Y. S. Gui, K. Martens, G. Williams, J. Dietrich, G. E. Bridges, and C.-M. Hu, Phys. Rev. Lett. **105**, 017202 (2010).
[39]X. F. Zhu, M. Harder, A. Wirthmann, B. Zhang, W. Lu, Y. S. Gui, and C.-M. Hu, Phys. Rev. B **83**, 104407 (2011).
[40]X. Fan, S. Kim, X. Kou, J. Kolodzey, H. Zhang, and J. Q. Xiao, Appl. Phys. Lett. **97**, 212501 (2010).
[41]L. H. Bai, Y. S. Gui, A. Wirthmann, E. Recksiedler, N. Mecking, C.-M. Hu, Z. H. Chen, and S. C. Shen, Appl. Phys. Lett. **92**, 032504 (2008).
[42]H. Zhao, E. J. Loren, H. M. van Driel, and A. L. Smirl, Phys. Rev. Lett. **96**, 246601 (2006).
[43]J. Wang, B. F. Zhu, and R. B. Liu, Phys. Rev. Lett. **104**, 256601 (2010).
[44]L. K. Werake and H. Zhao, Nat. Phys. **6**, 875 (2010).
[45]Via private communications, Dr. Hoffmann suggests that "The fact of the matter is that the experiments (Refs. 19 and 24) are conceptually very different and also in their approach very different. In the Cornell experiment (Ref. 24) the rf current is applied directly to the Py/Pt bilayer, while in our case (Ref. 19) only a small fraction of the rf current flows through the bilayer as a consequence of the capacitive coupling. This means that in the Cornell measurement the ratio of rf current to the rf magnetic field exciting the magnetization dynamics is significantly higher than in our experiments and that is the reason why the ratio of any voltages from spin Hall effects compared to AMR voltages is significantly smaller than in our experiments." We note that it is an important task to check whether such an interesting interpretation might be directly confirmed in a controlled experiment, for example, by directly comparing the photovoltage measured on the same Py/Pt bilayer using two different approaches for applying the rf current.
[46]J. D. Jackson, *Classical Electrodynamics*, 2nd ed. (John Wiley & Sons, New York, 1975).
[47]H. J. Juretschke, J. Appl. Phys. **31**, 1401 (1960).
[48]R. H. Silsbee, A. Janossy, and P. Monod, Phys. Rev. B **19**, 4382 (1979).
[49]B. Heinrich, Y. Tserkovnyak, G. Woltersdorf, A. Brataas, R. Urban, and G. E. W. Bauer, Phys. Rev. Lett. **90**, 187601 (2003).
[50]J. N. Kupferschmidt, S. Adam, and P. W. Brouwer, Phys. Rev. B **74**, 134416 (2006).
[51]A. A. Kovalev, G. E. W. Bauer, and A. Brataas, Phys. Rev. B **75**, 014430 (2007).
[52]Via private communications, Dr. Rezende points out that their group, unaware of Ref. 38, has worked independently on the question of the line shape and developed a theory (Ref. 25) for V_{SR}^{h} that considered both Lorentzian and dispersive components which are essential to fit their data for the angular dependence of the dc voltage produced by FMR. Specifically, Dr. Rezende points out that they have the following independent findings: (1) The important role and the consequence of the phase between the external rf h field and the induced rf current, which was previously considered to be 0° (or 90° depending on reference). (2) The existence of the Lorentzian component of V_{SR}^{h}. Previous papers (Refs. 19 and 20) considered that V_{SR}^{h} had only a Lorentzian derivative component and that, as they have pointed out in their paper (Ref. 25), was one of the reasons for the erroneous values for the material parameters obtained previously.
[53]T. L. Gilbert, IEEE Trans. Magn. **40**, 3443 (2004).
[54]L. D. Landau and E. M. Lifshitz, *Mechanics*, 2nd ed. (Pergamon, Oxford, 1969).
[55]J. P. Jan, in *Solid State Physics*, edited by F. Seitz and D. Turnbull (Academic, New York, 1957), Vol. 5.
[56]M. Born and E. Wolf, *Principles of Optics: Electromagnetic Theory of Propagation, Interference and Diffraction*, 7th ed. (Cambridge University Press, Cambridge, 1999).
[57]W. Heinrich, IEEE Trans. Microwave Theory Tech. **38**, 1468 (1990).
[58]W. Heinrich, IEEE Trans. Microwave Theory Tech. **41**, 45 (1993).
[59]S. V. Vonsovskii, *Ferromagnetic Resonance: The Phenomenon of Resonant Absorption of a High-Frequency Magnetic Field in Ferromagnetic Substances*, (Pergamon, Oxford, 1966).
[60]B. S. Guru and H. R. Hiziroglu, *Electromagnetic Field Theory Fundamentals*, 2nd ed. (Cambridge University Press, Cambridge, 2004).
[61]V. Tiberkevich and A. Slavin, Phys. Rev. B **75**, 014440 (2007).